Heavy Quarkonia Production in e^+e^- Collisions at the Z Pole

by

Cary Robert Lapoint

Submitted to the Department of Physics
in partial fulfillment of the requirements for the degree of

Doctor of Philosophy

at the

MASSACHUSETTS INSTITUTE OF TECHNOLOGY

June 1998

Author .....
Department of Physics
April 14, 1998

Certified by.....
Peter H. Fisher
Associate Professor
Thesis Supervisor

Accepted by.....
Thomas J. Greytak
Chairman, Physics Graduate Committee

Heavy Quarkonia Production in e^+e^- Collisions at the Z Pole

by

Cary Robert Lapoint

Submitted to the Department of Physics
on April 14, 1998, in partial fulfillment of the
requirements for the degree of
Doctor of Philosophy

Abstract

In this thesis I describe a study of heavy quarkonia production in the hadronic decays of the Z boson performed at the LEP e^+e^- collider. Selection algorithms were developed to identify charmonium states, taking advantage of the significant branching ratios of the J meson to dileptons as well as the sizable branching ratios of the ψ' and χ_c mesons to final states involving a J. Selection efficiencies were estimated from fully simulated signal events generated with the JETSET 7.4 Monte Carlo and a prompt heavy quarkonium Monte Carlo. Analyzing the full LEP I data set of approximately 3.6 million hadronic events collected by the L3 experiment between 1991 and 1995, final measurements of $\mathrm{Br}(\mathrm{Z} \to \mathrm{J} + \mathrm{X})$, $\mathrm{Br}(\mathrm{Z} \to \psi' + \mathrm{X})$, and $\mathrm{Br}(\mathrm{Z} \to \chi_c^1 + \mathrm{X})$ were made. Additionally, the fraction of prompt J mesons in Z decays was measured for the first time at L3, yielding information on the nature of the QCD production of J mesons. The results are:

$$\begin{aligned} \mathrm{Br}(\mathrm{Z} \to \mathrm{J} + \mathrm{X}) &= (3.16 \pm 0.21^{+0.19}_{-0.28}) \times 10^{-3} \\ \mathrm{Br}(\mathrm{Z} \to \psi' + \mathrm{X}) &= (2.4 \pm 0.5^{+0.7}_{-0.8}) \times 10^{-3} \\ \mathrm{Br}(\mathrm{Z} \to \chi_c^1 + \mathrm{X}) &= (1.9 \pm 0.7^{+0.3}_{-0.6}) \times 10^{-3} \\ f_{\mathrm{p}} &= (8.3 \pm 2.3 \pm 1.7^{+1.4}_{-0.7}) \times 10^{-2} \end{aligned}$$

Thesis Supervisor: Peter H. Fisher
Title: Associate Professor

Acknowledgments

I would like to express my gratitude to my wife Jeni for her love, support, and understanding during the production of this thesis.

Contents

List of Figures

List of Tables

Chapter 1

Introduction

1.1 Overview

The discovery of the J particle in the fall of 1974 opened up an extremely rich area of scientific inquiry, both theoretically and experimentally [1] [2]. Early work on charmonium spectroscopy, development of potential models, measurement of charmonium branching ratios, and QCD lattice simulations, not to mention similar pursuits for D mesons have become minor industries, occupying the time and efforts of hundreds of high energy physicists. Still, despite the undeniable progress made over the past 23 years, the details of one of the most fundamental aspects of heavy quarkonium physics, production, remain poorly understood. Three models have been developed to describe the production of heavy quark bound states, namely the Color Singlet Model (CSM) [3] [4], the Velocity Scaling Model (VSM) based on the Bodwin-Braaten-Lepage (BBL) formalism [5] [3], and the Color Evaporation Model (CEM) [3] [6] [7] [8]. Each of these models will be explained, and, as will be shown, while all can account for certain features of the collective charmonium and bottomonium production data set, none can successfully account for all of them.

Before proceeding, it is instructive to establish a few of the motivations for studying the production of heavy quarkonium states, charmonium states in particular. One of the most compelling reasons to understand J production is that J's are used as tools in other analyses due to their high branching fraction to easily identifiable dilepton final states ($\mathrm{Br}(\mathrm{J} \to \ell^+\ell^-) = 6.0\%$) and to the fact that they are most often generated in the process of b-hadron decay ($\mathrm{Br}(\mathrm{b} \to \mathrm{J}+\mathrm{X}) \approx 1\%$). Without a solid understanding of all the sources of J's, however, the results of analyses using J's can be in error. For example, an early measurement of the b-quark production cross-section at the Tevatron based on the number of J's produced was later found to be in error by roughly a factor 2 because of an unexpected excess of prompt J's [9]. Conversely, if J production is well understood, there are several useful applications in the area of b-quark physics. One can use the momentum spectrum

of a sample of J's to study b-fragmentation by measuring the Peterson parameter ϵ_b. While ϵ_b is more accurately determined using other methods, this is a nice, independent measurement. With an even larger sample of events containing J's (b-quark enhanced sample), it should be possible to compare decay length distributions from data and Monte Carlo to test b-tagging algorithms based on silicon vertex detector information. Once one recognizes the value of understanding J production, it follows that an understanding of χ_c and ψ' production is essential as well since there is substantial feeddown from these higher states to J's. Finally, from a theoretical viewpoint, heavy quarkonia are rather interesting objects because they necessitate an understanding of QCD at the transition point between the perturbative regime and the non-perturbative regime ($Q^2 \simeq$ a few GeV^2) [10]. These are just a few of the reasons why the study of charmonium production is worth pursuing.

The purpose of this thesis will be to study the production of various heavy quark bound states in Z decays using the L3 detector at LEP. Specifically, the inclusive branching ratios of the Z to J's, ψ''s, χ_c's, and prompt J's will be measured. The e^+e^- environment at LEP is a particularly attractive place in which to make such measurements because Z bosons have been produced and studied here for many years, and all of the Z decay modes, including the $Z \to q\bar{q}$ relevant to this work, are well understood. Where meaningful comparisons are possible, theoretical predictions will be confronted with the experimental results, and when theory is insufficiently precise, the measurements can simply be viewed as additions to the existing body of knowledge about heavy quarkonium production. It is the hope that one day a complete and coherent theoretical picture will emerge which can accurately describe production of $c\bar{c}$ and $b\bar{b}$ bound states in a variety of different processes from electro- and photoproduction to hadroproduction to Z decays and that experiment will not only provide a benchmark by which to judge the success of production theory but also serve as a guide for its evolution.

1.2 Quarkonium Production and Decay Models

1.2.1 Color Singlet Model

One of the earliest attempts to explain heavy quarkonium production was the Color Singlet Model (CSM). The basic premise of this model is that only those $Q\bar{Q}$ pairs which are produced in a given J^{PC} state in a color singlet configuration evolve into color singlet quarkonium states of the same J^{PC}. Mathematically, the model asserts that the production rate of a particular heavy quarkonium state is the product of a long-distance factor(F_{nl}) and a short-distance differential cross-section [3]. To take a concrete example, for J production as a function of p_t one has:

$$\frac{d\sigma[J]}{dp_t} = F_{10} \times \frac{d\sigma[c\bar{c}(1^3S_1, \underline{1})]}{dp_t} \tag{1.1}$$

The short-distance factor is a differential cross-section for the production of the $c\bar{c}$ pair in the state $(1^3S_1, \underline{1})$, where the first part of the state description is standard spectroscopic notation for the radial and angular momentum quantum numbers, and the second part indicates color singlet ($\underline{1}$) as opposed to color octet ($\underline{8}$). In principle, such a cross-section can be calculated using perturbative QCD (pQCD) to any desired order in α_s, and in general it will depend on the specific collision process, the center of mass energy ($\sqrt{s}$), and other kinematic variables like p_t. The long distance factor in Equation 1.1, which represents the probability for the $c\bar{c}$ pair to evolve into a quarkonium bound state, on the other hand, is non-perturbative and cannot be easily calculated. At lowest order, it is directly related to the quarkonium radial wave function or its derivatives at the origin, however, and can be determined experimentally from the quarkonium decay widths [3].

In the past the CSM has been used to calculate heavy quarkonium production in a wide variety of processes including hadroproduction, Z decays, and b-hadron decay [4] [11] [12] [13] [14]. Initially, the CSM enjoyed reasonable success when calculations were compared to measurements at various facilities. By the early 1990's, however, there was mounting theoretical and experimental evidence suggesting that the CSM was not an entirely satisfactory framework for estimating charmonium and bottomonium production rates. At CDF an initial measurement of the b-quark production cross-section based on J production was later shown to be too large by a factor of about two [9]. Installation of a silicon vertex detector prior to the 1992-1993 run enabled subsequent investigators to distinguish prompt charmonium states from those coming from b-hadron decay, and it was discovered that only 20% (23%) of the J's (ψ's) were from the latter category [9]. Measurements of prompt J and ψ' production at high p_t ($p_t \gtrsim 4.0$ GeV) were found to be anomalously large, yielding rates approximately 50 times higher than the CSM predictions [15]. Additional measurements designed to isolate the χ_c radiative cascade contribution to J production revealed even more surprises. It was found that a mere 32% of the prompt J's were daughter products of χ_c decays [9] [15]. All of these results were contrary to the conventional expectations of the CSM, forcing theorists to seriously consider other mechanisms that could be responsible for the observed charmonium production. On the purely theoretical front it was pointed out early on that traditional calculations of χ_c decays resulted in the presence of infrared divergences associated with the emission of soft gluons [16] [17] [18] [19]. Similar divergences were later found in calculations of χ_c production, and these proved to be intractable in the sense that their structure prevented them from being absorbed into the non-perturbative factors related to the quarkonia wave functions at the origin [20]. It was largely due to such theoretical difficulties and most importantly the J and ψ' excesses observed at the Tevatron that both theoretical and experimental interest in heavy quarkonium production was renewed and that the CSM was brought under severe scrutiny.

1.2.2 Velocity Scaling Model

Recognizing the possibility that the CSM was no longer viable, a serious theoretical effort was mounted to develop a more rigorous, more powerful, model of heavy quarkonium production and decays. The breakthrough came in 1992 with the first published paper describing the Velocity Scaling Model (VSM), or Color Octet Model, and its application to P-wave decays [21]. A paper treating P-wave production in B-meson decays followed soon thereafter [22]. Based on nonrelativistic QCD (NRQCD), the VSM successfully separates the short-distance scale factors associated with annihilation and production set by the heavy quark mass, M, from the long-distance scale factors associated with the heavy quarkonium structure set by Mv and Mv^2, where v represents the relative velocity of the heavy quarks inside the quarkonium. Moreover, the formalism provides a very natural way to accomodate relativistic corrections to leading order estimates. With the arrival of the VSM, quarkonium calculations were placed on a more solid theoretical foundation.

The crucial aspects of the VSM are that both color singlet and color octet initial states are considered in the production and decays of heavy quarkonia and that rates are given by a sum of terms, each of which cleanly factorizes into a short-distance coefficient ($F_{\underline{c}}^d(X)$) and a long-distance NRQCD matrix element. The production rate of a quarkonium state H, can be expressed as [3]:

$$\sigma(H) = \sum_d \sum_X (F_{\underline{1}}^d(X) \times < 0|O_{\underline{1}}^H(d,X)|0 > + F_{\underline{8}}^d(X) \times < 0|O_{\underline{8}}^H(d,X)|0 >) \tag{1.2}$$

(An analagous formula holds for decays). Here, the sums run over the possible angular momentum states X of the initial $Q\bar{Q}$ system and the dimensions d of the operators, and the color singlet and octet terms have been explicitly separated. The short-distance factors $F_{\underline{c}}^d(X)$ are essentially the hard subprocess rates for producing a $Q\bar{Q}$ pair in a given color and angular momentum state and, in principle, are calculable in pQCD to any desired order in $\alpha_s(M)$. The long-distance matrix elements, which represent the probability for the $Q\bar{Q}$ pair to evolve into a color singlet bound state, on the other hand, are nonperturbative parameters of the theory. In the VSM, each of these matrix elements is expanded in powers of the heavy quark velocity according to the velocity scaling rules, and only the most sizable terms are kept [5]. Determining exactly where to truncate the expansion for a given level of accuracy, however, is nontrivial since one must also bear in mind the level of accuracy achieved by the $\alpha_s(M)$ expansion approximation of the $F_{\underline{c}}^d(X)$. Calculations of the short-distance factors to high order in α_s are meaningless unless one has also calculated or otherwise determined to the same order the v-related corrections to the long-distance matrix elements [5].

In order to elucidate the velocity scaling aspect of the VSM, it is necessary to examine in greater detail the matrix elements in Equation 1.2. Writing out a generic matrix element explicitly, one

has:

$$< 0|O_n^H|0 > \;\; = \;\; < 0|\chi^+ K_n \psi (\sum_X \sum_{m_j} |H + X >< H + X|) \psi^+ K_n^{'} \chi|0 > \tag{1.3}$$

Here, the index n replaces the separate indices c and X in Equation 1.2, which describe the $Q\bar{Q}$ state at creation, and the $\psi^+(\psi)$ and $\chi(\chi^+)$ are creation and annihilation operators for heavy quarks and antiquarks, respectively. The $K_n(K_n^{'})$ factors are products of a spin matrix, a color matrix, and a polynomial in the covariant derivative and other fields [5]. Temporarily focusing on color singlet operators only, one can assume that the sum over states X is dominated by the single term $|H >< H|$, resulting in:

$$\begin{aligned} < 0|O_n^H|0 > \;\; &\simeq \;\; < 0|\chi^+ K_n \psi (\sum_{m_j} |H >< H|) \psi^+ K_n^{'} \chi|0 > \\ &\simeq \;\; (2J+1) < 0|\chi^+ K_n \psi|H >< H|\psi^+ K_n^{'} \chi|0 > \\ &\simeq \;\; (2J+1)| < 0|\chi^+ K_n \psi|H > |^2 \\ &\simeq \;\; (2J+1) < H|O_n|H > \end{aligned} \tag{1.4}$$

In the above expressions, rotational invariance of the operators and the vacuum saturation approximation ($1 = \sum_X |X >< X| \simeq |0 >< 0|$) have been invoked. Also, the decay operator $O_n = \chi^+ K_n \psi \psi^+ K_n^{'} \chi$ makes an appearance in the final expression. [1] From examination of the third line in this equation series, it is clear how $< 0|O_n^H|0 >$ is related to the probability for the initial $Q\bar{Q}$ pair to evolve into the final quarkonium state H. Finally, recognizing that a color singlet quarkonium state is a complicated object with a finite probability for containing one or more gluons in addition to two heavy quarks, one can expand the quarkonium state in a series of terms, each of a definite order in the quark velocity, v [3]:

$$\begin{aligned} |H(nJ^{PC}) > \;\; = \;\; & O(1)|Q\bar{Q}(^{2s+1}L_J, \underline{1}) > \\ & + O(v)|Q\bar{Q}(^{2s+1}(L \pm 1)_{J'}, \underline{8})g > \\ & + O(v^2)|Q\bar{Q}(^{2s+1}L_J, \underline{8})gg > + ... \\ & + ... \end{aligned} \tag{1.5}$$

Furthermore, the creation and annihilation operators, the derivatives, and electromagnetic field

[1] For color octet operators, the situation is slightly more complicated since for the production matrix element, the $\sum_X |H+X >< H+X|$ is no longer dominated by the term $|H >< H|$ but rather by $|H+g >< H+g|$. For the decay element, the vacuum saturation approximation no longer applies, and instead one must approximate the sum over a complete set of hadronic states by $\sum_X |X >< X| \simeq |g >< g|$. Thus, the color octet production matrix elements lead to $| < 0|\chi^+ K_n \psi|H + g > |^2$, and the decay matrix elements lead to $| < g|\chi^+ K_n \psi|H > |^2$, which are related by crossing but strictly speaking are independent quantities.

operators in the K_n also have well defined scaling relations with v. For a comprehensive review of the velocity scaling rules see [3] [23]. Mentally substituting the expression 1.5 into 1.4, it becomes clear that the NRQCD production matrix elements are expansions in the parameter v and that the shorthand formula in Equation 1.2 actually implies a simultaneous expansion in α_s and v. It is worth mentioning, however, that the quantities α_s and v are not truly independent for heavy quarkonium systems. The dynamical balance between the kinetic energy ($\frac{Mv^2}{2}$) and the potential energy ($\frac{\alpha_s(\frac{1}{r})}{r} = Mv\alpha_s(Mv)$) leads to the relation:

$$v \approx \alpha_s(Mv) \tag{1.6}$$

In practice only a finite number of terms contribute at a given order to the production cross-section or decay rate of a quarkonium state in a particular process. As has been mentioned, exactly where the expansions are truncated is largely dictated by the velocity scaling rules after establishing the desired level of accuracy of the calculations. As pointed out in [5], however, one must also be aware that the $F_{\underline{c}}^d(X)$'s depend not only on α_s but also on dimensionless ratios of kinematic quantities, which can also influence which terms must be included in a specific calculation. In most cases, the color singlet predictions are recovered using the leading order estimates calculated within the VSM framework. One notable exception to this rule is the case of P-wave charmonium production and decays for which the leading order color singlet prediction involves just a single term related to $< 0|O_1^\chi(^3P_J)|0 >$, or equivalently, the derivative of the P-wave charmonium radial wave function at the origin [13] [4] [20] [3]. The VSM calculation, on the other hand, includes not only this contribution but also an additional contribution at the same order in v^2 through the matrix element $< 0|O_8^\chi(^3S_1)|0 >$ [22] [21]. As pointed out by Bodwin, Braaten, and Lepage, the inclusion of this second term is absolutely necessary for perturbative consistency, and its absence in previous CSM calculations led directly to the observed infrared divergences noted before.

The elimination of the χ_c divergences and the logical explanation of their presence in CSM results was the first successful application of the VSM, and the direct consequence of this initial success was the publication in subsequent years of a virtual flood of papers on the VSM. Bodwin, Braaten, and Lepage further clarified the theoretical underpinnings of the model and worked out many of its important implications [5]. Other authors carried out detailed analyses of heavy quarkonium production and decays using the BBL formalism and used data from fixed-target experiments, HERA, and the Tevatron to measure various individual production matrix elements and linear combinations of matrix elements [24] [25] [26] [27] [28] [29] [30] [31] [32] [33] [34] [35] [36] [37].

The process of determining the matrix elements is still in its infancy, and perhaps not surprisingly, the results are still somewhat confusing. Recently, Cho and Leibovich have determined many matrix elements for J, ψ', and the upsilon states for the very first time by performing fits to the Tevatron

data at high p_t [33] [34]. The values of most of these matrix elements have yet to be confirmed with data from other experiments. However, in at least one case there exists data from another facility which provides complementary matrix element information to that from the Tevatron, and early indications are that there might be inconsistencies. Using the Tevatron data, Cho and Leibovich have evaluated the following linear combination [34]:

$$\frac{<0|O_8^J(^1S_0)|0>}{3} + \frac{<0|O_8^J(^3P_0)|0>}{M_c^2} = (2.2 \pm 0.5) \times 10^{-2}\ \text{GeV}^3 \tag{1.7}$$

Meanwhile, Amundson, Fleming, and Maksymyk have performed a fit to data taken at fixed-target experiments as well as HERA and measured a different linear combination of these matrix elements [36]:

$$\theta = <0|O_8^J(^1S_0)|0> + \frac{7}{M_c^2} <0|O_8^J(^3P_0)|0> = (2.0 \pm 0.1) \times 10^{-2}\ \text{GeV}^3 \tag{1.8}$$

Solving these two linear equations for the individual matrix elements, one arrives at the disconcerting result that $<0|O_8^J(^3P_0)|0>$ is negatively valued. This has caused at least two groups of theoreticians/phenomenologists to conclude that the measurements are incompatible, a conclusion based on the assumption that all of the NRQCD matrix elements are necessarily positive definite [35] [36]. Both groups emphasize, however, that higher-order corrections, which are currently lacking in the literature, could possibly resolve the apparent discrepancy. One of the authors from [36], though, has recently backed away from the initial conclusions that the measurements are at odds by pointing out that matrix elements of dimension-8 operators like $O_8^J(^3P_J)$ need not have positive values [37]. Regardless, the determination of the NRQCD matrix elements has begun in earnest, and the reliability of such measurements will certainly improve over time as production calculations become increasingly sophisticated and experience with the VSM is acquired.

1.2.3 Color Evaporation Model

The final model which has been used to describe heavy quarkonium, the Color Evaporation Model (CEM), actually predates the other two models. Like the CSM, the CEM is rather simple conceptually, but the two models are opposites in terms of their treatment of color. As has been previously noted, in the CSM not only the $Q\bar{Q}$ production but also the color neutralization is assumed to take place at the short-distance perturbative scale. The CEM, on the other hand, pictures the transformation of $Q\bar{Q}$ pairs into color singlet bound states as a process involving multiple gluon interactions over a long-distance scale. It is also instructive to compare and contrast the CEM with the VSM. The CEM is similar to the VSM in that color octet $Q\bar{Q}$ states are included at the production scale, but the VSM considers the bleeding away of color via gluon interactions as suppressed by factors

of the heavy quark velocity, v. Such gluon interactions are an integral part of the CEM, however, and are expected to be prevalent. Another difference which proponents of the CEM often point out is that there are far fewer non-perturbative parameters in the CEM that must be experimentally determined. Hence, according to some the CEM inherently possesses greater predictive power as a theory. Unfortunately, the CEM can only be used to describe quarkonium production in cases where the heavy quarks are produced directly from a vector boson like a photon, gluon, or Z, which mediates the interaction and does not apply to one of the most common charmonium production mechanisms, b-hadron decay.

In the same spirit as the other two models, the description of heavy $Q\bar{Q}$ production in the CEM involves the separation of the short-distance $Q\bar{Q}$ production scale from the long-distance scale of bound state formation. Basically, the CEM relates the bound state heavy quarkonium cross-section to the subthreshold cross-section for producing $Q\bar{Q}$ pairs. In older versions of the model this relation was a strict equality [8] [38] [39] [40], but modern versions of the model also allow for a contribution from open heavy Q states where the extra energy required to form $Q\bar{q}$ and $\bar{Q}q$ mesons is obtained via complicated interactions with the color field in the region of the collision point [3] [6] [7]. This open contribution is now known to account for over 50% of the total subthreshold $Q\bar{Q}$ cross-section. For illustrative purposes, the equations defining $c\bar{c}$ production in the context of the CEM are given below:

$$\sigma_{c\bar{c}}^{\text{subthreshold}} = \sigma_{\text{open}}^{\text{subthreshold}} + \sigma_{\text{onium}} = \int_{4m_c^2}^{4m_D^2} dQ^2 \frac{d\sigma_{c\bar{c}}}{dQ^2} \tag{1.9}$$

$$\sigma_{\text{onium}} = \sum_X \sigma_{\text{onium}}(X) = \sum_X F(X) \int_{4m_c^2}^{4m_D^2} dQ^2 \frac{d\sigma_{c\bar{c}}}{dQ^2} \tag{1.10}$$

In Equations 1.9 and 1.10 $d\sigma_{c\bar{c}}/dQ^2$ is a process-dependent cross-section which can be calculated using pQCD. Also, the sum in Equation 1.10 runs over the entire set $\{X\}$ of subthreshold $c\bar{c}$ bound states. The $F(X)$ are simply constants which are different for individual quarkonium states, are process independent, and must be determined from experiment. In at least one version of the model, σ_{onium} accounts for exactly 1/9 of the total subthreshold $c\bar{c}$ production, with open charm production making up the remainder [41] [42]. According to the authors of [41] [42], the factor 1/9 follows from a simple statistical treatment of color. Other authors have challenged this notion, however, and in competing versions of the CEM no concrete predictions are made regarding the relative sizes of subthreshold open and bound state charm production [3] [6] [7]. Hence, there are really just two general predictions of the CEM. First, the dependence of $\sigma_{c\bar{c}}$, σ_{onium}, and σ_{open} on a given dynamical variable like $\sqrt{s}$, x_f, or p_t is universal, and second, the fractions $F(X)$ are independent of the collision process.

Recently, a number of authors have reexamined the CEM, breathing new life into this theory, which was essentially abandoned nearly twenty years ago for no apparently compelling reason. In

these critical reviews, they show that the CEM predictions are in very good agreement for a variety of different production processes over wide kinematic ranges. For example, the shapes of the $\sigma(E_\gamma)$'s for photoproduced bound states and open charm states overlap to a remarkable degree once they have been normalized to one another [41]. Similar results are found for hadroproduced bound and open charm states [41]. The CEM also correctly reproduces the shapes of the J production cross-section for pN and πN collisions; the J longitudinal momentum distributions for pN, πN, and $\bar{\text{p}}$N interactions; total J, prompt J, and χ_c $\text{d}\sigma(\text{p}_\text{t})/\text{dp}_\text{t}$ distributions at CDF; and a host of other distributions as well [6] [7]. In addition to production cross-section and differential cross-section shapes, absolute magnitudes of these quantities have been shown to follow CEM predictions once a few non-perturbative parameters have been determined. In [41] the authors use photoproduction data to measure $F(J) = 0.045$ for a given set of parton distribution functions (PDF's) at certain mass scales. [2] Using this $F(J)$ and K factors (fudge factors which represent ignorance of higher order QCD corrections) determined by rescaling the NLO prediction for open charm hadroproduction to agree with observed open charm data, absolute predictions for bound state production are made which match the data perfectly [41]. Lastly, tests of the CEM have been made regarding the constancy of the production ratios of various heavy quarkonium states. $\sigma_\chi/\sigma_J = 0.4$, for example, has been shown to hold from $\sqrt{\text{s}} = 8$ GeV up to $\sqrt{\text{s}} = 60$ GeV. Likewise, $\sigma_{\psi'}/\sigma_J = 0.14$ holds from $\sqrt{\text{s}} = 15$ GeV to $\sqrt{\text{s}} = 60$ GeV, and it has also been demonstrated that this ratio is independent of the atomic number A in fixed target experiments [3] [6]. Thus, in a wide range of environments and kinematic regions the CEM provides a reliable description of heavy quarkonium production.

Still, despite its overall success, there are indications that the CEM might not be the complete solution to heavy quarkonium. The NA14 Experiment at CERN, for example, has published an upper limit of $\sigma_\chi/\sigma_J \leq 0.08$ based on its photoproduction data [43] [7]. Most other experiments, however, using proton and pion beams support a σ_χ/σ_J ratio close to 0.4 [3] [6]. The CEM predicts that the ratios should be independent of the collision process and therefore identical, but it does not seem to be the case in this instance. Recently, analysis of high energy data taken at the Tevatron by CDF has uncovered yet another curiosity. The $\sigma_{\psi'}/\sigma_J$ ratio at $\sqrt{s} = 1.8$ TeV is substantially higher (0.2) than at lower energies (0.14). Closer inspection of the ratio as a function of p_t reveals a gradual increase with p_t [7]. In other words, the shapes of $\sigma_{\psi'}(\text{p}_\text{t})$ and $\sigma_J(\text{p}_\text{t})$ are not the same, in stark violation of the tenets of the CEM. Whether this observation is due to some systematic effect or is, in fact, indicative of some underlying physics remains to be seen. In any event, these two irregularities represent a serious challenge to the CEM.

[2] It should be mentioned here that while other authors have determined $F(J) = 0.025$ using fixed-target data, this does not represent a failure of the theory since different PDF's and mass scales were used and the NLO calculations for production processes are highly dependent on the choice of PDF's and mass scales [3] [6] [7].

1.2.4 Theoretical Model Summary

In summary, there are three theoretical models of heavy quarkonium production today: the Color Singlet model, the Velocity Scaling Model, and the Color Evaporation Model. The CSM and VSM provide a similar description of the production process, involving the creation of a $Q\bar{Q}$ pair at the short distance scale followed by the evolution of the pair into a final state quarkonium. The VSM, however, can be viewed as a generalization of the CSM in which not only color singlet initial states are important but color octet initial states take part as well. In addition, the VSM provides a sophisticated mathematical formalism together with well motivated velocity scaling rules for use in calculating rates. When the CSM was first used in the late 1970's and early 1980's, its expectations compared reasonably well with the available experimental data. More recent results at higher energies, however, suggest that the more general assumptions of the VSM are required to describe production data well. The third and final model, the CEM, is also able to explain the bulk of heavy quarkonium production data, but it has a very different flavor than the CSM and VSM. In terms of physics, it is more closely related to the VSM since color octet initial states contribute to final state quarkonia production, but the approach to describing the bleeding off of color is quite different. In the CEM, soft gluon exchange is assumed to be common, obviating the need to consider color at all. While VSM calculations involve numerous terms, each with an assigned relevance based on the velocity scaling rules, CEM calculations are much simpler and more phenomenological. One has only a small set of universal constants in the CEM, and once their values are determined using one process, predictions can be made for any other. The predictions of each of these models for J production at LEP will be examined in the next section (see Table 1.1). Which of the competing descriptions best explains all of the available heavy quarkonium data, including that from the LEP experiments, is still an open question, and it will be the task of future theoreticians and experimenters to resolve the matter.

1.3 Expectations at the Z Peak

1.3.1 General

Having described the basics of the models commonly applied to heavy quarkonium production, the obvious next step is to examine their predictions for quarkonium production in e^+e^- collisions at $\sqrt{s} = 91$ GeV. At LEP, charmonium production is strongly dominated by the b-hadron decay mechanism, accounting for 90% to 97% of the total charmonium sample. Only a 3% to 10% contribution is expected from the prompt QCD processes of charm fragmentation, gluon radiation, and gluon fragmentation, but it is precisely this small fraction which is the most interesting. The lower bound of this prompt fraction range is given by the CSM, the upper bound is given by the VSM, and the

CEM prediction lies in between. Hence, a measurement of the prompt fraction has the potential to distinguish among these various models. Because there is no corresponding top-hadron decay mechanism, production of upsilon states can only proceed through the QCD processes analagous to those just mentioned for charmonium states. Therefore, upsilons are unlikely to be observed in significant numbers even with the full LEP I statistics. The term "prompt" used in the context of charmonium production to label the processes of charm fragmentation, gluon fragmentation, and gluon radiation, means that the origin of the resulting charmonium states and the collision vertex cannot be distinguished by a microvertex detector [9]. In practical terms, at LEP only events which do not involve b-quarks between the Z decay point and the heavy quarkonium production point are considered prompt. With this understanding, heavy quarkonium production via gluon fragmentation is not always, strictly speaking, a prompt process because the gluon can be emitted from a long-lived $b(\bar{b})$ quark in $Z \rightarrow b\bar{b}$ decay. Still, it is typically referred to as a prompt process since $b\bar{b}$ decays account for only 22% of all hadronic Z decays. Furthermore, the term "direct" will be used to refer to all heavy quarkonium states not produced from the decay of higher radial or angular momentum states.

1.3.2 Prompt Quarkonium Production

While prompt quarkonium production is expected to represent only a tiny portion of overall quarkonium production at LEP, it is very interesting experimentally because this small sample can shed light on the role of color during the production process. Unfortunately, theoretical calculations of the various subprocess rates come with fairly large uncertainties, and consequently, all of the theoretical results in this section have been assigned a uniform 50% error (see previous section Quarkonium Production and Decay Models). Aside from the generally accepted fact that prompt quarkonium production constitutes only a small part of the total heavy quarkonium production in e^+e^- collisions, little else has been verified. In the literature, three fundamental processes have been considered to contribute to prompt quarkonia production at LEP energies: c-quark fragmentation, gluon fragmentation, and gluon radiation. Upper limits on some of these processes have been established, but to date only one measurement $Br(Z \rightarrow J_{prompt} + X) = (1.9 \pm 0.7 \pm 0.5 \pm 0.5) \times 10^{-4}$ has actually been made at LEP [44] [45] [46]. More comprehensive studies have been performed at the Tevatron using CDF's large samples of heavy quarkonium states and also at HERA and numerous fixed-target facilities [33] [34] [35] [36] [37] [47]. Not all of these measurements are clearly understood yet, however, and as noted already, some even seem to contradict one another when viewed within the VSM framework. Still, work is progressing at an extreme pace in this very active area of high energy physics, and one can only hope that a unified picture of heavy quarkonium production will soon emerge.

Within the CSM the single largest contribution to prompt charmonium production is from charm

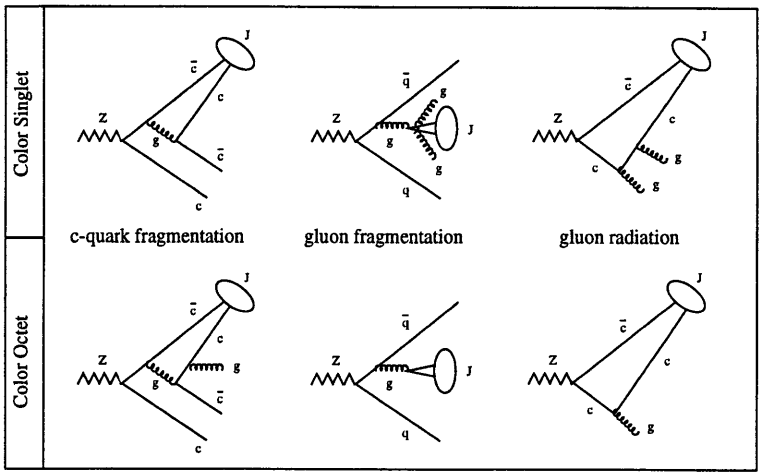

Figure 1-1: Prompt J production mechanisms
The color singlet (upper row) and color octet (lower row) Feynman diagrams illustrating the three main mechanisms for prompt J production in Z decays.

fragmentation. This process was first calculated in 1990 and again in 1993, with consistent results using a consistent set of input parameters (α_s, $|R(0)|^2$, etc.) [11] [12]. Using the fragmentation function derived in [12], $Br(Z \rightarrow c\bar{c}) = 0.11 \pm 0.007$, modern estimates of the radial wave functions $|R^J(0)|^2$ and $|R^{\psi'}(0)|^2$, and including feeddown from ψ', one can derive $Br(Z \rightarrow Jc\bar{c}) = (6.7 \pm 3.3) \times 10^{-5}$ [48] [29] [49] [30]. Next in importance is the process of gluon fragmentation which has been analyzed by two independent groups. Initial calculations of the rate due to this mechanism were anomalously high and were later found to be in error by factors of 4π [50] [51]. The corrected calculations yield $Br(Z \rightarrow Jq\bar{q}gg) = (2.3 \pm 1.2) \times 10^{-5}$ and are dominated by direct production of χ_c^1 and χ_c^2 states which subsequently decay into J's. This is in accord with Braaten and Yuan, who found a rather low probability for a J to be directly produced during gluon fragmentation [52]. The least important of the prompt charmonium production mechanisms, gluon radiation, was actually the first to be considered by theorists. Borrowing the formula obtained by Keung and substituting an improved value of $|R^J(0)|^2 = 1.02\ GeV^3$, one can estimate $Br(Z \rightarrow Jgg) = (6.1 \pm 3.0) \times 10^{-7}$, which is miniscule in comparison to the other prompt contributions [48] [53]. Thus, in the CSM after adding together these three contributions one expects an approximate branching ratio of $Br(Z \rightarrow J_{prompt} + X) = (9.1 \pm 4) \times 10^{-5}$.

According to the VSM, however, a significantly larger prompt J production rate is expected because of color octet contributions to the processes of charm fragmentation, gluon fragmentation, and gluon radiation. In this case gluon fragmentation now dominates over c-quark fragmentation, and the gluon radiation contribution remains negligible. Recent determinations of the color octet matrix elements used to define production rates in the VSM lead to $Br(Z \rightarrow Jq\bar{q})_{octet} = (1.9 \pm 1.0) \times 10^{-4}$ [33] [34] [29] [31]. Both the short- and long-distance parts of the color octet terms contributing

Production Mechanism	$Br(Z \rightarrow J + X)_{CSM}$	$Br(Z \rightarrow J + X)_{VSM}$	$Br(Z \rightarrow J + X)_{CEM}$
c-fragmentation	6.7×10^{-5}	6.7×10^{-5}	–
g-fragmentation	2.3×10^{-5}	2.1×10^{-4}	–
g-radiation	6.1×10^{-7}	7.0×10^{-7}	–
TOTAL	9.1×10^{-5}	2.8×10^{-4}	$\geq 1.8 \times 10^{-4}$

Table 1.1: Prompt J branching ratio predictions
Predictions of prompt J production for various processes in the CSM, VSM, and CEM.

to the charm fragmentation process have been found to be suppressed relative to their color singlet counterparts, resulting in the tiny branching ratio $Br(Z \rightarrow Jc\bar{c})_{octet} = (1.1 \pm 0.6) \times 10^{-7}$ [29]. Likewise, the color octet diagrams for the gluon radiation process have proved unimportant, with the latest calculations, yielding $Br(Z \rightarrow J + g)_{octet} = (9.0 \pm 4.5) \times 10^{-8}$ [29]. Thus, color octet diagrams not only show that gluon fragmentation assumes the leading role in prompt J production, but the rates actually become sizable enough to render conceivable the detection and measurement of prompt J's amid the large b-hadron decay J background.

It has also been demonstrated that rates for prompt J production higher than those in the CSM are expected in the CEM. Recently, Gregores, Halzen, and Eboli, have given the CEM prediction $Br(Z \rightarrow J_{prompt} + X) = (1.8 \pm 0.9) \times 10^{-4}$, which does not include feeddown from higher radial and angular momentum states [54]. Given the non-negligible errors associated with the VSM and CEM calculations, the model predictions for the rate of prompt J production are consistent. Moreover, it has been pointed out that the prompt J momentum spectrum is very much the same in the two models and, therefore, cannot be used to distinguish between them [54]. This similarity of predictions, in fact, is quite general, making it difficult to differentiate the two competing descriptions. A possible exception to this are the predictions for prompt J spin alignment. If the CEM approach is correct, then one expects that the final state J's will be unaligned since any initial alignment should be diluted via multiple gluon interactions [54] [41]. Such non-alignment would probably be difficult to explain in the VSM, however, though the VSM spin alignment predictions are still somewhat controversial [54] [41] [55] [56]. Unfortunately, at LEP there is no chance to measure the spin alignment of prompt J's due to insufficient statistics. At best, one can only realistically hope to observe a small overall excess of prompt J's above the expected b-hadron decay J background.

1.3.3 B-hadron Decay

As noted previously, b-hadrons are the most important source of charmonium states in e^+e^- collisions at the Z peak. One of the first LO calculations of $Br(b \rightarrow J + X)$ was performed by Kühn, Nussinov, and Rückl in 1980, yielding the theoretical result $Br(b \rightarrow J + X)_{direct} = (0.2 - 17.0)\%$ [13]. A similar and consistent calculation was carried out in [14]. The large range of variation

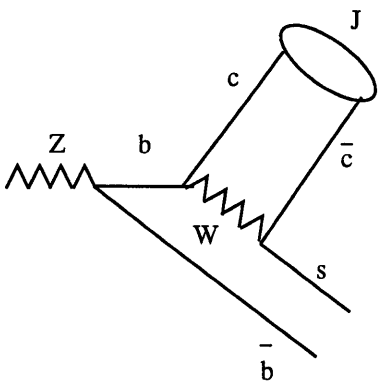

Figure 1-2: b decay to the J
Feynman diagram illustrating the b decay mechanism of J production in Z decays.

given here was a consequence of uncertainties at the time regarding two fundamental aspects of the process: color suppression and QCD corrections to the weak hamiltonian mediating the b-quark decay. Color suppression becomes a factor when one demands that the $c\bar{c}$ pair initially be in a color singlet state (CSM). By 1984 the first measurement of $Br(b \rightarrow J + X)$ had been made, and the relatively small size of $Br(b \rightarrow J + X)_{total} = (1.0 \pm 0.5)\%$ was taken as an indication of the action of color suppression [57]. Still, despite the large experimental errors, the branching ratio was not as small as expected assuming the validity of both color suppression and QCD corrections, and from the papers published at the time, one senses that the physics community involved in this research expected that subsequent measurements of $Br(b \rightarrow J + X)_{total}$ would eventually drop the accepted value well below 1%, signifying a critical victory for QCD. Nonetheless, it was already realized at this point that the LO calculation was itself on somewhat shaky ground due to the strong color suppression of the Born level diagram and the extreme scale dependence of the QCD corrections to the weak hamiltonian [58]. Consequently, a NLO analysis of this process was performed, but unfortunately, this attempt was flawed because the renormalization group was not treated properly [59] [22]. Not until 1994 were these problems finally rectified and a new calculation carried out. From this work it was observed that the strong scale dependence persisted even at NLO, making a reliable prediction difficult. Regardless, the authors concluded that their NLO calculation suggested a rate at least as suppressed as that given by the LO result [59]. Another conceivable explanation for the observed excess of $b \rightarrow J$ decays relative to theoretical expectations was enhancement of J's due to feeddown from known higher states. (Scenarios involving feeddown from as yet undiscovered states has also been considered in the literature [60].) This possibility was explored in 1992 in a landmark paper presenting improved estimates of χ_c production, one of the first applications of the VSM formalism [22]. In this paper, the authors first present their prediction $Br(b \rightarrow J + X)_{direct} = 0.23\%$, a result in agreement with previous LO predictions, and then they

take the measured $\mathrm{Br}(b \to J + X)_{\mathrm{total-exp}} = (1.12 \pm 0.16)\%$ from CLEO II to deduce the value for $\mathrm{Br}(b \to J + X)_{\mathrm{direct-exp}}$ by appropriately accounting for feeddown from directly produced ψ' and χ_c states [22] [61] Their determination of $\mathrm{Br}(b \to J + X)_{\mathrm{direct-exp}} = (0.71 \pm 0.20)\%$ is still 2.5σ from the calculated value, leading them to conclude that the order-α_s corrections are potentially important. Using the newer and more precise values of the branching ratios to ψ' and χ_c states measured by CLEO II, $\mathrm{Br}(b \to J + X)_{\mathrm{direct-exp}}$ is actually closer to 0.79%. The most complete and up to date estimate of $\mathrm{Br}(b \to J + X)$ is derived using the VSM/BBL framework and includes relativistic and radiative corrections as well as one color octet term. While the first of these was determined to be negligible, the latter two were found to augment the base result in [22] by 80% and 76%, respectively. The final prediction $\mathrm{Br}(b \to J + X)_{\mathrm{direct}} = 0.58\%$ brings the theory more comfortably close to experiment [24]. It should be emphasized, however, that only one of many color octet terms was included in this calculation, and the corresponding matrix element was taken from an early fit to the Tevatron data [33]. A more refined fit, yielding estimates not only of $< 0|O_8^J(^3S_1)|0 >$ but also of a linear combination of the matrix elements $< 0|O_8^J(^1S_0)|0 >$ and $< 0|O_8^J(^3P_0)|0 >$, lead to far larger values of $\mathrm{Br}(b \to J + X)_{\mathrm{direct}}$, overshooting the present best experimental value from CLEO II [34] [35]. Thus, it must be affirmed that at the present time estimates of $\mathrm{Br}(b \to J + X)_{\mathrm{direct}}$ continue to be in a state of flux and that extremely reliable calculations of this branching ratio do not yet exist.

In addition to J's, ψ''s and χ_c's have been studied as well in the process of b-hadron decay. Because the calculations for ψ' and the J are essentially identical, the focus in the past has been on J's, and results have not always been presented separately for ψ'. This is especially true for the papers which treat the more complicated aspects of the charmonium production problem such as NLO terms, relativistic and radiative corrections, and color octet terms. One of the earliest published results regarding ψ' production was the ratio $\mathrm{Br}(b \to \psi' + X)_{\mathrm{direct}}/\mathrm{Br}(b \to J + X)_{\mathrm{direct}} = 0.31$, which in the CSM is given approximately by the ratio of the electronic widths $\Gamma_{\psi' \to e^+e^-}/\Gamma_{J \to e^+e^-}$ [13]. This result holds to lowest order in the VSM as well [22]. Improved measurements of the widths have resulted in the updated expectation $\mathrm{Br}(b \to \psi' + X)_{\mathrm{direct}}/\mathrm{Br}(b \to J + X)_{\mathrm{direct}} = 0.40$, and experimental results from CLEO II are in excellent accord with this value. After accounting for feeddown from ψ', χ_c^1, and χ_c^2 states to final state J's, one can obtain from the CLEO II measurements $\mathrm{Br}(b \to \psi' + X)_{\mathrm{direct}}/\mathrm{Br}(b \to J + X)_{\mathrm{direct}} = (0.43 \pm 0.08)$ [61]. Such agreement is actually quite surprising since the individual branching ratios are not well estimated by the theory and the theoretical ratio is given by leading order calculations only. It might simply be accidental, but perhaps it actually confirms the hypothesis that regardless of the explanation for the apparent theoretical deficit/experimental excess for $\mathrm{Br}(b \to J + X)_{\mathrm{direct}}$ and $\mathrm{Br}(b \to \psi' + X)_{\mathrm{direct}}$ (higher order contributions, color octet terms, radiative and relativistic corrections, etc.) both J's and ψ''s are affected in the same way and to the same extent. In contrast, χ_c's are actually very different from J's from a calculational standpoint.

As already noted, early attempts to accurately describe χ_c production were suspect due to infrared divergences. Despite this flaw, the CSM predicted that in the process of b-quark fragmentation χ_c^1 states would be nearly as common as ψ''s and that decays to χ_c^0 and χ_c^2 would be forbidden [13]. The first rigorous theoretical predictions were not available until the emergence of the VSM, however. In 1992 in one of the first applications of the VSM, Bodwin, Braaten, and Lepage published estimates for J, h_c, and χ_c production which relied on the non-perturbative parameters G_1, H_1, and H_8'. G_1 is directly proportional to the electronic decay width of the J and has a value of 108 MeV [22]. In an earlier paper the same authors used the VSM formalism and the experimental widths of χ_c^1 and χ_c^2 to light hadrons to fix the parameter $H_1 = (15.3 \pm 3.7 \pm 5.5)$ MeV [21]. The final parameter, H_8', can be determined using the VSM calculations and the recent χ_c^1 and χ_c^2 production measurements published by CLEO II [61]. Setting $M_b = 5.0$ GeV and $Br(b \to \ell\nu X) = (10.75 \pm 0.25)\%$, one can obtain two separate estimates of this quantity: $H_8' = (1.4 \pm 0.6)$ MeV and $H_8' = (3.2 \pm 0.8)$ MeV. While these values are not in particularly good agreement, they are still consistent, especially considering the fact that the theoretical errors, which have not been included here, are still quite large. From this exercise, however, it must be concluded that where χ_c production is concerned, experiment and the VSM theory have not yet reached a level of precision which invites meaningful comparison.

1.3.4 Summary

To conclude, the general picture of heavy quarkonium production at LEP energies is fixed both theoretically and experimentally. Upsilon states are highly suppressed and probably unobservable with the LEP I statistics. Charmonium states, on the other hand, are found in far greater numbers, with a dominant fraction coming from b-hadron decay and a subordinate but perhaps detectable contribution coming from one or two prompt mechanisms. The details of this picture, however, are far from clear, particularly concerning the size and composition of the prompt J sample. If the CSM is used to calculate rates, one expects a smaller prompt J sample in which charm fragmentation dominates gluon fragmentation, but this expectation is reversed if the VSM is used. The situation is confused further when the CEM is considered since there are no published predictions regarding the composition, and the overall prompt rate is comparable to that of the VSM. Even the rate of J production from b-hadron decay is not known precisely from a theoretical point of view, although it is fairly well known experimentally from previous measurements of total J production at LEP, CESR, and other facilities. Given this current theoretical uncertainty regarding heavy quarkonium production, which applies not only in e^+e^- collisions but in other contexts as well, it is imperative to make as many production measurements in as many environments as possible. Performing such analyses using the L3 detector will be the focus of the remainder of this thesis, providing a few more pieces to the heavy quarkonium jigsaw puzzle.

Chapter 2

Experimental Facilities

2.1 CERN

The research described in this thesis was performed at the European Center for High Energy Physics (CERN), located on the outskirts of Geneva, Switzerland. CERN is Europe's premier research complex for investigations in the field of high energy physics. It was established in 1955, and in addition to having a long history, it has an illustrious one as well. Experiments carried out at CERN were the first to observe jet structure in proton-antiproton collisions, weak neutral currents, and W and Z bosons, and to measure in detail the properties of the Z boson [62] [63]. The precision electroweak (EW) measurements at the Z pole were made possible with the construction in the late 1980's of CERN's Large Electron Positron Collider (LEP). This synchrotron is approximately 27 km in circumference, and in 1998 it is still the largest collider in existence today. The LEP electrons and positrons originate in the LEP Injector Linacs (LIL) and are subsequently transferred to the Electron Positron Accumulator (EPA), where they are temporarily stored while the particle bunches achieve sufficient luminosity. Once enough electrons and positrons have been accumulated, the bunches are transferred to the old Proton Synchrotron (PS) and then to the Super Proton Synchrotron (SPS) for various stages of pre-acceleration before being injected into the main LEP ring. At this point the energy of the bunches is boosted by the two LEP RF cavities to 45.6 GeV, which is roughly one-half of the mass of the Z boson. For the next several hours after being accelerated to this energy, the electron and positron beams are made to cross at four points spaced uniformly around the LEP ring, and copious quantities of Z's are produced. When the beam luminosity dwindles to an optimum threshold, determined by maximizing the time averaged luminosity, the beams are dumped, and the beam filling cycle repeats.

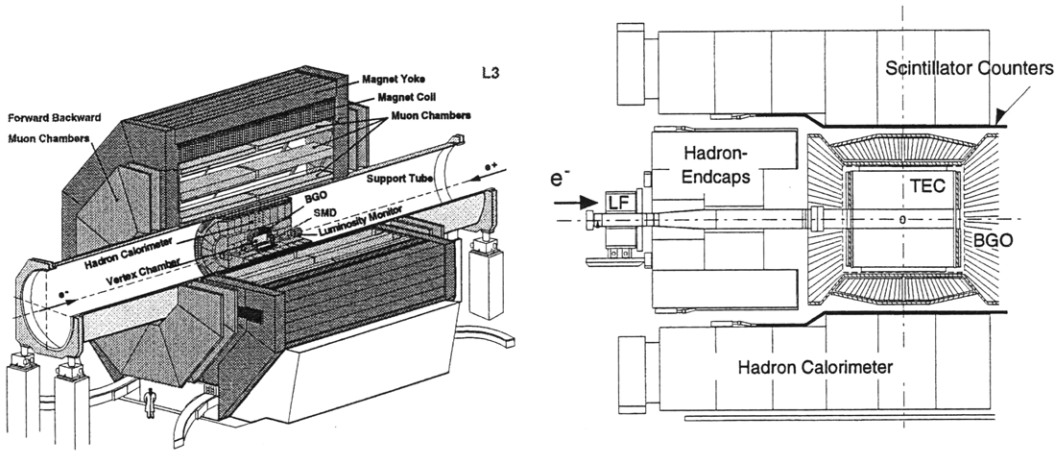

Figure 2-1: L3 Experiment
a) full perspective view and b) inner detector view

2.2 L3

2.2.1 General Description

The bulk of the L3 Experiment was assembled in 1988-89 in a cavern located 50 m underground at the first of four bunch crossing points (second of eight access points) distributed around the LEP ring. It is a multi-purpose high energy physics detector containing a central tracker, an electromagnetic calorimeter, scintillators, a hadronic calorimeter, and a precision muon chamber system, all contained within a large solenoidal magnet. Additional subdetectors were added in subsequent years, most notably the electromagnetic calorimeter endcaps, the forward-backward muon chambers, and the silicon microvertex detector. These various systems operating together allow L3 to measure isolated electrons and photons, muons, and jets extremely well.

2.2.2 Tracker System

The L3 tracking system consists of two semi-independent subdetectors: the time-expansion chamber (TEC) and the silicon microvertex detector (SMD) (usable since 1994). The SMD is the first of the L3 subdetectors to detect the passage of particles emerging from Z decays at the interaction point (IP) as it is situated directly outside the beryllium beam pipe. SMD coverage is nearly 2π in ϕ and goes down to $|cos(\theta)| \leq 0.93$. It is composed of two layers of sensitive silicon sensors located at radial distances of 6.1 cm and 7.8 cm from the beam, and each layer is made up of twelve slightly overlapping units called ladders [64]. The ladders, in turn, consist of four instrumented and double-sided silicon wafers which yield measurements in three dimensions. The experimental spatial resolution of the device is 7.0μm in r-ϕ and 14.3μm along z [65]. Therefore, the SMD is well-suited

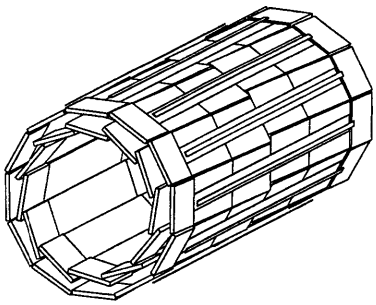

Figure 2-2: Silicon microvertex detector
Perspective view of L3's SMD.

to the task of distinguishing between tracks which emerge directly from Z decays at the IP and those produced from longer-lived particles, which are just slightly displaced from the IP (as in $b\bar{b}$ and $\tau^+\tau^-$ events).

Working with the SMD to measure tracks is L3's time-expansion chamber (TEC). The TEC is a high precision gas drift detector situated outside the SMD and extending to a distance of 48 cm from the beam. Azimuthal coverage is efficient and complete except for very small regions near the TEC wire planes, and tracks can be reconstructed down to about $|cos(\theta)| \leq 0.9$. The TEC is composed of an inner TEC vessel with 12 sectors and an outer TEC vessel with 24 sectors [66]. Each sector

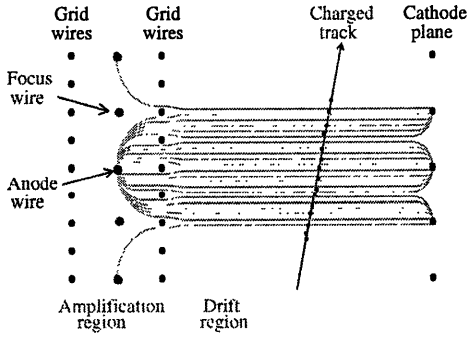

Figure 2-3: Time expansion chamber
A view of the drift of ionization electrons in a single TEC sector caused by the passage of a charged particle.

has an identical design with an anode wire plane, a cathode wire plane, and a grid plane separating the drift region from the amplification region near the anodes. The inner TEC sectors each have 8 wires, the outer TEC sectors have 54 wires, and 14 of the anode wires in each outer sector provide a

differential pickup signal using the grid wires for resolving the left/right ambiguity for each track [66]. The single-wire hit efficiency is roughly 85% for inner TEC anodes and 95% for outer TEC anodes. In addition, the single-wire resolution has been measured to be between 40μm and 100μm in the drift region (91.3% of ϕ coverage), a constant 220μm in the amplification region (6.5% of ϕ coverage), and roughly 140μm very near the cathode plane (2.2% of ϕ coverage) [67]. Lastly, the empirical momentum resolution of the tracks reconstructed using the TEC is approximately $0.018 \times p_t$ [68].

The TEC mode of operation is quite clever and worth describing in greater detail. The time-expansion principle suggests detector designs that employ low drift fields (low drift velocities), yielding signal pulses on the anode wires which in the time domain are not sharp spikes but instead are extended distributions. With the former, the signal arrival time is estimated basically using only the leading edge of the pulse to which only a limited fraction of the total number of ionization electrons contribute. The advantage of the time-expansion method is that the signal arrival time can be estimated by using the center of gravity of the timing distribution. Hence, more of the available pulse information is utilized than just the leading edge, resulting in an improved measurement. In practice, there are several critical features of the TEC which allow it to operate in time-expansion mode. First, the TEC uses a gas mixture of 80% CO_2 with 20% iC_4H_{10}, which has inherently low longitudinal diffusion [66]. Without such low diffusion the advantage of the time-expansion mode would be eliminated by the degradation of the signal pulse. In addition, this particular gas mixture also has the desired feature of having a low Lorentz angle at the TEC working point. Finally, it should be mentioned that the measurement technique requires a non-trivial shaping of the signals to cancel the ion tails before they are sampled by Flash Analog to Digital Converters (FADC). With this design, the TEC has operated successfully for more than seven years.

2.2.3 Calorimeter System

The next subdetector beyond the tracking system is L3's electromagnetic calorimeter (ECAL), which is situated between 50 cm and 75 cm from the beam line. The ECAL covers nearly the full azimuth and is composed of a barrel region ($|cos(\theta)| \leq 0.74$) and two endcaps ($0.8 \leq |cos(\theta)| \leq 0.98$ [66]. The primary unit for both regions is a bismuth-germanium-oxide (BGO) crystal in the shape of a truncated pyramid. For the barrel, these crystals are made to point towards the IP and have an inner face cross-section of 2 cm $\times$ 2 cm, an outer face cross section of 2.5 cm $\times$ 2.5 cm to 3 cm $\times$ 3 cm, and a length or depth of 24 cm (22 radiation lengths) [66]. In this region there are 48 crystals along the θ coordinate and 160 along the ϕ coordinate. The BGO angular resolution is on the order of 2 mrad and the energy resolution has been measured to be 5% at 100 MeV and less than 2% above 1 GeV [66]. Thus, the ECAL measures the electromagnetic showers generated by electrons and photons extremely well over a broad energy range. In addition to measuring electrons and photons, the ECAL also serves as the first nuclear interaction length of material for strongly

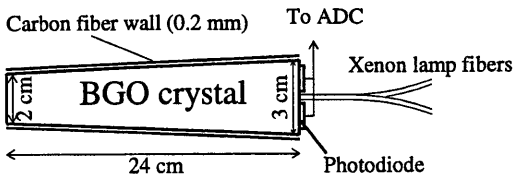

Figure 2-4: BGO crystal
A view of a typical crystal of bismuth germanium oxide like those used in the L3's ECAL.

interacting particles like pions and protons. For the endcaps the crystal dimensions and arrangement are quite different from those used in the barrel, and the energy and angular position resolutions are slightly worse.

L3's ECAL is the first demonstrated large scale use of BGO in a high energy physics experiment. This substance is very attractive as the primary material for an electromagnetic calorimeter because it has reasonable light output while being very dense ($\rho = 7.13 g/cm^3$) [49]. Because bismuth germanium oxide crystals are denser than other crystals commonly used in high energy physics detectors, BGO has a smaller radiation length ($X_0 = 1.12$ cm) and a smaller Moliere radius ($R_M = 2.4$ cm) [49]. (These quantities, of course, are the appropriate length scales for the longitudinal and transverse development of electromagnetic showers, respectively.) The consequences of these shorter length scales are two-fold. First, total containment of electromagnetic showers necessarily requires less material. Thus, a BGO detector can be smaller overall, and even though BGO is quite expensive, the total cost is not prohibitive. Furthermore, since showers in BGO are more localized in the transverse dimensions, smaller crystals can be used, and this ultimately translates into improved angular resolution for electromagnetic bumps. Other nice features of BGO are that it has low afterglow and is not hygroscopic [66]. On the down side, BGO light output is extremely temperature dependent making energy calibration a rather sensitive issue. Still, by making an effort to keep the BGO temperature stable and by properly monitoring the temperature, the adverse effects of the temperature dependence can be reduced to an acceptable level. In general, since the start of LEP, the L3 ECAL has enjoyed remarkable success as an electromagnetic calorimeter and is satisfactory proof that BGO is a viable alternative to traditional substances like NaI, CsI, and lead glass.

Sandwiched between the ECAL and the hadron calorimeter (HCAL) is a large scintillator system. There are 62 scintillators in all - 30 for the barrel and 32 for the forward/backward regions. Each of the barrel scintillators is roughly 2.9 m long and covers about 11.25° in ϕ (except for the 2 barrel

scintillators near the horizontal which cover twice as much area) [66]. The timing resolution has been measured to be 0.55 ns [69]. With this level of performance, the scintillators have two basic functions at L3. The first is to provide fast hit multiplicity information as part of the Level 1 trigger decision. The second is to provide timing information for rejection of cosmic ray muons. Muons from true physics events at the IP take between 2.5 ns and 3.5 ns to reach the scintillators (depending on the polar angle), so using this TOF knowledge together with the timing of a muon's scintillator hit and the timing of the bunch or bunchlet crossing, one can distinguish between 'interesting' muons and cosmic ray muons (which typically arrive out-of-time). Combining this method with a method based on large track DCA's in the TEC, cosmic ray background can be rejected efficiently and reduced to a manageable level.

The second half of L3's calorimeter system, the HCAL, comes next and is a large sampling calorimeter designed for the measurement and containment of hadronic showers. The barrel portion of the detector covers 2π in ϕ and down to $|cos(\theta)| \leq 0.82$, and two endcaps extend the coverage down to $|cos(\theta)| \leq 0.995$ [66]. The barrel region is composed of 9 rings, each with 16 sectors. The sectors in the three central rings are radially thicker than those in the six outer rings (91 cm versus 81 cm), but otherwise the 144 sectors are identical [66]. Each sector is a stack of alternating layers of 0.5 cm thick depleted uranium plates and 1 cm thick brass proportional tubes held in place by a stainless steel frame. Alternating layers of proportional chambers are oriented perpendicular to each other in order to obtain coordinate information in both the ϕ and z directions [66]. As strongly interacting particles like pions and protons pass through the L3 calorimeter system, a hadronic shower will typically be initiated. In the HCAL the secondary particles from the shower will ionize the argon-based drift gas mixture in the brass proportional tubes, and signals will be detected on the anode wires. For the readout, nearby wire signals are summed together into groups referred to as towers. In each sector there are 9 towers in the ϕ direction, 9 in along the z direction, and 10 (8) towers for the inner (outer) sectors in the radial direction [66]. This fine segmentation yields a rather complete 3-dimensional picture of any given hadronic shower that develops in the HCAL. Performance studies have shown that the overall energy resolution of the calorimeter after proper calibration is approximately $(55/\sqrt{E} + 8)\%$ [66]. It should be mentioned that the HCAL endcaps, while having a considerably more complicated geometry and readout, are made of the same materials, operate on the same principles, and have essentially the same level of performance. Furthermore, it should also be mentioned that located between the HCAL barrel and the L3 support tube are several additional centimeters of brass and proportional chambers called the muon filter. While the muon filter is lightly instrumented and can give a few more measurements along the trajectory of a particle which reaches it, its primary purpose, as the name suggests, is to provide an extra nuclear interaction length for preventing strongly interacting particles from entering the muon chambers.

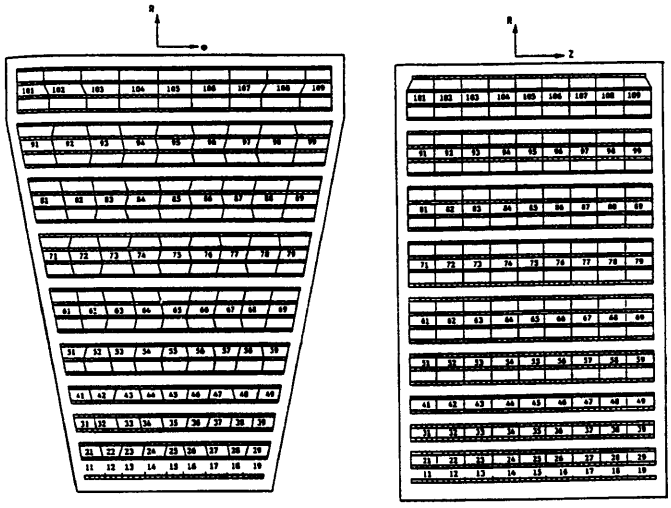

Figure 2-5: Tower structure of a single HCAL module
Views in r-ϕ and r-z of the tower segmentation of the brass proportional tubes in an HCAL sector.

2.2.4 Muon Chamber System

Surrounding the muon filter, one finds a 32 m long, 10 cm thick, stainless steel cylinder known as the support tube. This rigid tube was designed to protect and isolate the inner subdetectors and to support the 172 ton muon chamber system (MUCH). In addition, the support tube serves to align the entire experiment with LEP optics. The MUCH subdetector resides between 2.6 m and 5.4 m from the beam line and employs some 176 gas drift chambers for the measurement of muon directions and momenta [66]. The device is physically separated into 2 ferris wheels, each of which contains 8 octants. These ferris wheels cover 2π in ϕ, and muons can be measured down to $|cos(\theta)| \leq 0.83$ (although the momentum resolution degrades significantly in the range $0.7 \leq |cos(\theta)| \leq 0.83$). Within each octant one finds three layers of drift chambers: an inner layer composed of 1 P-chamber sandwiched between 2 Z-chambers, a middle layer composed of 2 P-chambers, and an outer layer composed of 2 P-chambers each sandwiched between 2 Z-chambers. As the chamber labelling suggests, the MUCH P-chambers are responsible for measuring the p_t of muons traversing the subdetector, and the Z-chambers are responsible for measuring hits along the z direction or, equivalently, muon polar angles. Each Z-chamber contains two layers of drift cells, so a typical muon will have 2 hits in these types of chambers, although for more forward- or backward-moving muons 3 or even more hits are possible. Not all of the P-chambers are identical, however. For the inner and outer layers there are 16 wires per drift cell, while for the middle layer chambers there are 24 wires. The single wire resolution for the P-chamber wires has been measured to be roughly 200μm, and at large muon momentum this is what ultimately limits the precision of the momentum measurement [66]. Even so, at LEP I energies the sagitta error arising from multiple

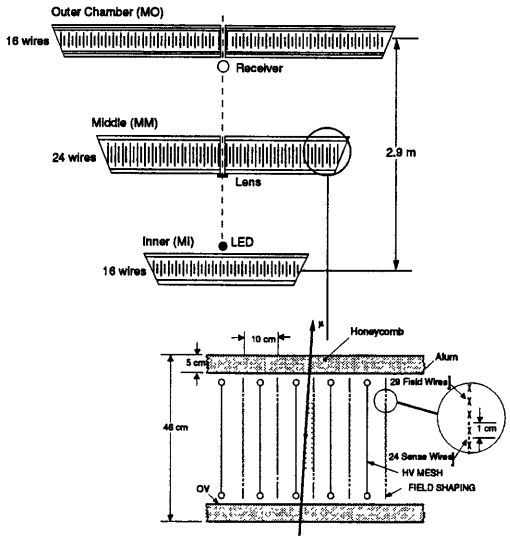

Figure 2-6: MUCH subdetector
A view of the chamber layers in an octant of L3's muon chamber system as well as a blow-up of a single layer as a muon passes through it.

scattering within the MUCH spectrometer (0.01 X_0 of scattering material) is non-negligible. Taking both of these factors into account, one can easily estimate the momentum resolution to be roughly 2%. Actually, there are several other minor sources which contribute to the sagitta error, as well, and experimentally one finds the resolution to be 2.7% for 45 GeV muons which traverse all three chamber layers (triplets, for $|cos(\theta)| \leq 0.7$). For muons which have hits in only the first two layers (doublets, for $0.7 \leq |cos(\theta)| \leq 0.83$) the resolution worsens to about 20%.

Immediately outside the MUCH and enclosing the entirety of the original L3 Experiment is a large solenoidal magnet which provides a 0.5 T field for bending charged tracks in the TEC and MUCH subdetectors. Like the MUCH, the magnet has an octagonal cross-section and has a diameter and length of about 12 m. It is comprised of some 28 packages, each containing 6 aluminum coils seprated by Mylar-covered fiber glass [66]. Surrounding the coils is a yoke made of soft iron. A large power supply provides the 30 kA of current to the aluminum coils to generate the magnetic field, and two gigantic doors at both ends of the experiment serve as pole pieces and allow access to the muon chambers during shutdowns or repair periods.

Finally, to complete the description of the L3 Experiment it should be mentioned that a forward-backward (FB) muon spectrometer was installed starting during the winter shutdown of 1994 and completed one year later. The new system is designed to improve the resolution of muons passing through the barrel MUCH doublet region and to extend muon coverage down to 24° from the beam line, both purposes being vital for the physics expected at LEP II. Joining the new FB system were two conventional 1.2 T toroidal magnets created by winding coils around both solenoidal magnet

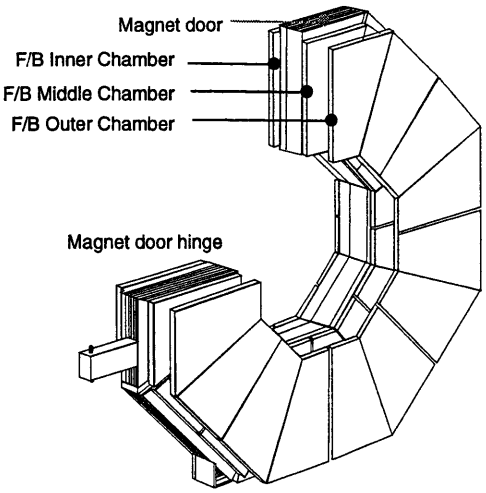

Figure 2-7: FB muon subdetector
A closeup perspective view of one end of the FB muon system.

doors. The entire FB system is made up of some 96 new drift chambers, 48 at either end of the experiment, and as with the MUCH subdetector, the chambers are arranged in octants with three layers [70]. Within each octant there are 3 chambers of the left-handed variety adjacent to 3 of the right-handed variety. The inner layer of chambers hangs off the inner side of the solenoid magnet doors and occupies the very narrow region between the doors and the ends of the MUCH barrel muon chambers. The middle and outer layer chambers, on the other hand, are rigidly fixed together in an aluminum frame and together form a package which hangs on the outside of the doors. In addition to the FB chambers themselves, development of a new triggering system was necessary to complete the FB subdetector. Triggering in the angular region covered by the FB chambers is being performed by a large resistive plate chamber system, and excellent results have been achieved. Thus far, performance of the FB chambers has, likewise, been excellent. Momentum resolution is about 5% at 44°, rising slowly to about 30% between $44° \leq \theta \leq 36°$, and remaining a constant 30% down to about 24°, where the resolution is limited by the multiple scattering in the 1 m thick iron magnet doors [70]. These numbers are in perfect accord with expectations.

2.2.5 Subdetector Reconstruction

Within the L3 framework offline event reconstruction is initially carried out at the subdetector level. In the TEC, for example, pattern recognition subroutines first identify hits likely to have been caused by the passage of the same charged particle. The drift times of these individual wire hits are then converted to coordinates in the r-ϕ plane using the known position vs. drift time relationship. Next,

a circle fit is applied to the points in order to reconstruct a track trajectory. If z-coordinate hits are available, a linear fit is applied in the s-z plane to obtain the polar angle (θ). The resulting reconstructed object is called a TTRK, and it is uniquely specified by its θ, p_t (obtained from the signed radius of curvature of the circle fit), distance of closest approach to the event vertex (DCA), and azimuthal angle (ϕ) at the point of closest approach. Additional information is also kept for each TTRK, including the number of hits along the trajectory, the wire numbers of the first and last hits, and the quality of the fits.

Reconstruction of tracks in the muon chambers is virtually identical to that in the TEC. First, a cell map is used to convert the recorded drift times which are associated to one another from the pattern recognition algorithms to positions in the P-chambers. Within each P-chamber, nearby hits are fit with a line (a reasonable approximation for high momentum tracks) to form P-segments, and then nearby segments in adjacent chamber layers are matched. For the Z-chambers the very same procedure is used except that Z-segments are produced from the hits found in both chambers in a given layer. Lastly, a circle is fit to the P-segments, a line is fit to the Z-segments, and matched P-segments and matched Z-segments in the same octant are matched together. The resulting object is called a MUTK, and like its TEC counterpart, it is uniquely described by its θ, p_t, DCA, and ϕ.

Performing reconstruction in the ECAL is ostensibly a simpler task than in the TEC or MUCH subdetectors because no fits are required. First, the pattern recognition identifies regions of energy deposition in the ECAL. If BGO crystals with energy depositions above some threshold are near enough to each other they are associated, but if not, no association takes place. Next, the energy of each crystal is determined by taking the measured ADC value, converting it to a voltage, subtracting the crystal pedestal value, applying a crystal temperature correction, applying xenon corrections, and multiplying by the experimentally determined crystal calibration constant. These reconstructed associated crystal groups are called EBMP's, and several useful quantities are calculated for each one. The most significant of these quantities is the energy of the bump, E_{best}. To determine this quantity one starts by calculating the energy contained in the 8 crystals surrounding the most energetic crystal in the bump (E_9) and applying a correction for the small amount of energy expected to lie outside this cluster of 9 crystals using knowledge of the electromagnetic shower shape in BGO. Slightly different corrections are applied to barrel and endcap EBMP's. Next, if E_{9-corr} is larger than 3 GeV then $E_{best} = E_{9-corr}$. Otherwise, E_{best} is based on E_6 to which empirical corrections for the shower shape and polar angle (when in the endcaps) have been applied [71]. E_{best} is L3's best estimate of the bump energy assuming the bump to have originated from an electron or photon. EBMP's also obviously have some angular position in the L3 reference frame which is determined by calculating the energy-weighted θ and ϕ using all the crystals in the EBMP. Another interesting quantity is E_9/E_{25}, where E_i is the sum of the energies in the (i-1) crystals surrounding the most energetic crystal in the EBMP. A high E_9/E_{25} signifies an isolated electromagnetic bump, while a low E_9/E_{25}

signifies either hadronic energy deposition or substantial nearby calorimetric activity (overlapping energy deposition). Another quantification of the quality of a bump is the electromagnetic chi-squared ($\chi^2_{\rm EM}$), which is a measure of the difference between the observed energy distribution among the EBMP crystals and what is expected from shower shape studies. In general, electromagnetic showers are more collimated, with roughly 93% of an electron's or photon's energy found in the nearest nine crystals, while hadronic showers are usually broader [71]. A low $\chi^2_{\rm EM}$ indicates that the EBMP is consistent with being an electromagnetic shower and vice versa. Finally, the value of a neural network variable ($F_{\rm net}$) based on all of these variables (and therefore correlated with them) is calculated for every EBMP. Values of $F_{\rm net}$ close to 1 imply that the EBMP is likely to have been generated from an electron or photon, and values close to 0 imply the opposite. This concludes the basic tutorial of ECAL reconstruction in L3.

Rounding out the discussion of calorimetry, one comes to the reconstruction of HCAL objects, which is similar to that of ECAL objects. Here again, pattern recognition schemes combine nearby (in both z and ϕ projections) HCAL tower hits into entities known as HCAL geometric clusters (HGCL's). Using information from these hits, the energy, polar angle, and azimuthal angle of the HGCL are determined. Calculation of the angles is rather straightforward as before, while the energy calculation is slightly more complicated, involving various conversion constants and calibration procedures. Other than these, few other quantites are retained for the HGCL's.

2.2.6 AXL3 Reconstruction

Once the reconstruction has been performed for the various L3 subdetectors individually, higher level objects are generated by utilizing information from all across L3 (AXL3). Some of these include ATRK's (tracks), AMUI's (muons), ASRC's (smallest resolvable clusters), and ASJT's (jets). In general AXL3 objects are improved versions of those identified and reconstructed by the individual subdetectors. Track θ-coordinate information, for example, is improved from the TTRK level to the ATRK level by matching TTRK's to EBMP's at the BGO inner surface. Because the angular resolution of the BGO is so good, the matching can usually be performed reliably, and adding the EBMP polar angle information to that given by the TEC Z-chambers yields substantial improvement in the evaluation of a track's polar angle. For muons, AMUI's are improved versions of MUTK's obtained by backtracking the MUTK's through the inner calorimeters and matching them to TTRK's. Superior estimates in the θ and particularly in the ϕ at the IP are made when a TTRK is matched than when simply extrapolating the MUTK track back to the origin because muons can be multiply scattered appreciably in traversing the inner subdetectors (especially at low energies). Further benefits of the MUTK backtracking process are that the radial distance of closest approach (RDCA) and z-coordinate at the point of closest approach (Z0) can be determined, the ionization loss in the inner calorimeters can be estimated (and added to the MUTK momentum to obtain the

muon's momentum at its creation), and the MUTK can be matched to the muon's ionization clusters in the ECAL and HCAL (if any). All this information is stored in the AMUI structure. ASRC objects are obtained through angular matching of HGCL's and EBMP's at the BGO inner surface. Not all ASRC's need contain both an HGCL and EBMP, however. Isolated objects of either type will become ASRC's during the process of AXL3 reconstruction but will not, of course, include any of the type of information associated with the absent cluster. Lastly, ASJT's are mentioned here for completeness. These AXL3 objects are formed by combining nearby ATRK's, ASRC's, and AMUI's into an abstract jet object called an ASJT. The primary information associated with each ASJT are the energy, θ, and ϕ, all of which are calculated in an obvious way from the constituents. A handful of additional minor AXL3 objects are also reconstructed for each event, but for many analyses the ATRK's, AMUI's, ASRC's, and ASJT's provide sufficient information.

2.2.7 Particle Signatures

So far the L3 detector components have been described in some detail as has been the offline event reconstruction. In order to perform a particular analysis at L3, however, it is clear that one must also be familiar with the signatures that particles produce in the detector. The relevant particles for the analysis on which this thesis is based include photons, electrons, and muons. L3, of course, is capable of identifying a wide variety of other particles like pions, kaons, and lambdas, but the details pertaining to these will not be described here.

The electromagnetic particles, electrons and photons, are fairly easy to identify at L3. These particles produce electromagnetic showers in the ECAL and very little in the HCAL. For electrons, one also observes a track in the TEC which points to the shower. To select photons, then, one might require ASRC's with a high E_9/E_{25}, a low χ^2_{EM} and/or a high F_{net}, an E_{best} above some energy threshold, and isolation from tracks (especially in the r-ϕ plane). To select electrons one would ask for similar shower properties as well as an ATRK which, when extrapolated to the BGO inner surface, matches the azimuthal position of the ASRC. In addition, one might also demand good p_t matching between the ATRK and ASRC. It should be mentioned that often electrons and photons are found buried in jets, and in these cases the signatures will not be totally clear due to overlapping energy deposition from multiple particles. Depending on the needs of a given analysis, the cuts outlined here should be tightened or loosened. The particular cuts used in this analysis will be described in subsequent chapters.

For muons the signature in L3 is quite distinctive. Starting from the IP, one sees a track in the TEC pointing to a minimum ionizing particle (MIP) signature in the calorimeters (a 280 MeV ASRC in the ECAL and a track-like ASRC with roughly 1.8 GeV energy in the HCAL). After this, one will have a MUTK in the muon chambers to which (hopefully) all the previous objects are linked in the AMUI description. Still, as with electrons and photons, if the muon happens to be in a jet, its MIP

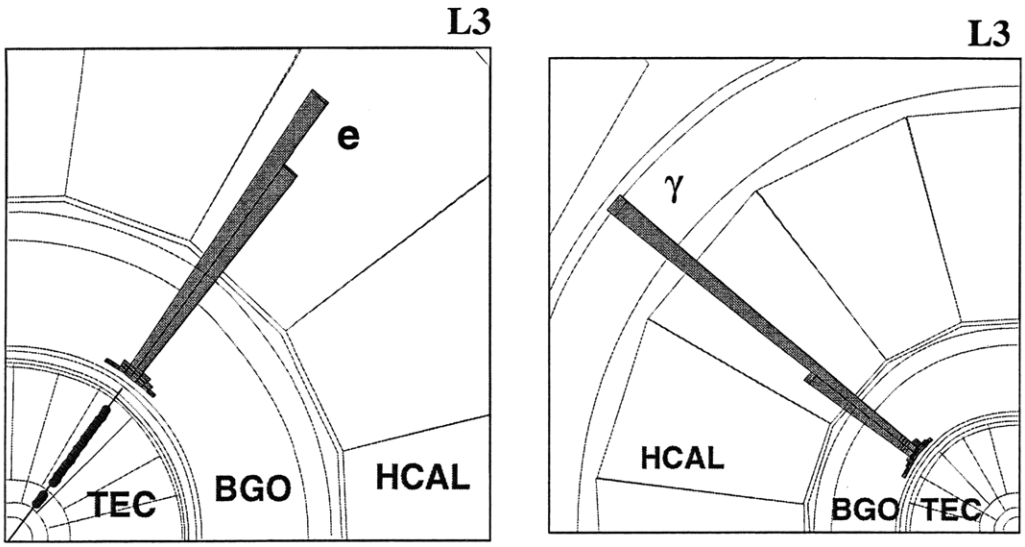

Figure 2-8: Electromagnetic particle signatures
The electromagnetic signatures of an isolated electron and an isolated photon.

signature might not be so clean, and one will basically see only a track in the muon chambers maybe with a scintillator hit and/or a matched TTRK. Unfortunately, the mere existence of an AMUI does not necessarily indicate the presence of an interesting physics muon, especially in hadronic events. Essentially the impurity comes from two different sources: hadronic punchthrough and real cosmic ray muons. Hadronic punchthrough is the name given to hadronic showers which penetrate through the HCAL and muon filter into the muon chambers. Typically, such fake muons are reconstructed poorly so that cuts on the RDCA and Z0 will provide adequate rejection. Such cuts will also help to reduce the cosmic ray muon contamination as will cuts on scintillator timing (when valid scintillator hits are present). The selection of muons for this analysis is based on these various considerations and like that of electrons and photons will be covered in more detail in the next few chapters.

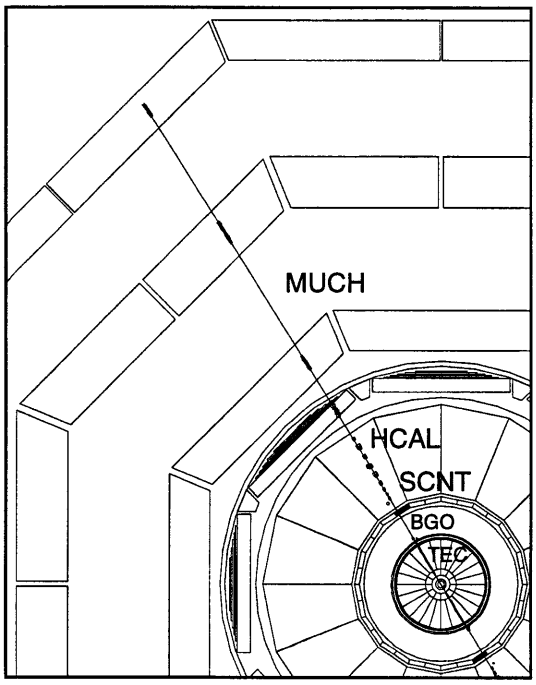

Figure 2-9: Muon signature
The passage of an isolated muon through the L3 detector.

Chapter 3

Preparatory Investigations

3.1 Heavy Quarkonium Selection

$c\bar{c}$ and $b\bar{b}$ bound states are heavier than other mesons because they are comprised of two heavy quarks. Like other heavy mesons, D's and B's for example, many decay modes are possible, most of which have small branching ratios and involve hadronic final states [49]. Since heavy quarkonium production in the decays of Z's is rare, attempting to extract a signal using the hadronic decays would be very difficult experimentally. Background from other more probable processes in Z decays is prohibitively large, drowning out the signal. Fortunately, unlike other heavy mesons, the 1^3S_1 and 2^3S_1 charmonium states which are relevant to this thesis also decay electromagnetically into pairs of oppositely charged leptons. Moreover, the branching ratios for these leptonic modes are relatively large - at the several percent level - due to OZI suppression of the strong decay modes involving multiple hard gluons as well as the fact that the quarkonium states lie below the $D\bar{D}$ threshold. In addition, the signature of two oppositely charged, same generation leptons in the final state is rather unique. The only relevant background to such a signal involves leptons from semi-leptonic weak decays of heavy quarks and/or misidentified leptons, but this background is not overwhelming. It is this confluence of factors which allows for the experimental observation of heavy quarkonium states at the Z peak.

For completeness, it should be noted that the J can only decay to e^+e^- and $\mu^+\mu^-$. Tau pair decays are obviously kinematically forbidden since $m_J = 3.097$ GeV and $2m_\tau = 3.554$ GeV. For the ψ' the $\tau^+\tau^-$ decay mode is highly phase space suppressed because $m_{\psi'} = 3.686$ GeV. In the case of the upsilon systems, tau pairs are produced at nearly the same levels as electron and muon pairs. However, since taus decay further into final states with undetectable neutrinos, they are not useful. Therefore, it is to be understood that only the e^+e^- and $\mu^+\mu^-$ modes were considered in this analysis.

3.2 Purpose of Lepton Study

Having established the decay modes to be searched for, it was deemed necessary to study the properties and behavior of leptons in the L3 detector. To a large extent this information was known at a superficial level beforehand, but the goal of the study was to acquire this knowledge experimentally and describe it more precisely. The study was performed with real data, thereby allowing for slight differences with Monte Carlo simulated data which could later be checked. One clear requirement for the study was that the final lepton samples be pure so that the properties of any irreducible hadronic background or cosmic ray muons would not disturb what would eventually be interpreted as the properties of leptons originating at the interaction point. The logical event type to study was $Z \rightarrow \tau^+\tau^-$ in which only one τ decays to an e or μ. A sample of muons from such events can be extremely pure since the event topology is unique. Cosmic ray muons can be eliminated with timing cuts on the associated scintillator hits, and the pion and kaon punchthrough in the muon chambers is at a much lower level relative to the true muon tracks owing to the high absorption of the ECAL and HCAL. The electron sample, on the other hand, cannot be made so pure since the L3 detector uses the same subdetectors to measure electrons and hadrons and does not naturally suppress the hadrons relative to the electrons in 1-prong tau decays. To increase the purity of the electron sample, one is obliged to cut on shower shape variables, but even this does not totally eliminate the pion and kaon background. Unfortunately, the particle identification through the ionization loss in the TEC gas is too limited to be of use in hadron rejection. Several aspects of the tau events made them ideal for studying leptons:

- Event type is common, providing a large and statistically relevant sample of leptons ($Br(Z \rightarrow \tau^+\tau^-) = 3.36\%$, $Br(\tau \rightarrow e\bar{\nu}_e\nu_\tau) = 17.80\%$, $Br(\tau \rightarrow \mu\bar{\nu}_\mu\nu_\tau) = 17.30\%$) [49].
- Events have easily identifiable topology, providing a pure sample, especially for muons.
- Selection is possible without cuts on muon variables and with limited cuts on electron variables, eliminating any potential bias of lepton properties.
- Final sample contains leptons with energies over full range from 0 GeV to 45 GeV.

There was, unfortunately, one obvious drawback to using the tau events with a single 1-prong decay for studying leptons to improve quarkonium selection. The leptons in the tau events are quite isolated, which typically is not the case for the leptons arising from quarkonium decays. It is conceivable that the description of the lepton quantities that were studied is different for isolated leptons and for leptons in jets (like the signal), but this was a necessary tradeoff for the desired lepton sample purity.

Cut	Motivation
NASRC ≤ 12	remove $q\bar{q}$ events
$2 \leq$ NATRK ≤ 4	remove $q\bar{q}$ events
$EBGO_{lumi} \leq 10$ GeV	remove 2γ events
$EBGO_{cap} \leq 35$ GeV	remove 2γ events
missing $\lvert E_{\parallel}\rvert/E_{vis} \leq 0.5$	remove 2γ events
$E_{BGO+HCAL} \geq 15$ GeV	remove dimuon and 2γ events
$E_{BGO} \leq 65$ GeV	remove bhabha events
NAMUI $= 1$	remove dimuon events
NPSEG ≥ 2	insure muon quality
NZSEG ≥ 1	insure muon quality
$T_{near} \leq 5$ ns	remove cosmics
$\theta_{isolation} \geq 90°$	require proper τ topology

Table 3.1: Preparatory investigation muon selection
Selection criteria used to identify muons in $\tau^+\tau^-$events in which only one tau decayed to a muon.

3.3 Muon Study and Results

The objectives for the muon study were the following:

1. determine the behavior of $RDCA_\mu$ vs. muon momentum
2. determine the behavior of $Z0_\mu$ vs. muon momentum
3. determine the relative muon detection efficiency (ϵ) (low muon momentum relative to high muon momentum)
4. compare the data and Monte Carlo descriptions of $RDCA_\mu$, $Z0_\mu$, and ϵ

The motivation for studying the muon RDCA and Z0 (see the section on AXL3 reconstruction in Chapter 2) as a function of the muon momentum was that they are influenced by multiple scattering, which varies inversely with particle momentum. The purpose of studying the muon detection efficiency at low momentum was to obtain a sense of how low in momentum one might hope to detect muons using the muon chambers. Ionization losses in the inner subdetectors amount to approximately 2.5 GeV, so one will detect few muons in the muon chambers which have a momentum below this value at their point of creation near the interaction point. However, the exact location and shape of this threshold was not known before the study. Most important of all was that the comparison of these data quantities with those from Monte Carlo could be used to judge the quality of the simulation. To achieve the muon study objectives, 1-prong tau events were used as described in the previous section. The complete selection for the muon sample is given in Table 3.1 together with the motivation for each cut. Applying this selection to L3's 1991-1995 data set, some 18,809 muon candidates were found. The muons were divided into 6 momentum ranges (2 GeV – 5 GeV, 5 GeV – 8 GeV, 8 GeV – 15 GeV, 15 GeV – 22 GeV, 22 GeV – 30 GeV, and 30 GeV – 40 GeV),

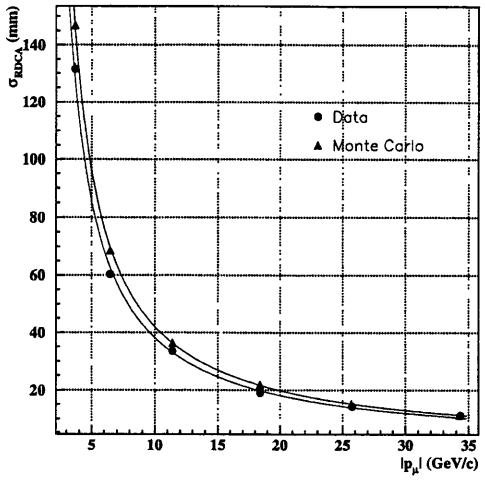

Figure 3-1: Muon σ_{RDCA} vs. muon momentum
The data have been fit with functions of the form: $a/(|p_\mu| - b)$. With the units specified above, the fit to the data yielded $a = 343.8, b = 0.99$. For Monte Carlo simulated data, the fit gave $a = 372.8, b = 1.13$.

and the RDCA_μ and $\mathrm{Z0}_\mu$ were histogrammed for the muons in each range. A gaussian fit was applied to each distribution and the width taken as a measure of the typical RDCA_μ or $\mathrm{Z0}_\mu$ at a given momentum (the average muon momentum of all the muons in a given range). The behavior of σ_{RDCA} and σ_{Z0} for real, isolated muons as a function of momentum is shown in Figure 3-1 and Figure 3-2. As expected, the σ_{RDCA} and σ_{Z0} increase in size at lower muon momentum, revealing the influence of multiple scattering. The same procedure was applied to a sample of 350,000 Monte Carlo $\mathrm{Z} \rightarrow \tau^+\tau^-$ events, and the results are again plotted in Figure 3-1 and Figure 3-2. Reasonably good agreement is observed.

The approach that was adopted for measuring the muon detection efficiency was to try to obtain the momentum spectrum of muons originating solely from tau decays and compare it to the generator level spectrum as determined by Monte Carlo tau events. In order to do this, the first step was to generate a spectrum which would approximate the data spectrum by using different types of Monte Carlo events. Contributions were taken from $\tau^+\tau^-$ events (dominant), $\mu^+\mu^-$ events (high momentum contamination), and 2-photon events with muons in the final state (low momentum contamination), all weighted by their production cross-sections [72]. By taking the momentum spectrum of the selected muons from the tau Monte Carlo events and dividing it by the spectrum from the full sample, the sample purity was estimated as a function of muon momentum (see Figure 3-3). Here, purity is defined as the fraction of the selected muons whose parents were taus. Multiplying the purity function (derived from Monte Carlo) by the data momentum spectrum yielded the corrected

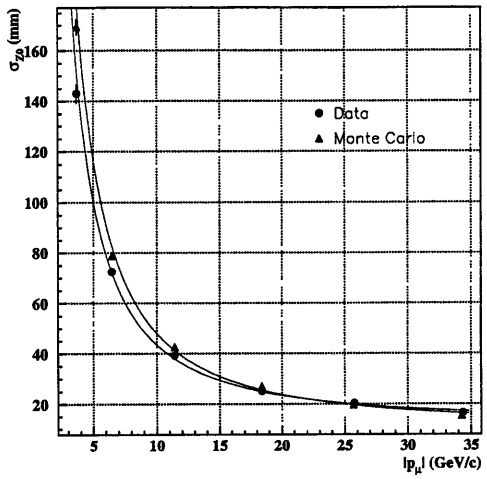

Figure 3-2: Muon σ_{Z0} vs. muon momentum
The data have been fit with functions of the form: $a/|p_\mu|^{1.5} + b$. With the units specified above, the fit to the data yielded $a = 980.2, b = 12.47$. For Monte Carlo simulated data, the fit gave $a = 1185.9, b = 10.5$.

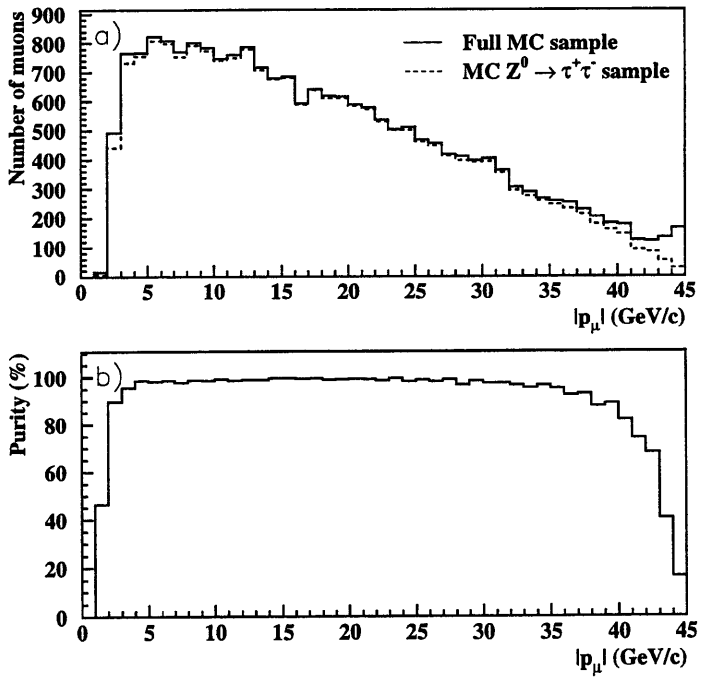

Figure 3-3: Muon study Monte Carlo muon spectra and sample purity vs. momentum
a) muon momentum spectra for muons from the full Monte Carlo sample and from the $Z \rightarrow \tau^+\tau^-$ sample and b) the muon sample purity vs. muon momentum as determined by Monte Carlo.

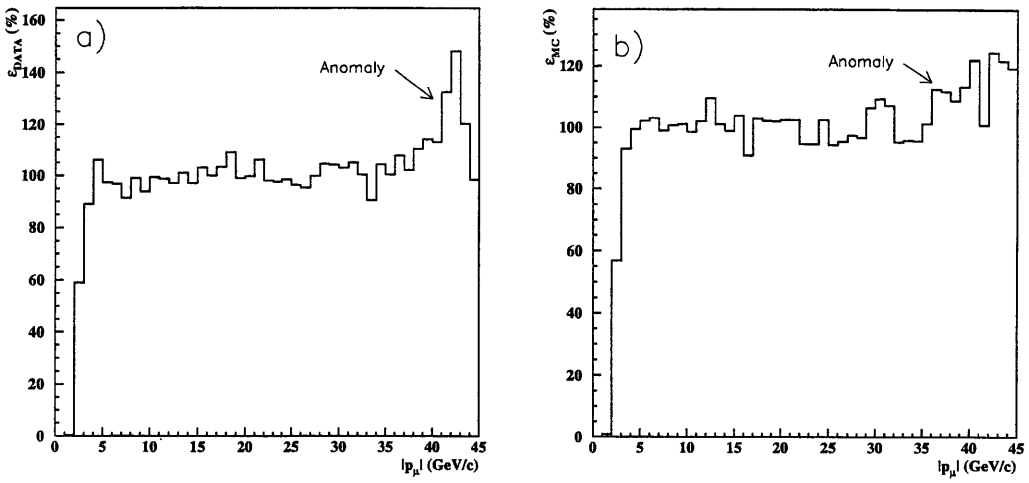

Figure 3-4: Relative muon detection efficiency vs. muon momentum
a) data and b) Monte Carlo. The errors on each bin range between 4% at low momentum and 10% at high momentum. The anomalies at high momentum are likely due to low statistics and in the case of the data also to an excess of muons from dimuon events which are not entirely accounted for by the purity correction.

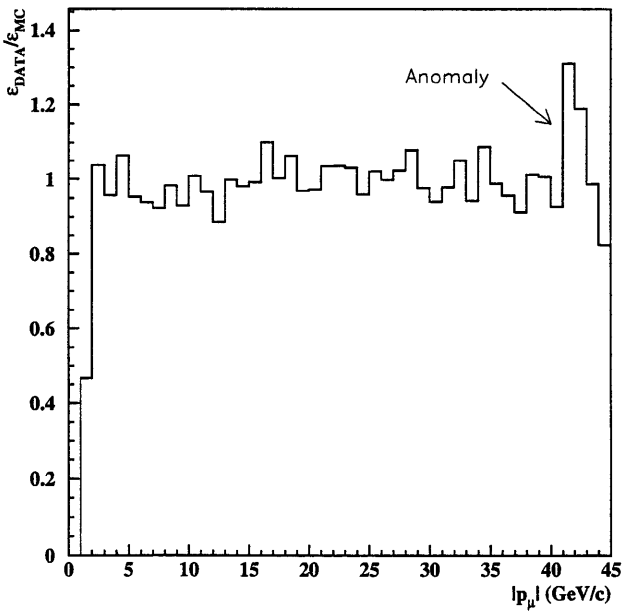

Figure 3-5: Comparison of relative muon chamber efficiencies for data and Monte Carlo
The anomaly at high momentum is due to an excess of muons from dimuon events in the data sample.

data muon spectrum for muons originating from tau decays. Next, the Monte Carlo generator level spectrum for tau events was normalized to the purity-corrected data spectrum in the range between 10 GeV and 35 GeV (where there was virtually no background contamination before correction), and the latter was divided by the former to obtain the relative muon chamber detection efficiency as a function of momentum (see Figure 3-4). From Figure 3-4, it can be seen that $\epsilon_{\rm DATA}$ is significant all the way down to $p_\mu = 2$ GeV and is nearly 100% above 3 GeV. The $\epsilon_{\rm MC}$ was measured by dividing the muon momentum spectrum of selected muons in Monte Carlo tau events by the renormalized generator level spectrum from those same events. Lastly, Figure 3-5 shows $\epsilon_{\rm DATA}/\epsilon_{\rm MC}$, which gives one a sense of how good the Monte Carlo simulation describes the muons in real data. In a word, the description is excellent all the way down to the smallest detectable muon momenta.

3.4 Electron Study and Results

The single goal of the electron study was to determine the behavior of the TEC-ECAL ϕ angle matching vs. E_{best} of the electron. This study, therefore, was clearly not as ambitious as the muon study, and this was so for several reasons. First, the primary selection variables for electrons (Σ_9/Σ_{25} and $\chi^2_{\rm EM}$) were already understood fairly well beforehand, obviating the need for further work. Second, as mentioned previously, cuts on these variables was already necessary to identify electron candidates, and a method for studying electrons using data but without explicit cuts on Σ_9/Σ_{25} and $\chi^2_{\rm EM}$ was never conceived.

Because use of the electron energy spectrum from 1-prong tau decays was not actually needed (as in the muon case), it was considered acceptable to allow electron candidates into the final sample using event types other than $\tau^+\tau^-$events. Therefore, the selection devised admits a large number of candidates from bhabha events which populate the upper end of the energy spectrum and various 2-photon events which populate the low end. The latter is perhaps more worrisome since this source likely contains a fair amount of pions and kaons as well as electrons, but no clear, effective, method was ever concocted whereby this hadronic background could be efficiently rejected without removing a large fraction of the true electrons and potentially biasing the electron quantities in the process. Keeping this in mind, the full selection is given in Table 3.2. Applying the electron selection to L3's 1991-1995 data set, a sample of 83,845 electron candidates was obtained. To ascertain the functional behavior of $\sigma_{\Delta\phi}$ versus E_{best}, where $\Delta\phi = |\phi_{\rm ASRC} - \phi_{\rm ATRK}|$ and $\phi_{\rm ATRK}$ is the azimuthal angle at the surface of the ECAL of the electron track associated with the ASRC , six ranges of E_{best} were considered. For every electron candidate, the observed $\Delta\phi$ was histogrammed according to its observed energy. Each of the six histograms was then fit with a gaussian as before and the width taken as a measure of the typical $\Delta\phi$ at a given E_{best}. The behavior of $\sigma_{\Delta\phi}$ is displayed in Figure 3-6. The data $\sigma_{\Delta\phi}$ plot was fit with a function of the form $\sigma_{\Delta\phi} = a/E_{best} + b$, and a and b

Cut	Motivation
$1 \leq$ NASRC ≤ 12	remove $q\bar{q}$ events
$2 \leq$ NATRK ≤ 4	remove $q\bar{q}$ events
NAMUI ≤ 1	remove dimuon events
ASRC $E_{best} \geq 1$ GeV	insure electron quality
ASRC $\Sigma_9/\Sigma_{25} \geq 0.9$	insure electron quality
ASRC $\chi^2_{EM} \leq 8$	insure electron quality
ASRC $E_{HCAL}/E_{total} \leq 0.01$	insure electron quality
$\theta_{isolation} \geq 90°$	insure electron quality
ATRK matched to ASRC	insure electron and not γ

Table 3.2: Preparatory investigation electron selection
Selection criteria used to identify electron candidates in $\tau^+\tau^-$, bhabha, and 2γ events.

were found to be $a = 6.336$ GeV mrad and $b = 1.372$ mrad. For the Monte Carlo simulated data, a different functional form was necessary to adequately describe the results. To be precise, the Monte Carlo $\sigma_{\Delta\phi}$ plot was fit with a function of the form $\sqrt{a/E_{best} + b}$, where a and b were measured to be $a = 22.48$ GeVmrad^2 and $b = 0.41$mrad^2. The reason for the difference in the functional forms was never elucidated, but the discrepancy is not terribly critical. Even the observable *numerical* disagreement between data and Monte Carlo seen in Figure 3-6 is not too important since the cuts made on $\Delta\phi$ for the analysis (as will be seen in the next chapter) were quite loose according to the $\Delta\phi$ standards set by the data. In short, the agreement, while not perfect, was satisfactory.

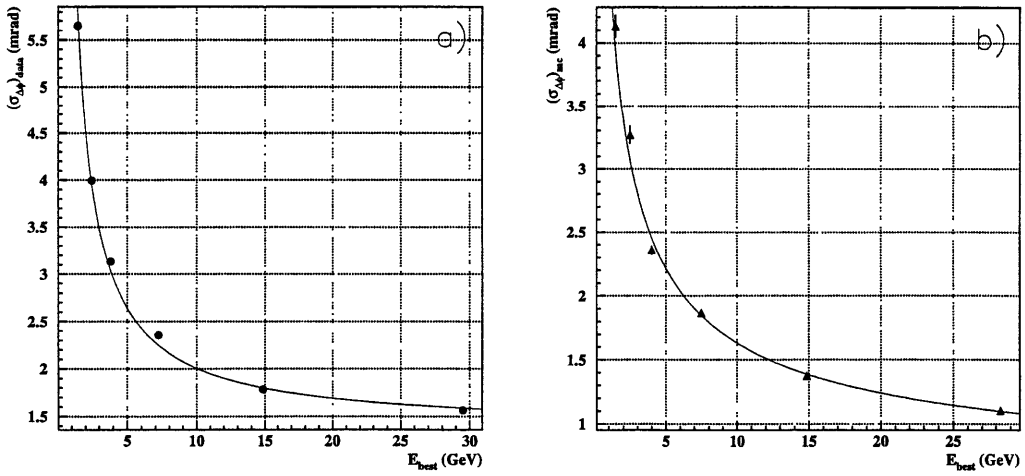

Figure 3-6: TEC-ECAL angular matching vs. E_{best}
Electron $\sigma_{\Delta\phi}$ vs. E_{best} for a) data and b) Monte Carlo.

Chapter 4

J and ψ' Production

4.1 Hadronic Pre-selection

The very first step in the search for heavy vector mesons was to identify and eliminate from further consideration bad L3 data-taking runs. A list of such runs was compiled from the master list of known L3 bad runs using standard L3 procedures. The list that was finally generated actually constituted a particular subset of all L3 bad runs since only bad runs during which there were severe problems with the data acquisition(DAQ) or the ECAL or MUCH subdetectors were placed on the bad run list for this analysis. L3 bad runs which were considered bad because of problems with various triggers or other subdetectors did not go into the bad run list, and consequently, events from such runs were passed through the remainder of the analysis chain. The reasoning behind this particular definition of a bad run (bad DAQ or bad ECAL or bad MUCH) and the handling of less severe time-dependent detector inefficiencies will be explained later in the section on the efficiency determinations.

Once bad runs were skipped, each remaining event in the L3 1991-1995 (inclusive) data set was subjected to a hadronic pre-selection since heavy vector mesons are found only in hadronic decays of the Z. This pre-selection relies on several distinguishing properties of $q\bar{q}$ events, namely high cluster and track multiplicity and large and well balanced visible energy. The exact cuts that were imposed are shown below:

- $N_{ASRC} > 13$
- $N_{ATRK} > 4$
- $0.5 < E_{vis} < 2.0$
- $E_{HCAL} > 2.5$ GeV
- $E_{\perp}/E_{vis} < 0.5$

Year	# of Hadronic Events
1991	284917
1992	606551
1993	664416
1994	1476437
1995	590275
TOTAL	3622596

Table 4.1: Numbers of hadronic events
Number of hadronic events selected for each year.

- $|E_{||}|/E_{vis} < 0.6$

This is a standard hadronic event selection, and according to previous studies as well as an independent one performed for this analysis, it has an efficiency of 99.0% and a purity ($\pi_{q\bar{q}}$) of (0.9975 ± 0.0005). About half of the tiny impurity comes from $\tau^+\tau^-$ events, and the remainder comes from cosmics, beam gas interactions, and 2-photon events. [73] The numbers of hadronic events found in each year are shown in Table 4.1.

4.2 J and ψ' Selection

Each event passing the hadronic pre-selection was then examined further for evidence of a J or ψ' dilepton decay. In general, the signature of this process is one high energy lepton and one low energy lepton located near each other in physical space ($\bar{\theta}_{open} = 27°$). This can be seen from the MC momentum and opening angle distributions shown in Figure 4-1. For the dimuon channel, charmonium candidates were identified by the presence of two reconstructed AMUI objects with an opening angle less than 90°. In addition to minimum momentum requirements, loose cuts on the RDCA and Z0 of each AMUI were applied to reduce hadronic punchthrough and cosmic ray background. The complete J$\rightarrow \mu^+\mu^-$ selection is given below, where the subscripts 1 and 2 denote the most and least energetic muons, respectively:

- $|p_{\mu-2}| > 2.0$ GeV
- $|p_{\mu-1}| + |p_{\mu-2}| > 8.0$ GeV
- $RDCA_1 < 3\sigma_{RDCA}$ and $RDCA_2 < 3\sigma_{RDCA}$
- $|Z0_1| < 5\sigma_{Z0}$ and $|Z0_2| < 3\sigma_{Z0}$
- $NPSEG_1 \geq 2$ and $NPSEG_2 \geq 2$
- $NZSEG_1 \geq 1$ and $NZSEG_2 \geq 1$

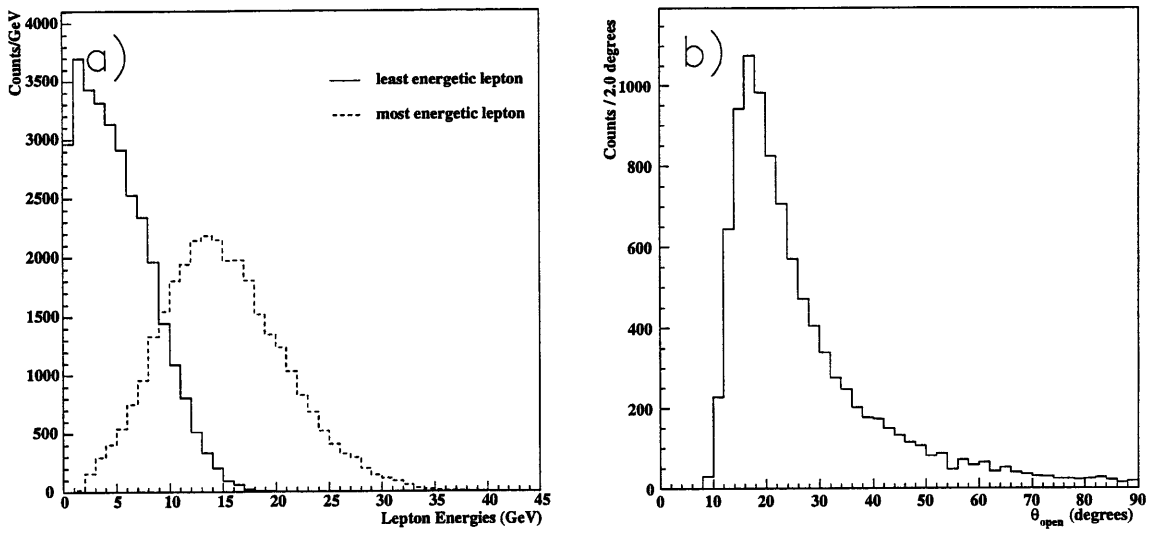

Figure 4-1: Monte Carlo b→J+X→ l^+l^- + X event variables
a) laboratory frame lepton momentum spectra and b) laboratory frame dilepton opening angle distribution.

- $\theta_{\rm open} < 90°$

For the dielectron channel, all combinations of two ASRC's lying within 90° were considered separately as a potential J or ψ' candidate. As with the muons, minimum energies were required for the electrons. Additional cuts were then applied to guarantee the isolation of each ASRC and increase the probability that both ASRC's were electromagnetic in nature (as opposed to hadronic). Lastly, each ASRC was required to be associated to an ATRK, with good ϕ (azimuthal angle) and $E_t(p_t)$ matching. The complete selection is specified below:

- $E_{best-2} > 1.5$ GeV
- $E_{best-1} + E_{best-2} > 8.0$ GeV
- $(\Sigma_9/\Sigma_{25})_1 \geq 0.8$ and $(\Sigma_9/\Sigma_{25})_2 \geq 0.8$
- $(\chi^2_{\rm EM})_1 \leq 12$ and $(\chi^2_{\rm EM})_2 \leq 12$
- $(\Delta\phi_{\rm ASRC-ATRK})_1 < 3\sigma_{\Delta\phi}$ and $(\Delta\phi_{\rm ASRC-ATRK})_2 < 3\sigma_{\Delta\phi}$
- $R_1 = (|1/E_t - 1/p_t|)_1 < 3\sigma_R$ and $R_2 = (|1/E_t - 1/p_t|)_2 < 3\sigma_R$
- $\theta_{\rm open} < 90°$

It is worth noting that no opposite charge requirement was made for the leptons in either channel. As expected, this did not increase the number of J mesons selected. However, it did slightly enhance the background in the region of the J peak, facilitating the fitting of the invariant mass distribution.

4.3 Efficiency Determination

In order to estimate the efficiency of this selection, samples of 11000 events of the type $Z \rightarrow b\bar{b} \rightarrow (J + X) \rightarrow (e^+e^- + X)$ and 11000 events of the type $Z \rightarrow b\bar{b} \rightarrow (J + X) \rightarrow (\mu^+\mu^- + X)$ were generated with the Jetset 7.4 Monte Carlo. In addition, 5000 Monte Carlo events of the type $Z \rightarrow b\bar{b} \rightarrow (\psi' + X) \rightarrow (e^+e^- + X)$ and 5000 events of the type $Z \rightarrow b\bar{b} \rightarrow (\psi' + X) \rightarrow (\mu^+\mu^- + X)$ were also produced for the present analysis to determine the efficiencies for detecting ψ' particles. It is worth noting that the L3 simulation accounts for such physical processes as bremsstrahlung and ionization losses in various parts of the detector and uses a fairly accurate model of the L3 geometry. By applying the selection described in the previous section to the ideal Monte Carlo signal event samples, one can obtain a zeroth-order approximation of the selection efficiencies for each decay mode. For $J \rightarrow e^+e^-$this zeroth-order result is $\epsilon_{J \rightarrow e^+e^-} = 30.5\%$, and for $J \rightarrow \mu^+\mu^-$it is $\epsilon_{J \rightarrow \mu^+\mu^-} = 34.5\%$. The corresponding selection efficiencies for ψ' are $\epsilon_{\psi' \rightarrow e^+e^-} = 37.1\%$ and $\epsilon_{\psi' \rightarrow \mu^+\mu^-} = 36.4\%$. It is essential to keep in mind, however, that differences between real data and these ideal Monte Carlo events do exist due to slight imperfections in the Monte Carlo model of L3 and to time-dependent sub-detector inefficiencies. Therefore, these numbers must be corrected to obtain the real efficiency estimates.

Improved efficiency determinations were made by taking into account the major differences between ideal Monte Carlo events and real data events. The method by which this was accomplished was to study bhabha and dimuon events to generate correction maps of the L3 detector for each J dilepton decay mode. For this purpose the L3 detector solid angle coverage was conceptually divided into 1152 regions of 7.5° by 7.5°. Next, $Z \rightarrow e^+e^-$and $Z \rightarrow \mu^+\mu^-$events were selected by triggering on one high energy lepton. Other types of events, specifically cosmics and $Z \rightarrow \tau^+\tau^-$events, were rejected by applying timing and global event energy cuts. Once an event was selected, a search was made for the partner lepton opposite to the trigger lepton. If one was found, two array elements were incremented based on the (θ, ϕ) coordinates of the partner lepton - one in the number expected array $N_{exp}(\theta, \phi)$ and one in the number found array $N_{fnd}(\theta, \phi)$. Otherwise, only an element of $N_{exp}(\theta, \phi)$ was incremented according to the (θ, ϕ) opposite the trigger lepton. By dividing the elements of $N_{fnd}(\theta, \phi)$ by those of $N_{exp}(\theta, \phi)$, (θ, ϕ)-dependent pseudo-efficiencies were determined. The term pseudo-efficiency is used here instead of efficiency because the full inefficiency due to physical gaps and other insensitive areas of the detector cannot actually be measured with this method when these regions happen to be correlated back to back. For example, finite gaps exist at the octant boundaries in the MUCH subdetector which happen to line up for back to back muons. Thus, when one stiff muon in such an event flies through one of these gaps and is not measured, it frequently occurs that the partner muon will pass through the correlated gap on the other side of the detector. Clearly, there is an inefficiency, but it will not be measured by this method because neither muon is available to trigger the event. Such inefficiencies are irrelevant, however, because the pseudo-efficiency

	e^+e^-		$\mu^+\mu^-$	
	J	ψ'	J	ψ'
ϵ_{ideal}	30.5%	37.1%	34.5%	36.4%
ϵ_{real}	24.7%	29.6%	31.3%	33.1%

Table 4.2: Selection efficiencies
Ideal and real selection efficiencies for J and ψ' decays to dileptons.

maps are used to reweight individual leptons in the Monte Carlo signal events which are actually reconstructed in the detector, and in the active regions of L3 the pseudo-efficiency should be a good approximation for the true efficiency. With the pseudo-efficiency maps for both data and Monte Carlo in hand, the signal event samples were again analyzed, now applying a correction factor or weight for each lepton equal to the observed ratio of the data and Monte Carlo pseudo-efficiencies at the lepton's (θ, ϕ) coordinates. To obtain a sense of the measured pseudo-efficiency maps, one can examine the theta projections of the maps for both electrons and muons shown in Figure 4-2. Also, it is worth mentioning that the statistical error on individual entries in the pseudo-efficiency data maps were on the order of 7% to 8%, while those for the MC maps were somewhat lower due to increased statistics. Averaging over time and angles, J decay correction factors of (0.81 ± 0.01) for dielectron decays and (0.91 ± 0.01) for dimuon decays were measured, where the errors are purely statistical. For ψ' the values (0.80 ± 0.01) and (0.91 ± 0.01) were found. The selection efficiency determinations are summarized in Table 4.2. Since this method relies on high energy trigger electrons and muons, both the ECAL and MUCH subdetectors as well as the DAQ were required to be fully operational. All other inefficiencies, however, were actually measured by the pseudo-efficiency map for the data, which explains the limited bad run list used for this analysis.

Because the efficiency correction procedure is so critical to the branching ratio measurements, further details will be supplied regarding this particular step of the analysis. First, in order for this correction to be made properly, it was essential that the same lepton selection be used for the partner leptons in the efficiency study as for the leptons in the J analysis. Furthermore, it was imperative that the $Z \rightarrow e^+e^-$and $Z \rightarrow \mu^+\mu^-$selections not only have high efficiency but also yield samples of very high purity. Otherwise, impure samples would necessarily lead to an apparent lower efficiency for the data than for the pure ideal Monte Carlo bhabha and dimuon events and hence to incorrect correction factors. Finally, it was important that the same bad runs be excluded from the J analysis and the detector efficiency study. The need for such consistency is obvious; measured detector inefficiencies were required only for those runs which were actually analyzed for heavy vector mesons. All of these subtleties were taken into account during the evaluation of the correction factors.

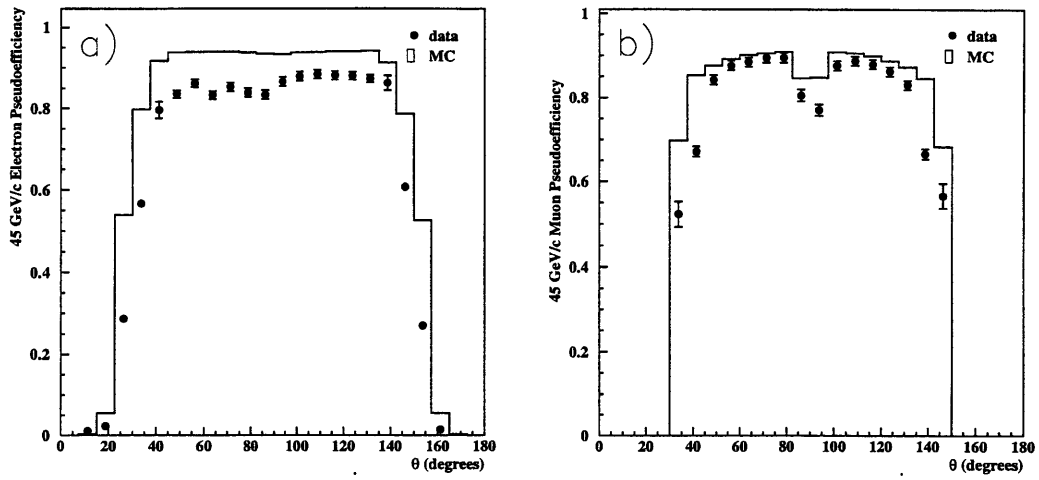

Figure 4-2: Pseudo-efficiency map polar angle projections
a) electron pseudo-efficiency vs. θ for data and Monte Carlo and b) muon pseudo-efficiency vs. θ for data and Monte Carlo.

4.4 Data Analysis

After applying the selection to the full 1991-1995 (inclusive) L3 data set the invariant mass distributions shown in Figure 4-3 and Figure 4-4 were obtained. In these plots one sees a decreasing background of candidates from $b \to \ell$, $c \to \ell$, and $b \to c \to \ell$ decays as well as misidentified leptons with clear J peaks near 3.097 GeV and much smaller excesses near the ψ' mass. The numbers of J's and ψ''s were derived from these distributions in two different ways with the results being averaged and one half the difference taken as a systematic error. For both methods it was necessary to somehow take into account the expected signal shapes of the vector mesons being studied, which are distinctly non-gaussian. For example, the J lineshapes for both the dielectron and dimuon decay channels are shown in Figure 4-5. How one counts the number of particles in such peaks when they rest upon a sizable and curving background will be described with each fitting method.

The first approach to fitting the invariant mass distributions (Method I) was to approximate their shapes as a linear sum of a third-order polynomial for the background plus two gaussians for the J peak plus two gaussians for the small excesses at the ψ' mass and fit in the range from 2.0 GeV to 5.0 GeV. The values of the parameters for the secondary gaussian in each peak, however, were constrained in such a way that their relationship to the parameters of the first gaussian matched the relationship between the corresponding parameters in a two gaussian fit of the Monte Carlo lineshapes. In addition, because the ψ' excess was so small in each distribution, the central value of the ψ' primary gaussian was constrained to be that of the J central gaussian plus 0.589 GeV (the known J-ψ' mass difference) [49], and the widths were constrained to be the same. The latter

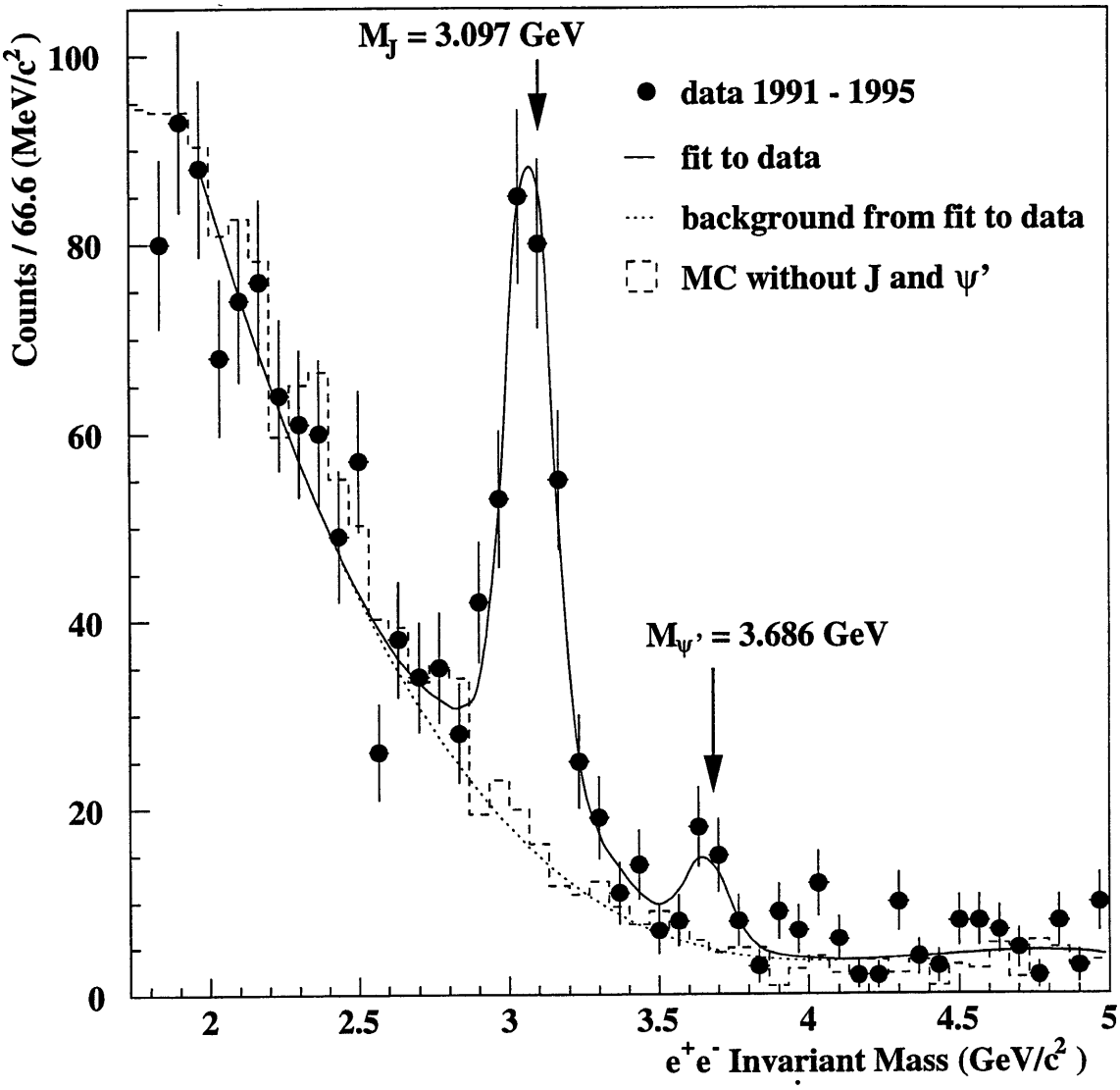

Figure 4-3: Dielectron invariant mass distribution
Invariant mass distribution for J and ψ' candidates in the dielectron channel.

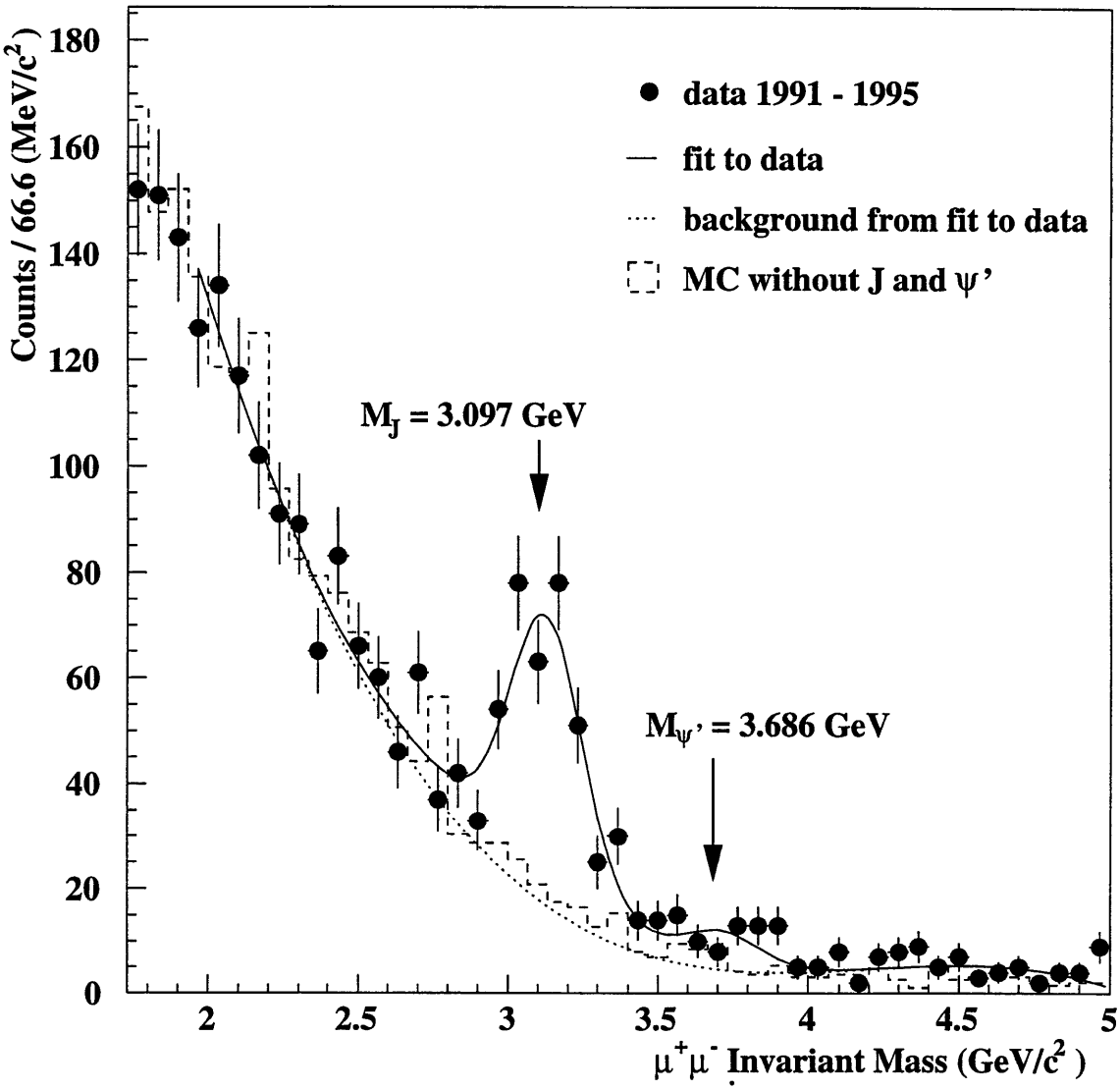

Figure 4-4: Dimuon invariant mass distribution
Invariant mass distribution for J and ψ' candidates in the dimuon channel.

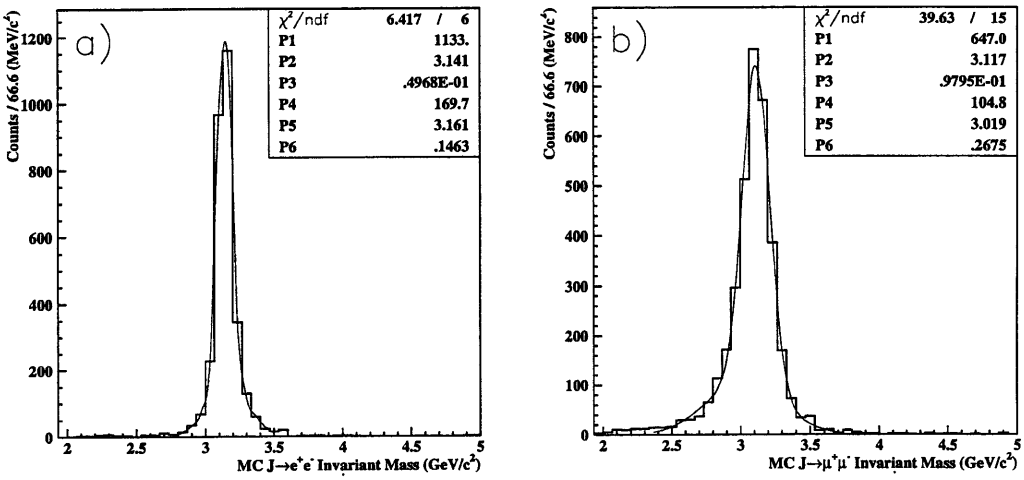

Figure 4-5: Monte Carlo J lineshapes
J lineshapes in the a) dielectron and b) dimuon channels for simulated Monte Carlo signal events. The signals have been fit with two gaussians, and good results have been achieved.

constraint is tantamount to assuming that the detector mass resolution remains constant over the range from 3.1 GeV to 3.7 GeV. According to Monte Carlo studies of the J and ψ' lineshapes, this is not strictly true, but it is approximately correct. One finds that the mass resolution in the dielectron channel is roughly 50 MeV for the J and 62 MeV for the ψ'. The corresponding values in the dimuon channel are 98 MeV and 116 MeV. Because the intrinsic width of the J and the ψ' are 86 keV and 278 keV, respectively, one can also conclude that the measured widths of these particles are dominated by detector resolution [49]. In the manner just described, the number of free parameters was reduced to a manageable level while retaining enough freedom to fit the signal properly. Applying this method to the mass distributions in Figure 4-3 and Figure 4-4 yielded the numbers shown in Table 4.4.

It is perhaps of some interest to comment briefly on the parameters of the fits. From the fit to the dielectron invariant mass distribution, a peak position of 3.071 GeV and a width of 72 MeV was found for the primary gaussian in the J peak. The corresponding parameter values from the fit to the dimuon invariant mass distribution were 3.128 GeV and 113 MeV. The peak position for the muons is higher than the nominal J mass value of 3.097 GeV, but this is seen also with the Monte Carlo peak as shown in Table 4.3. One can conclude from this that the muon peak position for data is in good agreement with that for Monte Carlo signal J's and that the shift relative to the nominal J peak is a consequence of the complicated lineshape. From visual inspection of Figure 4-5b, it is not surprising that the peak position of the primary J gaussian is not a very accurate estimator of the J mass. For the dielectron case, the peak position is found to be lower than the nominal J

Channel	Primary Gaussian Mean (GeV)		Primary Gaussian Width (MeV)	
	Data	Monte Carlo	Data	Monte Carlo
e^+e^-	3.071	3.141	72	50
$\mu^+\mu^-$	3.128	3.117	113	98

Table 4.3: J invariant mass peak fit parameters

mass, which for the reason just mentioned is not terribly significant. Since the Monte Carlo peak position in Figure 4-5a is at 3.141 GeV, however, the agreement between data and Monte Carlo is definitely worse than for the dimuons. The exact reason for this discrepancy is not obvious. Perhaps it is indicative of a fluctuation in the background underneath the peak in the data or possibly a minor calibration problem with the detector. Regarding the widths, one finds for Monte Carlo the values 50 MeV and 98 MeV for the dielectron and dimuon peaks, respectively. Thus, both of the data widths are in excess of the Monte Carlo expectations, and again, the reasons are not readily apparent. The degradation could be related to calibration problems, improperly accounted for time-dependent detector effects, or perhaps inaccurate Monte Carlo modeling at an even more fundamental level. Regardless of the source(s) of these differences, the measured numbers of mesons are unlikely to be influenced significantly.

	e^+e^-		$\mu^+\mu^-$	
	N_J	N'_ψ	N_J	N'_ψ
Method I	268 ± 23	30.1 ± 8.2	300 ± 29	33.6 ± 10.2
Method II	261 ± 23	34.5 ± 8.2	275 ± 29	30.4 ± 10.2
Average	265 ± 23	32.3 ± 8.2	288 ± 29	32.0 ± 10.2

Table 4.4: Measured numbers of J's and ψ''s with statistical errors
Numbers of J's and ψ''s determined by two different methods together with the averages

An alternative to this fitting method (Method II) was to obtain the background shape directly from Monte Carlo $q\bar{q}$ events containing no J's and ψ''s, normalize the mass distributions by the number of hadronic events, subtract the Monte Carlo background from the data, and fit the resulting difference with two gaussians (one for the J and one for the ψ'). To account for the non-gaussian behavior of the vector meson peaks, the numbers of mesons calculated from the gaussian fit parameters were multiplied by the following Monte Carlo derived correction factors: $C_{J\to e^+e^-} = 1.078$, $C_{J\to\mu^+\mu^-} = 1.067$, $C_{\psi'\to e^+e^-} = 1.058$, and $C_{\psi'\to\mu^+\mu^-} = 1.049$. The corrected numbers of J's and ψ''s determined in this way are also given in Table 4.4. Finally, averaging these results with those from Method I yields the final estimate of the numbers of J's and ψ''s from this analysis given in the last row of Table 4.4.

4.5 Systematic Errors

The main sources of systematic errors for the measurement of Br(Z $\rightarrow$ J+X)and Br(Z $\rightarrow \psi'$+X) were the choice of selection cuts, the efficiency corrections, the counting method, and the uncertainties in Br(J $\rightarrow \ell^+\ell^-$)and Br($\psi' \rightarrow \ell^+\ell^-$). Small additional systematics from finite Monte Carlo statistics, the influence of QCD charmonium production mechanisms on the selection efficiencies, and uncertainty in Br(Z $\rightarrow$ q$\bar{\text{q}}$) were also estimated. A full accounting of the J and ψ' systematics is given in Table 4.5 and Table 4.6. As stated in the previous section, the quoted error in the counting of

Source	$(\Delta Br/Br)_{J\rightarrow e^+e^-}$ (%)	$(\Delta Br/Br)_{J\rightarrow \mu^+\mu^-}$ (%)	$(\Delta Br/Br)_{comb.}$ (%)
J selection	$^{+5.4}_{-11.2}$	$^{+3.7}_{-9.3}$	$^{+3.3}_{-7.3}$
pseudo-ϵ correction	± 6.0	± 3.5	± 3.5
error on Br(J $\rightarrow \ell^+\ell^-$)	± 3.2	± 3.2	± 2.3
Monte Carlo statistics	± 1.5	± 1.4	± 1.0
fitting method	± 1.3	± 4.7	± 2.4
prompt J production	± 1.0	± 1.0	± 1.0
error on Br(Z $\rightarrow$ q$\bar{\text{q}}$)	± 0.2	± 0.2	± 0.2
TOTAL	$^{+9.0}_{-13.3}$	$^{+7.8}_{-11.6}$	$^{+6.0}_{-8.9}$

Table 4.5: Systematics for Br(Z $\rightarrow$ J + X)
Sources and magnitudes of systematic errors for the measurement of Br(Z $\rightarrow$ J + X).

Source	$(\Delta Br/Br)_{\psi'\rightarrow e^+e^-}$ (%)	$(\Delta Br/Br)_{\psi'\rightarrow \mu^+\mu^-}$ (%)	$(\Delta Br/Br)_{comb.}$ (%)
ψ' selection	$^{+43.9}_{-49.6}$	$^{+21.9}_{-27.0}$	$^{+24.5}_{-28.2}$
pseudo-ϵ correction	± 6.9	± 3.3	± 3.9
error on Br($\psi' \rightarrow \ell^+\ell^-$)	± 14.8	± 22.0	± 13.3
Monte Carlo statistics	± 1.9	± 1.9	± 1.3
fitting method	± 6.8	± 5.0	± 4.2
prompt ψ' production	± 1.0	± 1.0	± 1.0
error on Br(Z $\rightarrow$ q$\bar{\text{q}}$)	± 0.2	± 0.2	± 0.2
TOTAL	$^{+47.4}_{-52.7}$	$^{+31.7}_{-35.4}$	$^{+28.5}_{-31.8}$

Table 4.6: Systematics for Br(Z $\rightarrow \psi'$ + X)
Sources and magnitudes of systematic errors for the measurement of Br(Z $\rightarrow \psi'$ + X).

particles is one half the difference between the two counting methods used to obtain the final results. This error takes into account at once the dependencies on the background shape under the signal peaks, the form of the functions used to fit the signal, and the limits of the fit region. Uncertainties in branching ratios were taken directly from the 1996 Particle Data Group handbook [49]. Systematics arising from the particular choice of selection cuts used in this analysis were estimated by varying the cuts within reasonable limits and evaluating the changes in the measured Br(Z $\rightarrow$ J + X)and Br(Z $\rightarrow \psi'$ + X). The changes in the branching ratios were added in quadrature, and the square

root of the sum was taken as the total systematic error assigned to the selection. For this systematic error, the dominant contributions were from the cuts on the lepton momenta, but contributions from the other cuts were also non-negligible. It will be noted that the systematic error associated with the selection cuts for the measurement of $Br(Z \to \psi' + X)$ is very large compared to that for the other sources, but one should realize that the low statistics for the ψ' sample has much to do with this. Lastly, the systematic error associated with the efficiency correction procedure was conservatively estimated by varying the relevant partner lepton cuts, regenerating the pseudo-efficiency maps for both data and Monte Carlo events, recalculating the efficiency corrections, and taking the observed spread in these corrections as the systematic error.

4.6 Results

The formula shown below was used to calculate the branching ratios $Br(Z \to J + X)$and $Br(Z \to \psi' + X)$:

$$Br(Z \to V + X) = \frac{N_V}{N_{q\bar{q}}} \cdot \frac{1}{\pi_{q\bar{q}}} \cdot \frac{Br(Z \to q\bar{q})}{Br(V \to \ell^+\ell^-) \cdot \epsilon_{V \to \ell^+\ell^-}}$$

In the previous expression, 'V' is meant to stand for either J or ψ'. The values $Br(Z \to q\bar{q}) = 0.699 \pm 0.0015$, $Br(J \to \ell^+\ell^-) = 0.0601 \pm 0.0019$, $Br(\psi' \to e^+e^-) = 0.0088 \pm 0.0013$, and $Br(\psi' \to \mu^+\mu^-) = 0.0077 \pm 0.0017$ were taken from the 1996 Particle Data Group handbook [49]. Substituting the numbers given in the previous sections for N_J, $N_{q\bar{q}}$, $\pi_{q\bar{q}}$, $\epsilon_{J \to \ell^+\ell^-}$, and $\epsilon_{\psi' \to \ell^+\ell^-}$ one obtains:

$$Br(Z \to J + X)_{e^+e^-} = (3.45 \pm 0.30^{+0.31}_{-0.46}) \times 10^{-3}$$
$$Br(Z \to J + X)_{\mu^+\mu^-} = (2.96 \pm 0.30^{+0.23}_{-0.34}) \times 10^{-3}$$

$$Br(Z \to \psi' + X)_{e^+e^-} = (2.4 \pm 0.6^{+1.1}_{-1.3}) \times 10^{-3}$$
$$Br(Z \to \psi' + X)_{\mu^+\mu^-} = (2.4 \pm 0.8^{+0.8}_{-0.9}) \times 10^{-3}$$

Combining the results in each decay channel yields the final inclusive J and ψ' branching ratio measurements from this analysis:

$$Br(Z \to J + X)_{comb.} = (3.16 \pm 0.21^{+0.19}_{-0.28}) \times 10^{-3}$$
$$Br(Z \to \psi' + X)_{comb.} = (2.4 \pm 0.5^{+0.7}_{-0.8}) \times 10^{-3}$$

With $Br(Z \to J + X)_{comb.}$ in hand, it is then a simple matter to obtain the more fundamental quantity, $Br(b \to J + X)$. Recalling that J's in Z decays are produced primarily from b-hadron decays with a small contribution from prompt mechanisms, one can derive the expression below for this branching ratio:

$$Br(b \to J + X) = (1 - f_p) \cdot \frac{1}{2R_b} \cdot \frac{Br(Z \to J+X)}{Br(Z \to q\bar{q})}$$

Here, the Particle Data Group value of $R_b = .2213 \pm .0019$ will be used [49]. The quantity f_p is the fraction of prompt J's produced in Z decays, and its value is currently of interest both theoretically and experimentally. Several of the LEP groups have recently investigated or are presently investigating prompt J production in Z decays, and a determination of f_p from the 1991 - 1995 L3 data set will be made in a subsequent chapter. With the understanding that a full description of the L3 measurement is forthcoming, the result $f_p = 8.3 \pm 2.3 \pm 1.7 \pm 1.0\%$ is presented for the purpose of calculating $Br(b \rightarrow J + X)$. Using these numbers and the value of $Br(Z \rightarrow J + X)$ just measured, one obtains:

$$Br(b \rightarrow J + X) = (0.94 \pm 0.07^{+0.06}_{-0.09})\%$$

Two main conclusions can be drawn from this inclusive measurement. First, it is found to be in fair agreement with the value measured by the CLEO II experiment: $Br(b \rightarrow J + X) = (1.12 \pm 0.04 \pm 0.06)\%$ [61]. Thus, the relatively large value of this branching ratio seems to be well established. Secondly, because the two measurements are consistent, the branching ratio determined from L3 data, like that determined from CLEO II data, is in excess of older theoretical calculations of this quantity. Following the same comparison strategy as Bodwin, Braaten, and Lepage in [22], one can use this experimentally measured branching ratio to the J and recent determinations of the branching ratios below [61]:

$$Br(b \rightarrow \psi' + X) = (0.34 \pm 0.04 \pm 0.03)\% \quad (4.1)$$

$$Br(b \rightarrow \chi_c^1 + X) = (0.40 \pm 0.06 \pm 0.04)\% \quad (4.2)$$

$$Br(b \rightarrow \chi_c^2 + X) = (0.25 \pm 0.10 \pm 0.03)\% \quad (4.3)$$

to deduce $Br(b \rightarrow J + X)_{direct}$ by appropriately subtracting the feeddown contributions. Doing this, one finds $Br(b \rightarrow J + X)_{direct} = (0.61 \pm 0.07^{+0.07}_{-0.09})\%$, which is still several standard deviations away from the CSM baseline estimate of 0.23% [22]. It is rather close, however, to the improved VSM estimate 0.58% given by Ko, Lee, and Song, which includes contributions from relativistic corrections, radiative corrections, and one color octet term [24]. Unfortunately, uncertainties surrounding the impact of other color octet matrix elements on this calculation make the final estimate somewhat questionable, and the observed agreement with the Ko, Lee, and Song result might turn out to be purely coincidental. Hopefully, measurements in subsequent chapters will shed some light on this matter.

Chapter 5

χ_c Production

5.1 Introduction

Like their relative the J, χ_c's at LEP are produced primarily during the process of b-hadron decay. There are three of these P-wave states corresponding to total spins J = 0, 1, and 2. Because of the excellent electromagnetic calorimetry at L3, the strategy for measuring the branching ratio of the Z into χ_c states is to identify these states via their radiative decays to the J. Taking the relevant branching ratios into account, it is expected that the χ_c^1 will provide the dominant signal in the data. According to the VSM and CEM there could also be a small contribution from χ_c^2 as well, which would likely be inseparable from the χ_c^1 since the experimental resolution on the quantity

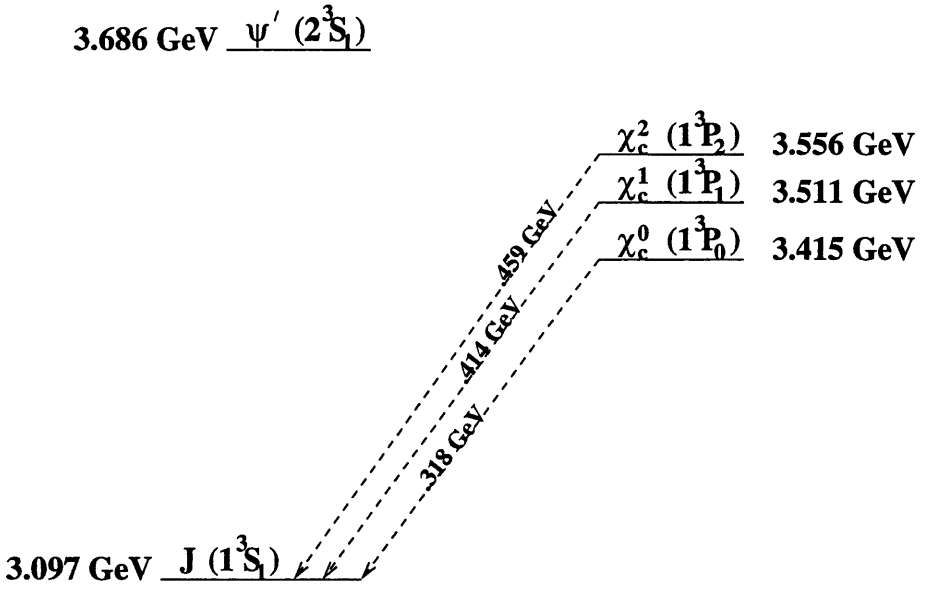

Figure 5-1: Pictorial diagram of the various bound states in the $c\bar{c}$ family

$M_{J\gamma} - M_J$ is approximately 25 MeV (see Figure 5-2) and the mass difference between the two states is a mere 45.6 MeV (see Figure 5-1). No significant signal is expected from the χ_c^0 because of its low branching ratio to Jγ, but if such a signal is present, it should be quite distinct from that of the χ_c^1 and χ_c^2 since in these cases the mass differences between the states are significantly larger than the experimental resolution.

5.2 χ_c Selection

In order to study the χ_c signal, two distinct samples were examined. The first χ_c sample was simply a subset of the b $\rightarrow$ J+X MC events that were generated for the inclusive J production measurement, and the second sample was a dedicated sample of 10000 events of the type $\chi_c^1 \rightarrow J + \gamma \rightarrow \ell^+\ell^- + \gamma$, where the dilepton decays were evenly distributed between the electron and muon channels. The first sample contained members of all three χ_c species (total angular momentum states) and was therefore used to study the signal mass difference ($M_{J\gamma} - M_J$) resolution of each. In addition, this sample was used to study the χ_c mass difference resolution in the two cases where J $\rightarrow e^+e^-$and J $\rightarrow \mu^+\mu^-$. The results are shown in Figure 5-2. These distributions suggest that the χ_c peaks in the $e^+e^-\gamma$

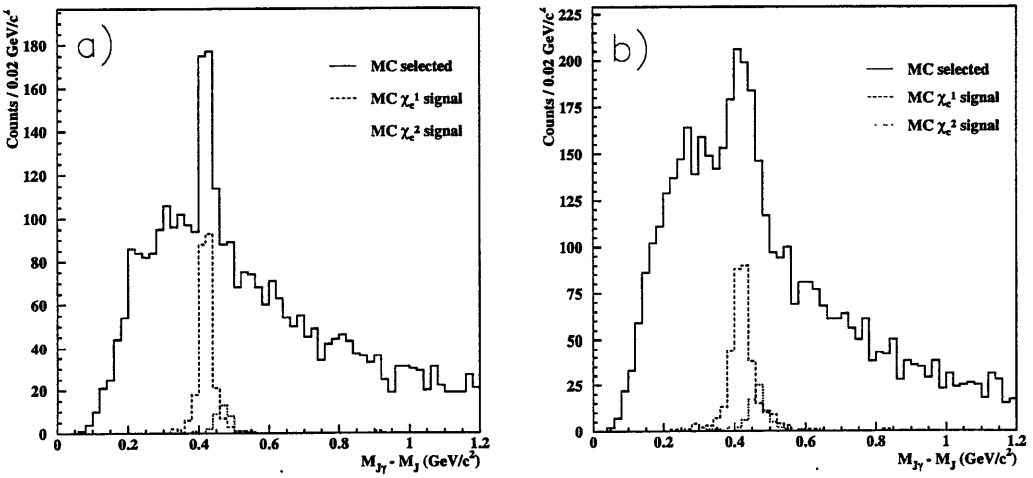

Figure 5-2: Monte Carlo χ_c signal shapes
a) using J$\rightarrow e^+e^-$ channel and b) using J$\rightarrow \mu^+\mu^-$ channel.

channel will probably be slightly narrower than the corresponding peaks in the $\mu^+\mu^-\gamma$ channel and that any χ_c^2 contribution is likely to be indistinguishable from the χ_c^1 contribution. The second, larger χ_c^1 sample was used to study the photon properties in radiative χ_c decays and to estimate the χ_c selection efficiency. Distributions of the two most important photon-related quantities, E_γ and $\theta_{J\gamma}$, are shown in Figure 5-3 and indicate that the photons are in the low to intermediate energy

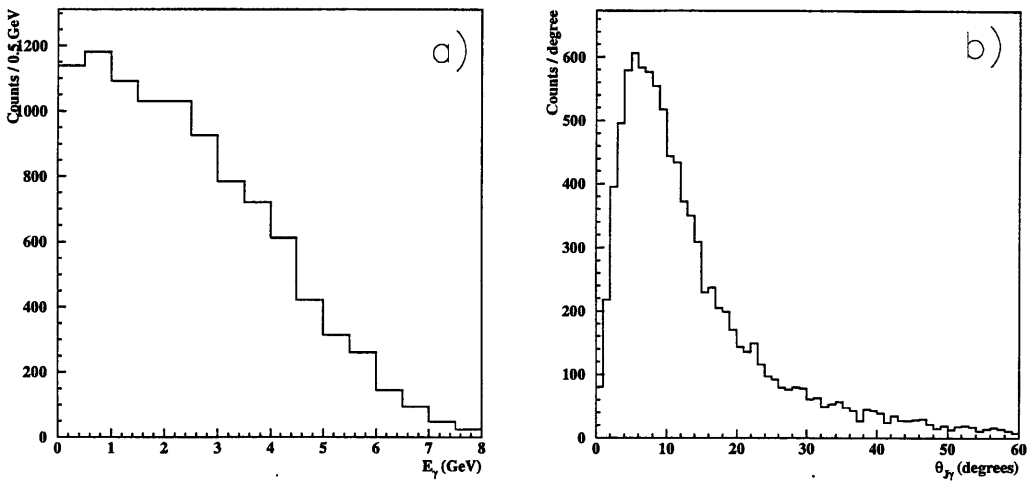

Figure 5-3: Properties of photons from χ_c decays as determined by Monte Carlo.
a) photon energy spectrum and b) distribution of the angle between the J and the photon in radiative χ_c decays to J mesons.

range and are in relatively close proximity to the J.

Selection of the χ_c's was designed to be rather straightforward. The same inclusive J selection described in Chapter 4 was used again to find the J's. For each J candidate in the peak region defined by 2.8 GeV $\leq M_{\ell^+\ell^-} \leq$ 3.4 GeV, a search was made for a photon near the J candidate with an energy in the expected energy range. The complete photon selection is listed below:

- 1.0 GeV $< E_{best-\gamma} <$ 8.0 GeV
- $(\Sigma_9/\Sigma_{25})_\gamma \geq 0.8$
- $(\chi^2_{EM})_\gamma \leq 12$
- $\theta_{J\gamma} < 40°$

Using this selection with the 10000 event MC χ_c^1 signal sample, the photon selection efficiencies for the electron and muon channels were determined to be $\epsilon_{\gamma(ee)} = 30.7\%$ and $\epsilon_{\gamma(\mu\mu)} = 38.9\%$ The significant difference between the two values is explained by the fact that events in which the J's decay to electrons contain much more activity in the ECAL, making it more difficult to find the low energy photons from the χ_c decays. Furthermore, it should be noted that a correction factor of 0.95 ± 0.05 was applied to the raw MC efficiencies for each J decay channel to obtain these estimates of ϵ_γ. This correction factor has been set to midway between the ideal (correction factor = 1.0) and the correction factor needed for a single electron (correction factor = 0.9) since the inefficiency of associating a good track to an electron bump clearly should not be applied in the case of a

photon. Lastly, it should be mentioned that the J selection efficiencies for the χ_c measurement ($\epsilon_{J\to e^+e^-} = .222$ and $\epsilon_{J\to\mu^+\mu^-} = .295$) were a bit lower from those quoted in Chapter 4 with the same selection because the dilepton invariant mass range considered was slightly smaller. Combining the photon efficiencies with the new J selection efficiencies, the overall χ_c^1 efficiency was estimated to be $\epsilon_{\chi_c^1} = 9.1\%$.

5.3 Data Analysis

Because the data statistics for this selection were low, it was deemed preferable to fix the shape of the background, normalize to the number of background in the data, and count the excess signal in the peak region rather than fit the data with a gaussian plus a background function. Therefore, the first step in making the χ_c measurement was to establish the background shape. For this purpose, three independent samples were used: fake J candidates from data in the range 2.0 GeV $\leq M_{\ell^+\ell^-} \leq$ 2.7 GeV combined with photon candidates, fake J candidates from approximately 9×10^6 MC $q\bar{q}$ events in the range 2.8 GeV $\leq M_{\ell^+\ell^-} \leq$ 3.4 GeV combined with photon candidates, and real J's from signal MC events with all χ_c's vetoed combined with random photon candidates. The resulting mass difference plots were all perfectly consistent with each other and were added together to increase

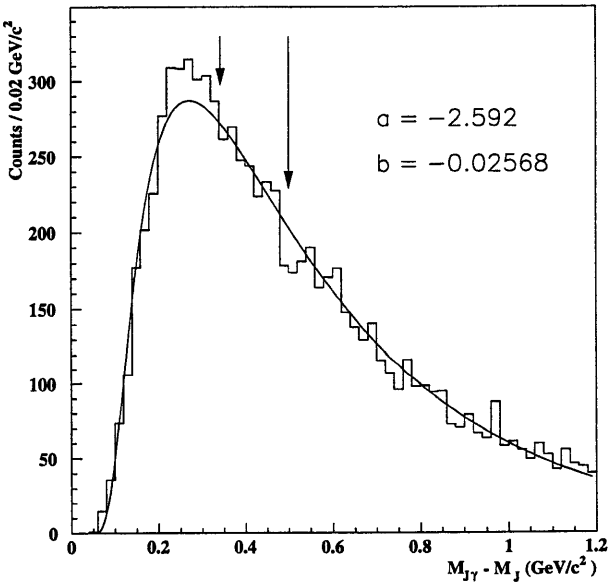

Figure 5-4: Background $M_{J\gamma} - M_J$ distribution
The histograms were obtained using data events from the low M_J sideband, MC $q\bar{q}$ events without real J's, and MC signal J events without real χ_c's. The fit function is of the form e^{ax+b/x^2}. The vertical arrows indicate the signal region.

the statistics for an improved fit. Several functional forms were fit to the background, and the best fit was obtained using e^{ax+b/x^2}. The fit yielded the shape parameters $a = -2.592$ and $b = -0.02568$

as shown in Figure 5-4.

Applying the selection described in the previous section to the data resulted in the mass difference plot shown in Figure 5-5, where the electron and muon channels have been added together. The

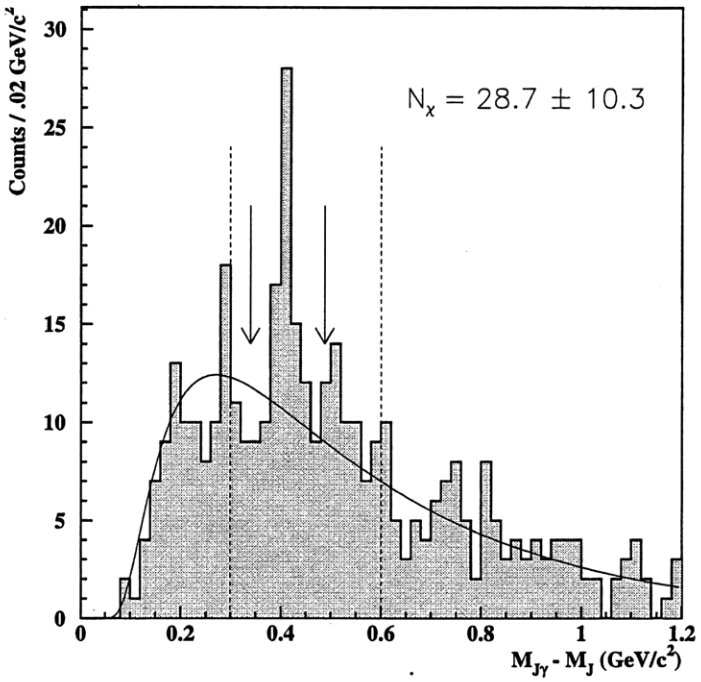

Figure 5-5: Data $M_{J\gamma} - M_J$ distribution
The solid curve is the normalized background function, where the normalization has been performed using data in the regions above and below the vertical dotted lines. The arrows indicate the defined signal region.

solid curve is the background function normalized using the number of candidates below 0.3 GeV and above 0.6 GeV. The signal region is indicated by the two solid arrows. A clear peak is obvious near 0.414 GeV where one expects a χ_c^1 signal to appear, and it should be noted that excesses are observed in both the electron and muon J decay subsamples. No clear excess is seen at 0.459 GeV to signal a large contribution from χ_c^2, and therefore, no attempt has been made to subtract the χ_c^2's from the peak to obtain the number of χ_c^1's. Interpreting the peak to be a χ_c^1 signal, the number of χ_c^1's is estimated by counting the number of candidates satisfying 0.340 GeV $\leq M_{J\gamma} - M_J \leq$ 0.488 GeV (the $\pm 3\sigma$ range for the MC signal χ_c^1 peak) and subtracting the integral of the background function over this same range. The result is $N_{\chi_c^1} = 28.7 \pm 10.3$, where the error is statistical only.

5.4 Systematic Errors

Many of the systematic errors associated with the inclusive J measurement were common to the χ_c measurement, eliminating the need to recalculate them. Among these were the error on $Br(Z \to q\bar{q})$, the error on $Br(J \to \ell^+\ell^-)$, and the error associated with the J selection efficiency due to the selection cuts, the correction factor, prompt production, and finite MC statistics. Of course, other systematic errors, namely those related to the photon selection efficiency and the counting method, had to be estimated for the first time. The error associated with the photon selection was estimated in the standard fashion by varying the cuts within reasonable limits and observing the change in the measurement. One will note that the lower bound of this systematic error is quite large and is dominated by the variation of the cut on $(\Sigma_9/\Sigma_{25})_\gamma$. When the cut was loosened to $(\Sigma_9/\Sigma_{25})_\gamma \geq 0.75$,

Error Source	Quantity Affected	Quantity Range	$(\Delta Br/Br)(\%)$
error on $Br(Z \to q\bar{q})$	$Br(Z \to q\bar{q})$	$0.698 - 0.700$	± 0.2
error on $Br(J \to \ell^+\ell^-)$	$Br(J \to \ell^+\ell^-)$	$0.0587 - 0.0615$	± 2.3
error on $Br(\chi_c \to J + \gamma)$	$Br(\chi_c \to J + \gamma)$	$0.257 - 0.289$	± 5.9
J selection	ϵ_J	$0.204 - 0.240$ (ee) $0.276 - 0.314(\mu\mu)$	± 5.1
J pseudo-ϵ correction	ϵ_J	$0.209 - 0.235$ (ee) $0.285 - 0.305(\mu\mu)$	± 3.2
prompt J production	ϵ_J	$0.220 - 0.224$ (ee) $0.292 - 0.298(\mu\mu)$	± 1.0
signal J MC statistics	ϵ_J	$0.218 - 0.226$ (ee) $0.290 - 0.300(\mu\mu)$	± 1.3
photon selection	ϵ_γ	$0.222 - 0.331$ (ee) $0.281 - 0.419(\mu\mu)$	$^{+7.7}_{-27.7}$
photon pseudo-ϵ correction	ϵ_γ	$0.292 - 0.332$ (ee) $0.370 - 0.408(\mu\mu)$	± 5.0
signal χ_c MC statistics	ϵ_γ	$0.295 - 0.319$ (ee) $0.377 - 0.401(\mu\mu)$	± 2.3
background extrema		0.2 - 0.3 and 0.6 - 0.9	± 4.0
background parameters	a and b	$-2.657 < a < -2.527$ $-0.02678 < b < 0.02458$	± 10.3
background statistics	$N_{bg-norm}$	$193.6 - 222.4$	± 6.9
χ_c^2 contamination	N_χ	25.8	-10.0
TOTAL			$^{+18.4}_{-33.9}$

Table 5.1: Systematics for $Br(Z \to \chi_c^1 + X)$
Sources and magnitudes of systematic errors for the measurement of $Br(Z \to \chi_c^1 + X)$.

the background increased substantially, and therefore, the statistical error of the background in the signal region was significantly larger. This happened to result in a lower measured number of χ_c's for approximately the same efficiency, which explains the systematic effect. In other words, the estimate of the systematic error associated with the photon selection includes, at least partially, the

statistical error and, therefore, is a conservative estimate. As noted before, the uncertainty assigned to the photon efficiency correction factor was ±5%, and the limited statistics for the MC signal χ_c's resulted in a small systematic error of ±3.2%. Three sources of error were considered to affect the background estimate inside the signal region: the parameters of the background function, the limited data statistics in the mass difference distribution sidebands, and the sideband extrema used to determine the overall normalization. The systematic uncertainties assigned were ±10.3%, ±6.9%, and ±4.0%, respectively. The first of these is fairly large, a result of varying independently the background function parameters, which are actually highly correlated. Hence, this systematic error is also very conservatively estimated. Finally, the systematic error on the number of χ_c^1's due to χ_c^2 contamination in the peak region has been estimated to be −10%.

5.5 Results

With the number of χ_c's and the associated systematic errors in hand, one can calculate the inclusive branching ratio, $\mathrm{Br}(Z \to \chi_c^1 + X)$. For this purpose, the following formula was used:

$$\mathrm{Br}(Z \to \chi_c^1 + X) = \frac{N_\chi}{N_{q\bar{q}}} \cdot \frac{1}{\pi_{q\bar{q}}\epsilon_{\chi_c^1}} \cdot \frac{\mathrm{Br}(Z \to q\bar{q})}{2\mathrm{Br}(J \to \ell^+\ell^-)\mathrm{Br}(\chi_c^1 \to J\gamma)}$$

where it is understood that:

$$\epsilon_{\chi_c^1} = \frac{\epsilon_{J\to e^+e^-} \cdot \epsilon_{\gamma(e^+e^-)} + \epsilon_{J\to \mu^+\mu^-} \cdot \epsilon_{\gamma(\mu^+\mu^-)}}{2}$$

Plugging in the numbers yields the result:

$$\mathrm{Br}(Z \to \chi_c^1 + X) = (1.9 \pm 0.7^{+0.3}_{-0.6}) \times 10^{-3}$$

Working under the assumption that the bulk of the observed χ_c^1 sample is produced from b hadrons, it is trivial to convert this into a branching fraction of the b instead of the Z by using an expression analagous to that used with the case of the J. Using the same value of f_p as before, one finds:

$$\mathrm{Br}(b \to \chi_c^1 + X) = (0.55 \pm 0.20^{+0.10}_{-0.19})\%$$

This result is in good agreement with the recently published CLEO II branching ratio of $(0.40 \pm 0.06 \pm 0.04)\%$ [61].

When comparing the experimentally determined production rate of χ_c^1 with theory, it is useful to examine the ratio $R_{\chi_c^1}$:

$$R_{\chi_c^1} = \frac{\mathrm{Br}(b \to \chi_c^1 + X)}{\mathrm{Br}(b \to J + X)} \tag{5.1}$$

The CSM expectation for this quantity is $R_{\chi_c^1} = 0.24$, which can be calculated from the direct production estimates in [13] by including feeddown. The measurement of $\mathrm{Br}(b \to \chi_c^1 + X)$ above and the measurement of J production in Chapter 4, however, yield:

$$R_{\chi_c^1} = (0.58 \pm 0.22^{+0.12}_{-0.21})$$

Though the measured $R_{\chi_c^1}$ is higher by a factor of more than two than the CSM prediction, this still represents only a 1σ discrepancy and by itself means little. Unfortunately, a meaningful comparison of this χ_c^1 production measurement with a VSM prediction is not yet possible. Only recently have the first numerical estimates of J production from b-hadron decays which attempt to account for color octet processes as well as radiative corrections appeared in the literature. Such detailed calculations are still lacking for the P-wave states, and without them direct comparisons between theory and experiment are perhaps a bit premature. Moreover, even if they were available, the sizable experimental errors associated with this particular measurement would probably preclude one from drawing any definite conclusions regarding the validity of the theoretical calculations. Therefore, to better test the various theoretical heavy quarkonium production models, it will be necessary to study other processes involving charmonium as well. One of these, prompt J production, will be the topic investigated in the next chapter.

Chapter 6

Prompt J Production

6.1 Overview

From experiment and theory it is known that b-hadron decay is the primary source of J's in e^+e^- collisions at the Z pole. However, it is expected that several percent of all J mesons in Z decays are produced via various QCD mechanisms. Because these mechanisms usually do not involve b-quarks and, therefore, the b-lifetime, J's produced in this way are referred to as prompt. As described in Chapter 1, five Feynman diagrams have been considered in the literature which contribute to prompt J production in Z decays, three of the color singlet type and two of the color octet type. Again, they are color singlet c-fragmentation, gluon fragmentation, and gluon radiation and color octet gluon fragmentation and gluon radiation. Of these five, the color octet gluon fragmentation and color singlet charm fragmentation processes are dominant and according to the VSM account for approximately 92% of all prompt J's in Z decays (see Table 1.1) [12] [48] [29]. Unfortunately, these two types of events are dissimilar, making it difficult to design a selection with a large acceptance for both which also rejects the overwhelming J background from b-hadrons.

In order to study prompt J's, a prompt heavy quarkonium Monte Carlo generator borrowed from the OPAL Collaboration was used to create samples of 10000 events each for the four most important prompt mechanisms, with half of the J's forced to decay to $e^+e^-$and half to $\mu^+\mu^-$. In Chapter 1 theoretical calculations of color octet gluon radiation were presented, which showed that this process is extremely suppressed relative to the other prompt processes and that its effects are negligible. Therefore, no Monte Carlo samples of J's produced via color octet gluon radiation were ever made. A variety of individual event and J candidate variables, including the event thrust magnitude, the number of jets, the energy sum for jets excluding the two most energetic jets, the angle between the J candidate direction and the thrust axis, the J candidate energy, and the energy in the 30° cone around the J candidate direction excluding the J energy, hereafter referred to as E_{30}, were

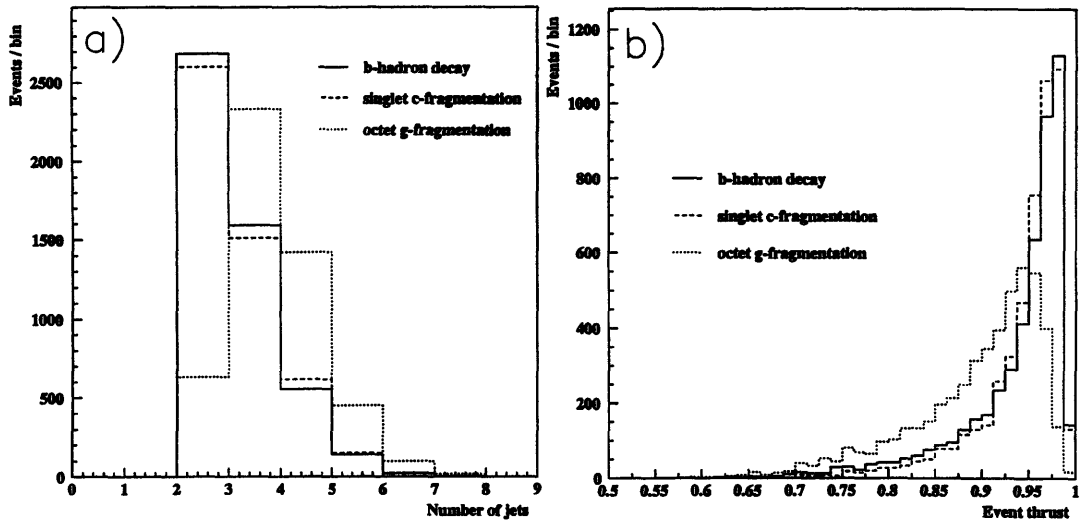

Figure 6-1: Monte Carlo J event distributions
a) number of jets in event and b) magnitude of the event thrust for different J sources.

initially examined for possible use in discriminating prompt J's from J's from b-hadron decays. The distributions of a few of these variables for the dominant prompt J process samples and for the b-hadron decay J sample are shown in Figures 6-1 and 6-2. From these plots, one can see that prompt J's produced via these processes are sufficiently different that no cut on a single variable is able to cleanly separate all the prompt J's from the b-hadron decay J background. Some of the variables, like the thrust magnitude, have little discriminating power at all. Others, like the J energy and the number of jets, can help distinguish only certain types of prompt J's from b-hadron decay J's. One finds, for example, that J's from c-fragmentation are rather hard like those from b-hadron decays, while the J's from gluon fragmentation have a much softer spectrum. Similarly, for both c-fragmentation events and b-hadron decay events, there is a high probability to have either two jets or three jets, while the other QCD mechanisms almost always yield three or more jets. Finally, one can see that the isolation energy, E_{30}, is the only variable found with reasonable discriminating power for all prompt J's. E_{30} is usually quite large for b-hadron decay J's and much lower for most prompt J's, and even the c-fragmentation events, which topologically and in other ways are very similar to b-hadron decay events, have an E_{30} distribution peaked at low energies. The shapes of these E_{30} distributions are fairly easy to explain. For gluon fragmentation events the J's are produced from a fairly soft and isolated jet and therefore have little extra energy nearby. In contrast, J's produced during the process of b-hadron decay are often found deep inside jets with considerable calorimetric activity in their vicinity. As for c-fragmentation J's, they tend to carry so much energy that there is little left over in their immediate surroundings, and hence, E_{30} is low. Using this information, it was possible to design a reasonably efficient prompt J selection meeting the requirement of nearly

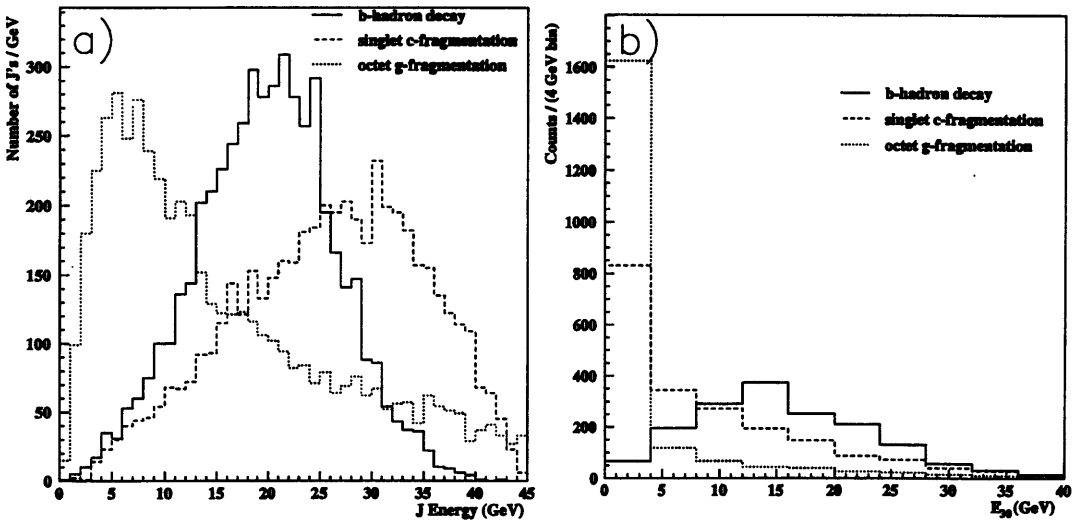

Figure 6-2: Monte Carlo J distributions
a) J energy spectrum and b) energy in the 30° cone around the J excluding the J energy for different J sources.

absolute rejection for J mesons from b-hadron decays.

6.2 Prompt J Selection

Several factors were considered in creating the selection for prompt J's. First, because the color singlet charm fragmentation and color octet gluon fragmentation contributions dominate prompt J production, little attention was given to the other QCD processes for selection purposes. These subordinate mechanisms, of course, were included in the determination of the final weighted prompt efficiency after the selection was frozen. Second, since color octet gluon fragmentation is expected to be more important than color singlet charm fragmentation for the overall prompt sample, this process was given priority in setting the cuts. Because of large theoretical uncertainties in the individual process rates and, to a certain extent, the process modelling, no attempt was made to actually optimize the prompt J signal to b-hadron decay J background ratio. Instead, the cuts were chosen to reject as much as possible the fake background and real b-hadron decay J background while retaining sufficient sensitivity to the prompt J's. This approach was adopted in order to provide convincing evidence that real prompt J's could be seen in the data. By forcing the efficiency for b-hadron decay J's to be very low, the hypothesis that the final J sample was explained solely by this source was made improbable.

With these factors in mind, a prompt selection centered around the quantity E_{30} was developed. Because most prompt J's are spatially separated from other energy deposition and b-hadron decay J's are not, the cut on E_{30} performs most of the work in the selection. The remainder of the

selection was kept identical to that used for the inclusive measurement in Chapter 4 save for a few minor exceptions. Since the gluon fragmentation J's typically have low energy, the energy sum of the two leptons for each J candidate was required to be at least 5 GeV instead of at least 8 GeV, increasing slightly the kinematic acceptance. In addition, the maximum lepton-lepton opening angle was lowered from 90° to 80°. This had the effect of eliminating to some extent some troublesome background from leptons in different jets which resulted in candidates at high J masses making the invariant mass distribution difficult to fit. Because the prompt J's are so isolated, the electromagnetic requirements for the electron candidates were tightened slightly in order to more efficiently reject fake background. Finally, for dimuon J candidates the cut on Z0 was reduced to $3\sigma_{Z0}$ from $5\sigma_{Z0}$ for the most energetic muon. The complete prompt J selection is given below for $J \rightarrow e^+e^-$:

- $E_{best-2} > 1.0$ GeV
- $E_{best-1} + E_{best-2} > 5.0$ GeV
- $(\Sigma_9/\Sigma_{25})_1 \geq 0.9$ and $(\Sigma_9/\Sigma_{25})_2 \geq 0.9$
- $(\chi^2_{EM})_1 \leq 8$ and $(\chi^2_{EM})_2 \leq 8$
- $(\Delta\phi_{ASRC-ATRK})_1 < 3\sigma_{\Delta\phi}$ and $(\Delta\phi_{ASRC-ATRK})_2 < 3\sigma_{\Delta\phi}$
- $R_1 = (|1/E_t - 1/p_t|)_1 < 3\sigma_R$ and $R_2 = (|1/E_t - 1/p_t|)_2 < 4\sigma_R$
- $\theta_{open} < 80°$
- $E_{30-ee} < 2.5$ GeV

and for $J \rightarrow \mu^+\mu^-$:

- $|p_{\mu-2}| > 2.0$ GeV
- $|p_{\mu-1}| + |p_{\mu-2}| > 5.0$ GeV
- $RDCA_1 < 3\sigma_{RDCA}$ and $RDCA_2 < 3\sigma_{RDCA}$
- $|Z0_1| < 3\sigma_{Z0}$ and $|Z0_2| < 3\sigma_{Z0}$
- $NPSEG_1 \geq 2$ and $NPSEG_2 \geq 2$
- $NZSEG_1 \geq 1$ and $NZSEG_2 \geq 1$
- $\theta_{open} < 80°$
- $E_{30-\mu\mu} < 4.0$ GeV

J source	ϵ (%)	Fraction of prompt sample	Weighted ϵ (%)
color singlet c-fragmentation	8.88	0.239	2.12
color singlet g-fragmentation	6.54	0.082	0.54
color singlet g-radiation	16.17	0.003	0.04
color octet g-fragmentation	20.63	0.677	13.96
Prompt sources (combined)	—	—	16.66
b-hadron decay	—	—	0.30

Table 6.1: J efficiencies (prompt selection)
Estimated efficiencies for various signal J production mechanisms using the prompt J selection.

By using this selection with the Monte Carlo prompt J and b-hadron decay J samples, the efficiencies in the first column of Table 6.1 were ascertained. Also given in Table 6.1 are the prompt sample fractions based on the theoretical production rates in Table 1.1. These fractions, or weights, indicate to what extent each individual process contributes to the total prompt J sample in Z decays. Multiplying the fraction by the corresponding efficiency for each process and summing over the processes yields the weighted efficiency for selecting prompt J mesons with the prompt J selection. As will be described shortly, the efficiencies for the same production processes using the general selection of Chapter 4 are also needed to determine $f_p = N_p/N_{J-tot}$. These are summarized in Table 6.2.

J source	ϵ (%)	Fraction of prompt sample	Weighted ϵ (%)
color singlet c-fragmentation	33.16	0.239	7.93
color singlet g-fragmentation	19.52	0.082	1.60
color singlet g-radiation	28.70	0.003	0.07
color octet g-fragmentation	25.61	0.677	17.33
Prompt sources (combined)	—	—	26.93
b-hadron decay	—	—	27.72

Table 6.2: J efficiencies (general selection)
Estimated efficiencies for various signal J production mechanisms using the general J selection from Chapter 4.

6.3 Data Analysis

Applying the prompt J selection to the 1991-1995 L3 data set, 53 J candidates were observed in the mass window from 2.733 GeV to 3.467 GeV. The $e^+e^-$and $\mu^+\mu^-$channels were summed together to provide the statistics necessary to measure the J peak, and a blow-up of the signal region of the resulting invariant mass distribution is shown in Figure 6-3. It should be noted that a small but identifiable signal was seen in each channel individually. The data distribution was then fit using a third-order polynomial for the background and a simple gaussian for the J peak. Information about the lineshapes for $J \to e^+e^-$and $J \to \mu^+\mu^-$was not used since the distributions for the $e^+e^-$and

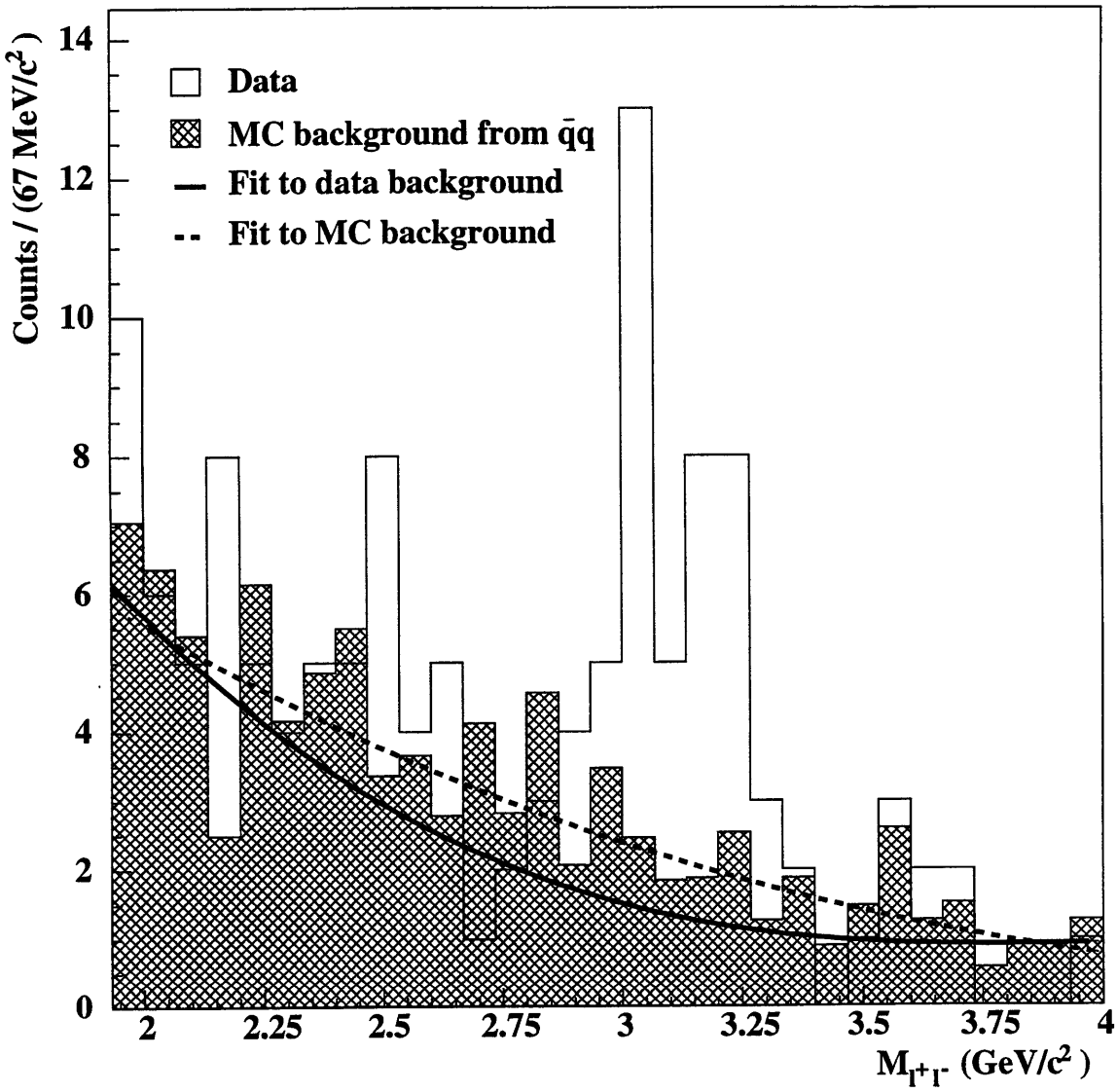

Figure 6-3: Prompt J selection invariant mass distribution
Invariant mass distribution with $e^+e^-$and $\mu^+\mu^-$channels combined (solid histogram), properly normalized background invariant mass distribution from Monte Carlo $q\bar{q}$ events (hatched histogram), polynomial fit to data background (solid line), and polynomial fit to Monte Carlo background (dashed line).

$\mu^+\mu^-$channels were combined in a single histogram . An integral of the background polynomial (solid line in Figure 6-3) yielded 15.6 events as the background under the peak. A completely independent estimate of the peak background of 24.2 events was obtained by appropriately rescaling and fitting the distribution resulting from analyzing approximately 1.0×10^7 Monte Carlo $q\bar{q}$ events (hatched histogram and dashed line in Figure 6-3). The best estimate of this peak background was taken to be the average of 19.9 events, and therefore, the estimated number of J's was 33.1. All 53 of the candidates in the mass window were visually scanned for signs of anything out of the ordinary. In most cases, the J candidates were soft, and the events looked like standard $q\bar{q}$ events. However,

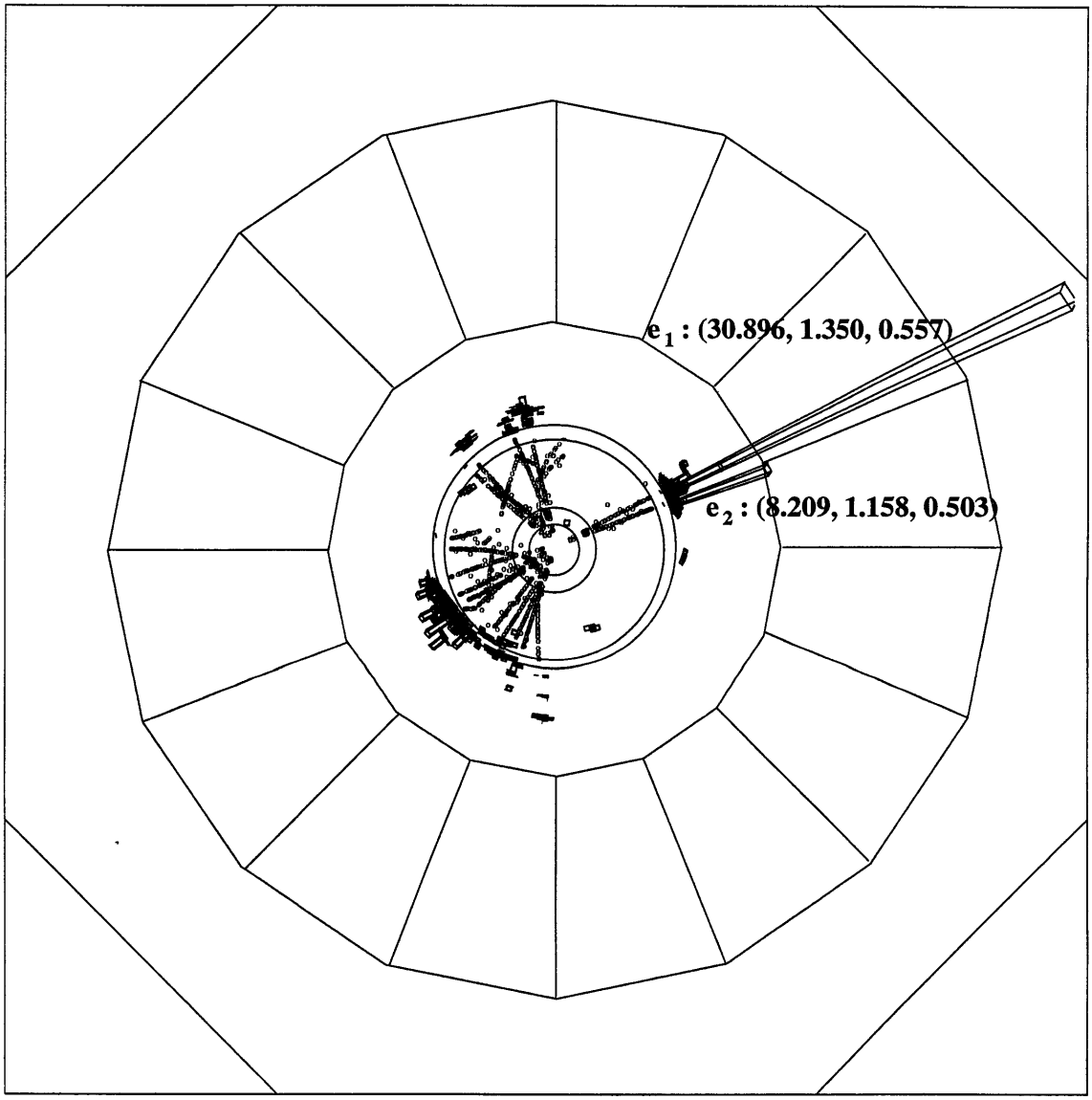

Figure 6-4: High energy prompt $J \rightarrow e^+e^-$ candidate
L3 run #489505 event #280 from 1994 data. Coordinates are of the form (|p|, θ, ϕ).

a few of the events contained highly energetic J candidates that were strikingly isolated. Three of these prime c-fragmentation J candidate events are displayed in Figures 6-4, 6-5, and 6-6 together with the lepton momenta.

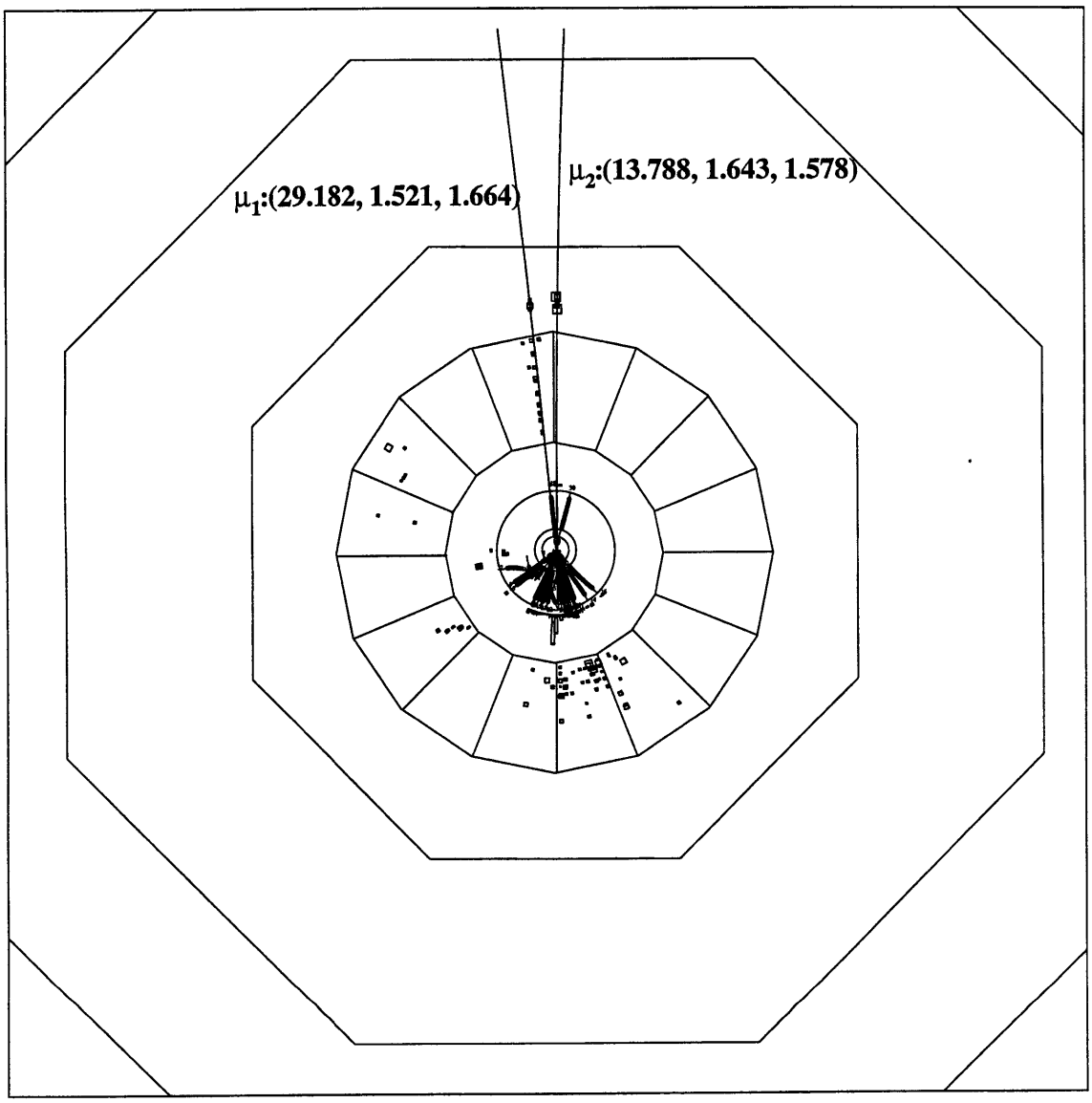

Figure 6-5: High energy prompt J $\rightarrow \mu^+\mu^-$ candidate
L3 run #322405 event #2047 from 1991 data. Coordinates are of the form (|p|, θ, ϕ).

6.4 Data Checks

After applying the prompt selection, several tests were performed not only to check the agreement between data and Monte Carlo but also to lend credence to the hypothesis of prompt QCD mecha-

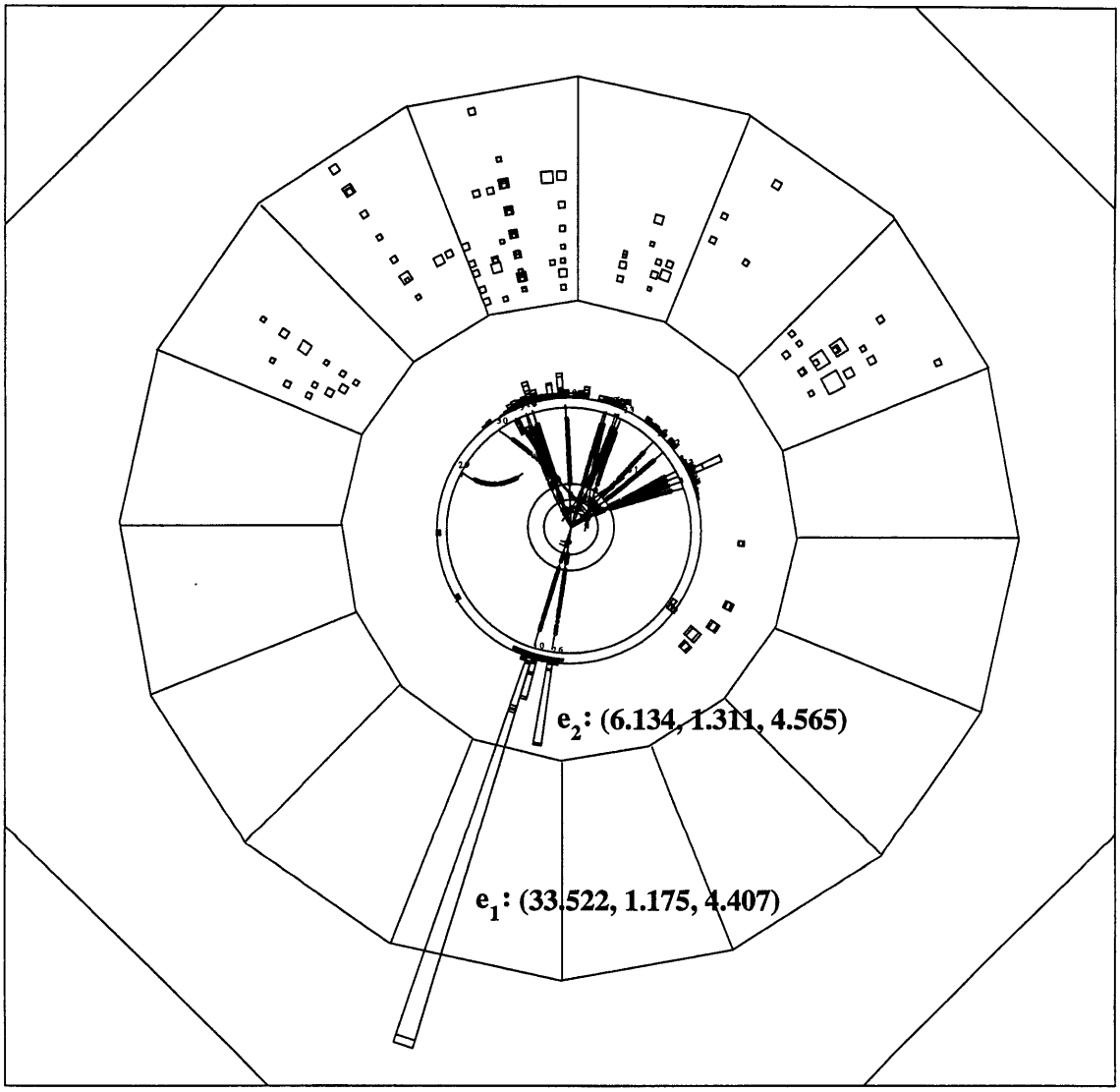

Figure 6-6: High energy prompt $J \rightarrow e^+e^-$ candidate
L3 run #638932 event #203 from 1995 data. Coordinates are of the form (|p|, θ, ϕ).

nisms as the primary source of the J's in the final selected sample. The first such test was simply to compare the observed energy spectrum of the J candidates in the data to that of a Monte Carlo sample composed of appropriately weighted contributions from $q\bar{q}$ background, b-hadron decay J signal, and prompt J signal. The resulting spectra are shown in Figure 6-7. The agreement is satisfactory given the paucity of data events, although it appears that the data spectrum is perhaps slightly softer than that of the Monte Carlo sample. Further comparison of the data spectrum with those of the individual prompt mechanisms does not elucidate the matter, for none of the latter are quite so strongly peaked at low energies. Therefore, one cannot gain much insight into the composition of the prompt J sample from a cursory inspection of the energy spectrum.

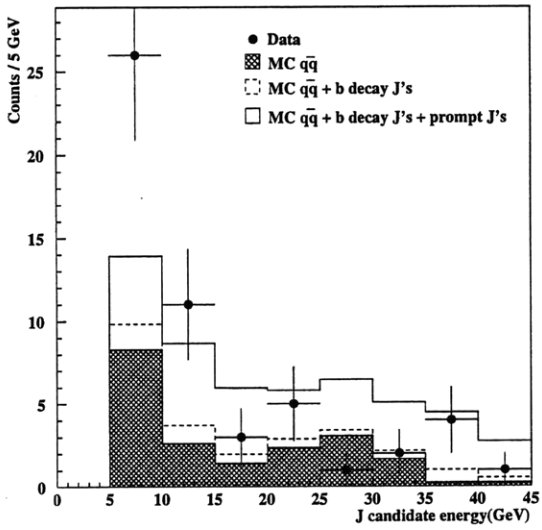

Figure 6-7: Prompt J candidate energy spectrum
Energy spectrum for the prompt J data candidates in the mass window from 2.733 GeV to 3.467 GeV (dots) together with the expected contributions from Monte Carlo events (hatched, dashed, and solid histograms).

Comparisons between data and Monte Carlo were also made for two additional distributions, the angle between the J candidate and the most energetic jet and the b-tag discriminant variable (for 1994 and 1995 data). The relevant plots are shown in Figure 6-8. For the angle to the most energetic jet in Figure 6-8a, reasonable agreement is again found. Unfortunately, this does not constitute strong evidence for the existence of prompt J's in the data sample since all of the distributions for this variable are similar in shape once the prompt selection is applied. At first glance this is somewhat surprising because the distributions for loosely selected samples are quite different from one another. Candidates from pure samples of b-hadron decay J and c-fragmentation J events tend to be closely aligned with or anti-aligned with the most energetic jet, while gluon-fragmentation candidates are commonly found over a wide range of angles relative to the most energetic jet. The similarity of the post-prompt selection distributions is made plausible, however, when one recognizes that the cut

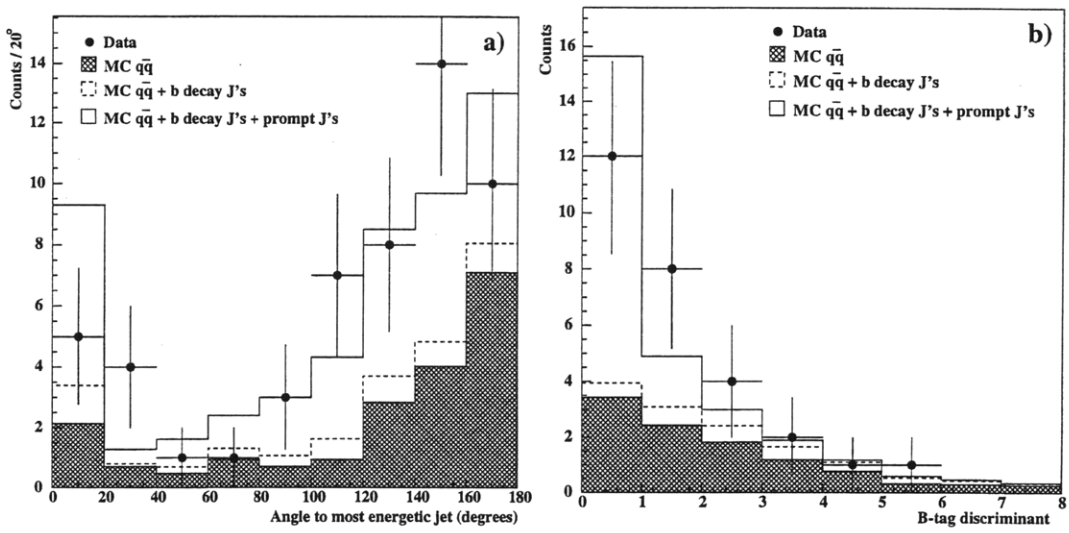

Figure 6-8: Prompt J candidate variable distributions
Distributions of the angle between the J and the most energetic jet and the b-tag discriminant variable for prompt J data candidates in the mass window from 2.733 GeV to 3.467 GeV (dots) together with the expected contributions from Monte Carlo events (hatched, dashed, and solid histograms).

on E_{30} is basically an isolation cut. It is natural, therefore, that the few b-hadron decay J's that survive the prompt selection are found far from the most energetic jet, and the same holds for the background. The gluon-fragmentation J's by their very nature are already relatively isolated before prompt selection, however, so the distribution for this sample of events is changed little except for the removal of a sharp peak at low angles (cases where the gluon jet happens to be the most energetic jet). The distribution of the b-tag discriminant variable is displayed in Figure 6-8b and is peaked at low values as expected. Events with measurable lifetime information (b-quark and, to some extent, c-quark events) have larger values for the b-tag discriminant variable, and uds-quark events have lower values. One should note that only 28 of the 53 prompt candidates show up in Figure 6-8b since the SMD is essential to the determination of the b-tag discriminant variable, and this subdetector was available only for the 1994 and 1995 runs (57% of the 1991-1995 data set). Because the background is largely from $Z \rightarrow b\bar{b}$ events, the contribution of this sample to the full distribution extends to high values of the b-tag discriminant. The same can be said, of course, for the b-hadron decay J sample contribution (the difference between the dashed histogram and the hatched histogram in Figure 6-8b, which, proportionally, has even greater population of the higher bins. Overall, the data appear to be more sharply peaked at lower values of the b-tag discriminant than for either the background or the b-hadron decay J samples, and qualitative agreement is observed between the data and the full Monte Carlo distribution, which includes the contributions from the prompt processes. Because there are so few data events, however, little more can be said.

6.5 Systematic Errors

The first task that was undertaken in the study of the systematic errors for the prompt J measurement was to examine the J energy spectrum and E_{30} distribution after applying the general J selection of Chapter 4. This was deemed necessary since the E_{30} is so critical to the entire prompt J selection. Without a fairly good Monte Carlo description of this variable, it is conceivable that one could mistakenly interpret an observed excess of J's as prompt when in truth they could simply be products of the common b-hadron decay process. The J energy spectra and E_{30} distributions from data together with the Monte Carlo expectations are shown in Figures 6-9 and 6-10. It is worth

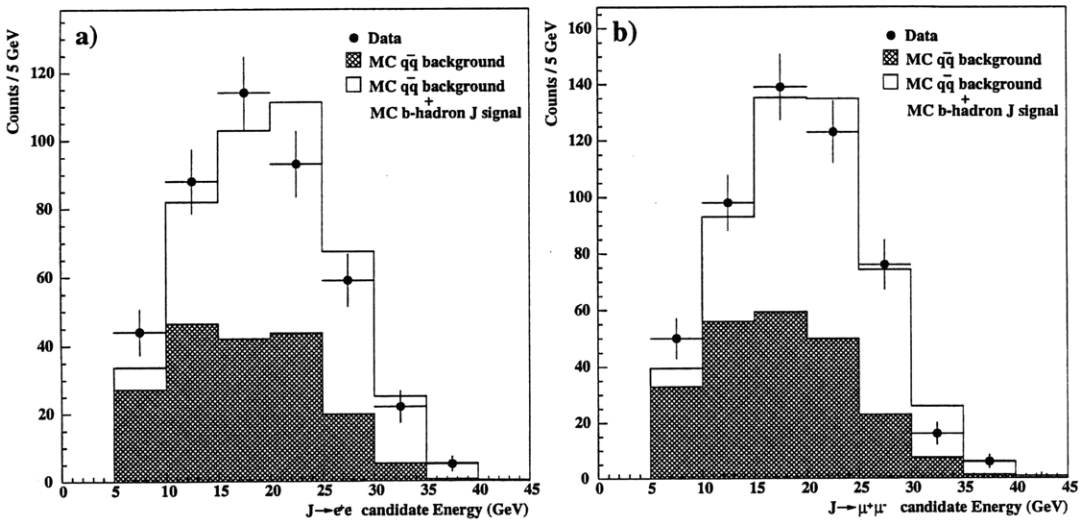

Figure 6-9: J energy spectra with uncorrected Monte Carlo (general selection)
Energy spectra of data a) $J \to e^+e^-$ and b) $J \to \mu^+\mu^-$ candidates (general selection) in the J mass window from 2.733 GeV to 3.467 GeV (dots) together with expected spectra of background under the J peak from Monte Carlo $q\bar{q}$ events (hatched histogram) and the spectra obtained by summing the Monte Carlo $q\bar{q}$ background distribution and the uncorrected Monte Carlo b-hadron decay J distribution (solid histogram).

stating explicitly that for a J sample dominated by b-hadron decay J's the J energy and the E_{30} variable are strongly anticorrelated. This is because the J's in such a sample are typically found inside a jet produced by one of the primary b-quarks. Therefore, one can approximate the sum of the J energy and E_{30} as the beam energy, and if there is a problem with the Monte Carlo description, it should be revealed in both distributions.

Looking at the J energy spectra in Figure 6-9, it appears that the data distributions in both the $J \to e^+e^-$ and $J \to \mu^+\mu^-$ channels are shifted to slightly lower energies than the full Monte Carlo estimates. A less noticeable shift in the opposite direction seems to also be present in the E_{30} distributions of Figure 6-10. The most obvious explanation for such a shift is that the background normalization determined by fitting the data invariant mass distribution is wrong. If this was the case

one could improve the agreement between the data and Monte Carlo J energy spectra by increasing

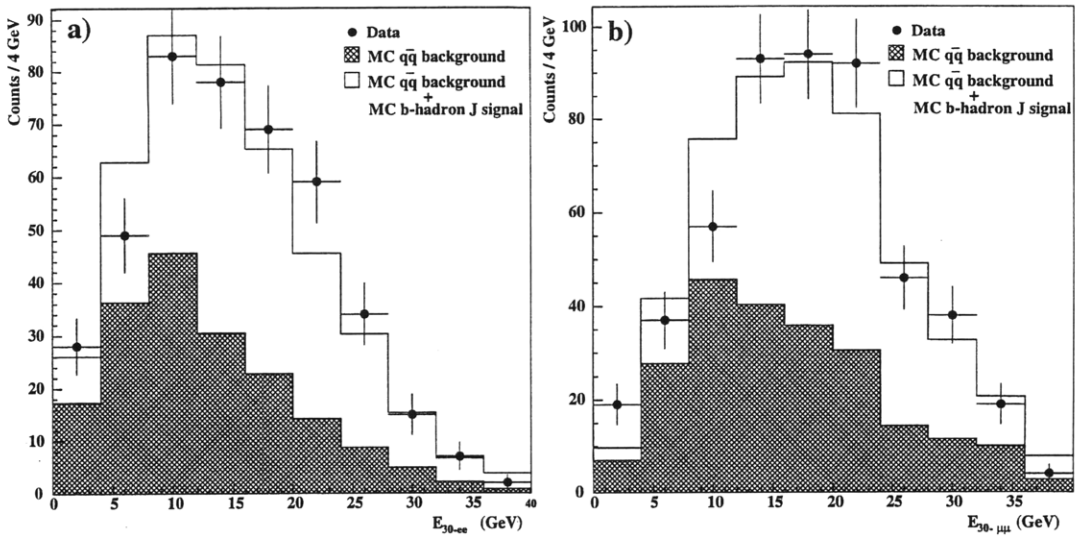

Figure 6-10: J E_{30} distributions with uncorrected Monte Carlo (general selection)
E_{30} distributions of data a) $J \to e^+e^-$ and b) $J \to \mu^+\mu^-$ candidates (general selection) in the J mass window from 2.733 GeV to 3.467 GeV (dots) together with expected distributions of background under the J peak from Monte Carlo $q\bar{q}$ events (hatched histograms) and the distributions obtained by summing the Monte Carlo $q\bar{q}$ background distributions and the uncorrected Monte Carlo b-hadron decay J distributions (solid histogram).

the amount of background. However, to improve the agreement between the data and Monte Carlo E_{30} distributions, it would be necessary to decrease the background slightly. In other words, an improvement in one variable made by adjusting the background normalization would result in a degradation of the other. Given this situation, it was concluded that the background normalization was not a likely cause for the shift. A second possibility that was considered was that the Monte Carlo descriptions of the background shapes were not correct. This was tested by comparing data and Monte Carlo in the invariant mass range between 2.0 GeV and 2.7 GeV (below the J signal region), and near perfect agreement was observed for both the $J \to e^+e^-$ and $J \to \mu^+\mu^-$ channels. Therefore, the background shape description was rejected as the explanation for the discrepancy. With no other simple explanation forthcoming, the differences seen in Figures 6-9 and 6-10 were finally ascribed to fundamental physics aspects not properly accounted for in the b-hadron decay J Monte Carlo events.

Despite the fact that no truly satisfactory explanation of the apparent shifts in Figures 6-9 and 6-10 could be determined, an attempt was made to push them into better agreement by brute force. The motivation behind this short study was to improve the estimate of the b-hadron decay J efficiency for the prompt selection and to arrive at some idea of the magnitude of the systematic errors associated with the Monte Carlo description of the J energy and E_{30}. From examination

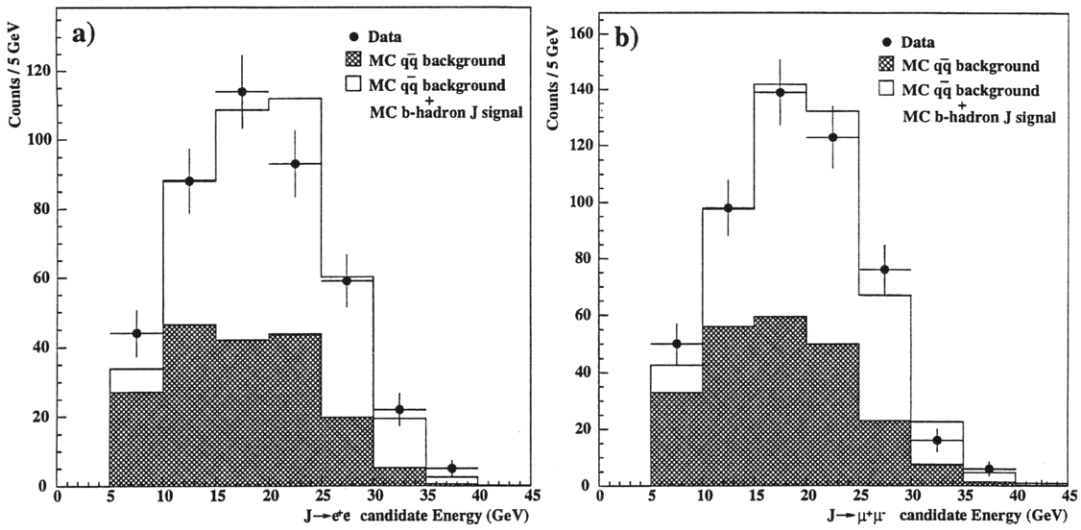

Figure 6-11: J energy spectra with corrected Monte Carlo (general seleciton)
Energy spectrum of data a) $J \to e^+e^-$and b) $J \to \mu^+\mu^-$candidates (general selection) in the J mass window from 2.733 GeV to 3.467 GeV (dots) together with expected spectrum of background under the J peak from Monte Carlo $q\bar{q}$ events (hatched histogram) and the spectrum obtained by summing the Monte Carlo $q\bar{q}$ background distribution and the corrected Monte Carlo b-hadron decay J distribution (solid histogram).

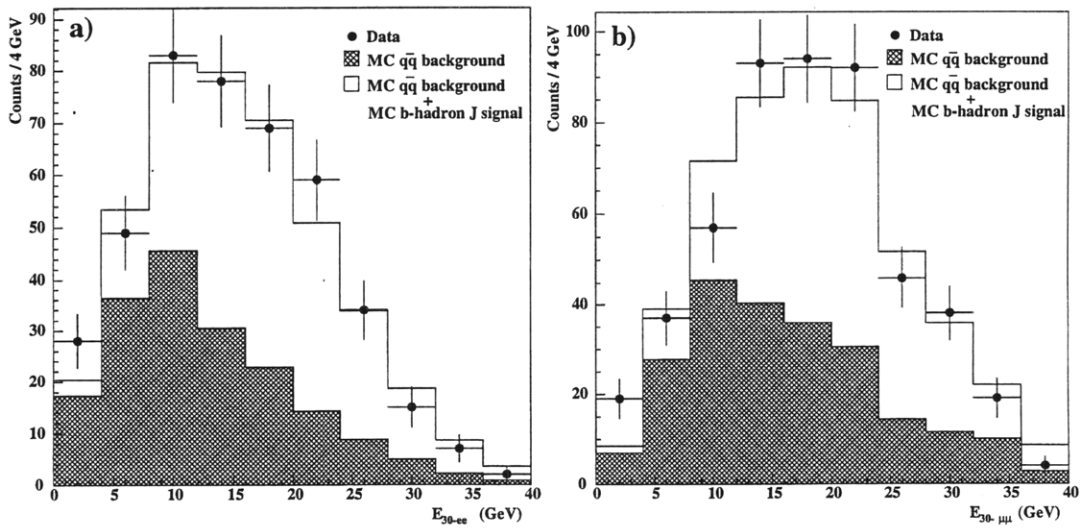

Figure 6-12: J E_{30} distributions with corrected Monte Carlo (general selection)
E_{30} distributions of data a) $J \to e^+e^-$and b) $J \to \mu^+\mu^-$candidates (general selection) in the J mass window from 2.733 GeV to 3.467 GeV (dots) together with expected distributions of background under the J peak from Monte Carlo $q\bar{q}$ events (hatched histograms) and the distributions obtained by summing the Monte Carlo $q\bar{q}$ background distributions and the corrected Monte Carlo b-hadron decay J distributions (solid histogram).

of the distributions of the most energetic and least energetic leptons for each J candidate, it was discovered that the latter was in very good agreement while the former was not. Therefore, for the Monte Carlo b-hadron decay J sample only, the energy of the most energetic lepton was shifted by a small amount while the E_{30} was shifted by the same amount in the opposite sense (under the assumption that $E_{30} \approx E_{beam} - E_J$). Quality of fit χ^2's were then calculated for both the J energy and E_{30} distributions, and this whole process was repeated for different shift magnitudes. From the plot of each χ^2 as a function of the energy shift, the minimum was ascertained, and the minima for $J \to e^+e^-$ and $J \to \mu^+\mu^-$ were averaged separately to estimate the optimal shifts to use with the Monte Carlo b-hadron decay J events. The shifts determined in this manner were 1.7 GeV for $J \to e^+e^-$ candidates and 0.92 GeV for $J \to \mu^+\mu^-$ candidates, and the corrected J energy and E_{30} histograms using these values are shown in Figures 6-11 and 6-12. The determination of the b-hadron decay J efficiency using the prompt selection was repeated using these same energy shifts, and the resulting value was averaged with the value derived from uncorrected b-hadron decay J events, yielding the efficiency given in Table 6.1. Half of the efficiency difference was then assigned as the systematic error involved with the Monte Carlo description of the J energy and E_{30}. Numerically, this systematic error is $\pm 8.5\%$.

Three additional sources of systematic error were considered in the measurement of f_p, the fraction of prompt J mesons in Z decays: the fitting and counting of the background under the prompt J peak, the correction involved with determining the real selection efficiency from an ideal simulation of Monte Carlo events, and finite Monte Carlo statistics. The systematic error induced

Error Source	Quantity Affected	Quantity Range	$(\Delta f_p/f_p)(\%)$
fitting / background counting	N_J^1	539.4 – 566.6	± 16.1
	N_J^2	28.8 – 37.4	
Monte Carlo energy shift	E_1	0. GeV – 1.7 GeV (ee)	± 8.5
		0. GeV – 0.92 GeV($\mu\mu$)	
J pseudo-ϵ correction	ϵ_b^1	0.2633 – 0.2911	± 7.9
	ϵ_b^2	0.0029 – 0.0032	
	ϵ_p^1	0.2560 – 0.2826	
	ϵ_p^2	0.1577 – 0.1755	
Monte Carlo statistics	ϵ_b^1	0.2744 – 0.2800	± 2.4
	ϵ_b^2	0.0029 – 0.0032	
	ϵ_p^1	0.2665 – 0.2721	
	ϵ_p^2	0.1641 – 0.1691	
TOTAL			± 20.0

Table 6.3: Systematics for f_p
Sources and magnitudes of systematic errors for the measurement of f_p.

by all of the cuts in the selection except those on E_{30} is considered negligible since:

$$f_p \approx \frac{N_J^2}{N_J^1} \cdot \frac{\epsilon_b^1}{\epsilon_p^2} \tag{6.1}$$

where the superscripts {1,2} denote the general selection and prompt selection, respectively. The error due to the choice of cuts enters into each efficiency in Equation 6.1 at roughly the same level, resulting in a near cancellation. In other words, the general and prompt selections are highly correlated, apart from the cut on E_{30}, so that any error due to the choice of cuts has little impact on the measurement of f_p. Furthermore, from the systematic error study for the measurement of $Br(Z \rightarrow J + X)$ in Chapter 4, it is expected that these errors should be insignificant compared to the others mentioned above. Therefore, the error on f_p from all of the selection cuts except those on E_{30} is ignored for this systematic error analysis. As mentioned in the data analysis section, an estimate of the error due to the counting of the background in the signal region was made by fitting two different background distributions, one from the actual data and one from a properly normalized Monte Carlo $q\bar{q}$ sample. The contribution of this source of systematic error is $\pm 16.1\%$ as shown in Table 6.3. The remaining sources of systematic error are of minor importance compared to this one but are included here for completeness. The uncertainty associated with the J pseudo-efficiency correction is estimated to be $\pm 5\%$. Applying this to each efficiency used in the determination of f_p yields a systematic error on f_p of $\pm 7.9\%$. This systematic error is retained despite Equation 6.1 because it is not known exactly how the efficiency correction factors apply in isolated versus jet-like environments. Lastly, there is a small systematic error of $\pm 2.4\%$ due to the limited statistics of the various Monte Carlo J samples used to estimate the selection efficiencies.

The significant theoretical uncertainty involved with the rates of the individual prompt J production processes, translates into a rather large theoretical systematic error for the measurement of f_p, which is calculated separately from the other systematics. A dependency of the measurement of f_p on the theoretical rates arises because the selection efficiencies for the different types of prompt J's vary and the rates are used to assign weights to each process when calculating the combined prompt J efficiency. The uncertainties in the theoretical rates are uniformly fixed to be $\pm 50\%$, which is a reasonable upper limit derived from the relevant published theoretical papers on prompt J production [11] [12] [48] [29] [50] [53]. Varying the rates within these liberal ranges modifies the prompt process weights, which in turn modifies the prompt J selection efficiencies for both the general selection and the prompt selection. Calculation of the resulting effect on f_p leads to a theoretical systematic error of $^{+17.2}_{-8.8}\%$.

6.6 Results

In order to determine the prompt J fraction in Z decays, it is necessary to perform basically two separate measurements with two different selections. The clear choices for these selections are the general selection given in Chapter 4 and the prompt selection presented earlier in this chapter. As noted previously, the efficiencies for the various J production processes for these two selections are summarized in Tables 6.1 and 6.2. For the sake of clarity, the mathematical steps involved in obtaining the formula for f_p are now described. First, one can write the number of J's selected with any given selection (N_J^i, where i={1,2}) as the number of b-hadron decay J's in the initial sample (N_b) times the b-hadron decay J efficiency (ϵ_b^i, where i={1,2}) plus the number of prompt J's in the initial sample (N_p) times the prompt J efficiency (ϵ_p^i, where i={1,2}).

$$N_J^i = N_b \cdot \epsilon_b^i + N_p \cdot \epsilon_p^i \tag{6.2}$$

$$N_J^1 = N_b \cdot \epsilon_b^1 + N_p \cdot \epsilon_p^1 \tag{6.3}$$

$$N_J^2 = N_b \cdot \epsilon_b^2 + N_p \cdot \epsilon_p^2 \tag{6.4}$$

Next, recognizing that the total number of initial J's (N_{J-tot}) is the sum of the initial number of prompt J's plus the initial number of b-hadron decay J's, one can replace the latter in favor of N_{J-tot}.

$$N_J^1 = N_{J-tot} \cdot \epsilon_b^1 + N_p \cdot (\epsilon_p^1 - \epsilon_b^1) \tag{6.5}$$

$$N_J^2 = N_{J-tot} \cdot \epsilon_b^2 + N_p \cdot (\epsilon_p^2 - \epsilon_b^2) \tag{6.6}$$

Finally, defining $A = N_J^2/N_J^1$ and rearranging, one can derive the expression for f_p shown in Equation 6.7.

$$f_p = \frac{\epsilon_b^2 - A \cdot \epsilon_b^1}{A \cdot (\epsilon_p^1 - \epsilon_b^1) - (\epsilon_p^2 - \epsilon_b^2)} \tag{6.7}$$

With Equation 6.7 in hand, it is straightforward to calculate f_p. From Chapter 4, the number of J's selected using the general selection was $(553 \pm 37 \pm 13.6)$, and from earlier in this chapter the number of J's selected using the prompt selection was $(33.1 \pm 7.3 \pm 4.3)$. Therefore, $A = (5.99 \pm 1.38 \pm 0.79) \times 10^{-2}$. Substitution of this quantity and the known efficiencies in the expression for f_p, one finds:

$$f_p = (8.3 \pm 2.3 \pm 1.7^{+1.4}_{-0.7}) \times 10^{-2}$$

In this expression, the measurement errors from left to right are statistical, systematic, and theoretical. It is of some interest to note that by using Equation 6.2, one can also easily determine the

composition of the samples selected with the various selections. Depending on whether one chooses to use the raw b-hadron decay J efficiency or the corrected b-hadron decay J efficiency, the composition of the prompt selection sample is either (78% prompt J / 22% b-hadron decay J) or (89% prompt J / 11% b-hadron decay J). In both cases, the calculations yield the expectation that the prompt selection sample is strongly dominated by prompt J's. Given these numbers, it is difficult to imagine that the prompt selection sample could be explained by b-hadron decay J's alone.

Using the value of $\mathrm{Br}(\mathrm{Z} \to \mathrm{J} + \mathrm{X})$ found in Chapter 4, the measurement of f_p is easily converted into a measurement of the inclusive branching ratio of the Z to prompt J mesons. Multiplying f_p and $\mathrm{Br}(\mathrm{Z} \to \mathrm{J} + \mathrm{X})$, one obtains:

$$\mathrm{Br}(\mathrm{Z} \to \mathrm{J}_{\mathrm{prompt}} + \mathrm{X}) = (2.7 \pm 0.8 \pm 0.5^{+0.4}_{-0.2}) \times 10^{-4}$$

For the purpose of comparison, the theoretical branching ratio in the VSM is 2.8×10^{-4} (see Table 1.1). Thus, excellent agreement is observed despite the sizable experimental and theoretical uncertainties.

6.7 Discussion

Having completed the measurement of f_p, it is worthwhile to examine again the evidence available from this analysis for the observation of prompt J's. The most convincing evidence has to be the clear J peak in the signal region of the invariant mass distribution, which contains a number of J's far in excess of what is expected from the b-hadron decay production process alone. 33.1 J's are measured above the background, and using the b-hadron decay efficiencies in Tables 6.2 and 6.1 together with the number of J's measured in Chapter 4, one can quickly calculate that only 5.5 of these J's are expected to be from b-hadron decay. In addition, the b-tag discriminant variable distribution for prompt J candidate events in data, which admittedly is not very significant statistically, still appears to be peaked at low values, suggesting that many of the J candidates are prompt. Further inspection of Figure 6-8b shows that this is quite different from the distributions of background and, even more importantly, b-hadron decay J events. Finally, the agreement between data and Monte Carlo for the J candidate energy spectrum and the distribution of the angle to the most energetic jet, while not spectacular, is satisfactory. While this last item cannot be considered conclusive evidence, it is certainly necessary to demonstrate such qualitative agreement. These three points taken together create a fairly compelling case for the observation of prompt J's in L3 data.

In conclusion, the measurement of the prompt J fraction in Z decays has been made for the first time at the L3 Experiment at LEP. Moreover, the value of f_p is distinctly nonzero. Prior to this measurement, non-observation allowed only an upper limit on the rate of J's produced from the gluon-fragmentation process to be made. With this new measurement of f_p, it can be affirmed that prompt J's are present in the LEP I data at an observable level. Previously, the OPAL Experiment

has studied prompt J production and also observed prompt J's in their data. Using a selection based on an energy isolation cut and b-tagging, OPAL determined $f_{\rm p} = (4.8 \pm 1.7 \pm 1.1 \pm 1.3)\%$ [44]. This is clearly lower than the measurement from this analysis but is still perfectly consistent within the errors. Thus, experiment supports a value of $f_{\rm p}$ in the general range of 5% to 10%.

What is less clear is the precise composition of the prompt sample in Z decays. As noted in the last section, the branching ratio to prompt J's derived from the measurement of $f_{\rm p}$ is in surprisingly good agreement with the theoretical value for this quantity, but this is true only if one includes the color octet gluon-fragmentation rate in the theoretical estimate. Otherwise, $f_{\rm p}$ and the branching ratio to prompt J's derived therefrom become 17.3% and 5.5×10^{-4}, respectively. This last value should be compared to the theoretical branching ratio of 9.1×10^{-5} obtained by summing the theoretical color singlet process rates only. Of course, there is quite a large error associated with the experimental determination of $\mathrm{Br}(\mathrm{Z} \to \mathrm{J}_{\rm prompt} + \mathrm{X})$ and with the theoretical rates as well. Still, the discrepancy between theory and experiment under the assumption of no color octet contributions is at the 2σ level. Consequently, while the results of this analysis of prompt J's in Z decays do not exclude this possibility, they are certainly more compatible with the hypothesis of a dominant color octet gluon-fragmentation contribution, as expected in the VSM.

Chapter 7

Conclusions

A comprehensive study of charmonium production in e^+e^- collisions at the Z pole has been carried out using the L3 detector at LEP in order to test the reliability of modern heavy quarkonium production calculations and to possibly differentiate between competing theoretical models. The specific measurements performed include determinations of $Br(Z \rightarrow J + X)$, $Br(Z \rightarrow \psi' + X)$, and $Br(Z \rightarrow \chi_c^1 + X)$ and the first estimate made at L3 for f_p, the fraction of prompt J's in Z decays. In obtaining these results, the full LEP I data set has been analyzed, and this set of measurements likely represents the final work on the topic at this experiment. The measured values of the various branching ratios are in good agreement with those from other experiments and with values previously reported by other members of the L3 Collaboration. In addition, these investigations support a non-zero value for f_p of roughly the same magnitude as that recently observed by the OPAL Collaboration. The presence of measurable quantities of prompt J's in the LEP data runs contrary to the expectations of the Color Singlet Model and is more compatible with theoretical calculations made within the framework of the Velocity Scaling Model or the Color Evaporation Model. From VSM fits to CDF charmonium production data at high p_t, it has been concluded that color octet gluon fragmentation plays a major role in heavy quarkonium production at the Tevatron. Though the collision processes are different at the Tevatron and at LEP, VSM predictions of prompt J production at the Z pole based on the CDF fits also involve a dominant contribution from color octet gluon fragmentation. Without this contribution, the overall prompt J production rate would be roughly a factor three lower and very difficult to measure. Thus, the observation of prompt J mesons in appreciable quantities together with several other results from this thesis tend to support the VSM or the CEM and are in accord with the original findings at CDF.

The general analysis of charmonium production in hadronic Z decays was described in Chapter 4, and the primary results were:

$$Br(Z \rightarrow J + X) = (3.16 \pm 0.21^{+0.19}_{-0.28}) \times 10^{-3}$$

$$\mathrm{Br}(Z \to \psi' + X) = (2.4 \pm 0.5^{+0.7}_{-0.8}) \times 10^{-3}$$
$$\mathrm{Br}(b \to J + X) = (0.94 \pm 0.07^{+0.06}_{-0.09})\%$$

Of these, the branching ratio $\mathrm{Br}(b \to J + X)$ is the most fundamental quantity because it can be measured in a variety of experiments at any number of different facilities. One of the best measurements of this branching ratio comes from CLEO II: $\mathrm{Br}(b \to J + X) = (1.12 \pm 0.04 \pm 0.06)\%$ [61]. The branching ratio determined from this analysis is in fair agreement with this value, but more importantly, it, like the CLEO II result, is substantially larger than the theoretical value predicted by the CSM. As pointed out previously, $\mathrm{Br}(b \to J + X)$ together with other known branching ratios can be used to calculate $\mathrm{Br}(b \to J + X)_{\mathrm{direct}}$ by subtracting the feeddown contributions from higher radial and angular momentum states. Doing so with the $\mathrm{Br}(b \to J + X)$ given above, one obtains:

$$\mathrm{Br}(b \to J + X)_{\mathrm{direct}} = (0.61 \pm 0.07^{+0.07}_{-0.09})\%$$

This value is inconsistent with the CSM prediction 0.23% but agrees nicely with the VSM prediction 0.58% recently calculated by Ko, Lee, and Song [22] [24]. Unfortunately, the CEM does not apply to the production of charmonium states in the process of b-hadron decays, and therefore, predictions of this theory cannot be compared with the experimental results from this analysis. However, one can infer from the measurement of J production at L3 that the VSM is favored over the CSM.

The next major topic of charmonium production that was investigated was the production of the χ_c states. In Chapter 5 it was shown that there was no evidence of significant quantities of χ_c^0's or χ_c^2's in the data. However, from the clear χ_c^1 peak measurements of $\mathrm{Br}(Z \to \chi_c^1 + X)$ and $\mathrm{Br}(b \to \chi_c^1 + X)$ were made:

$$\mathrm{Br}(Z \to \chi_c^1 + X) = (1.9 \pm 0.7^{+0.3}_{-0.6}) \times 10^{-3}$$
$$\mathrm{Br}(b \to \chi_c^1 + X) = (0.55 \pm 0.20^{+0.10}_{-0.19})\%$$

The latter result, in turn, was used to derive an estimate for $\mathrm{R}_{\chi_c^1}$:

$$\mathrm{R}_{\chi_c^1} = (0.58 \pm 0.22^{+0.12}_{-0.21})$$

Here again the numbers disfavor the CSM. According to the CSM this ratio should have a value near $\mathrm{R}_{\chi_c^1} = 0.24$, and it is worth noting that this estimate has relatively small error because QCD uncertainties in the individual branching ratios largely cancel in the ratio $\mathrm{R}_{\chi_c^1}$ [13]. Mature numerical VSM estimates for this quantity and for $\mathrm{Br}(b \to \chi_c^1 + X)$ are not yet available in the literature. However, one qualitative prediction of the VSM and the CEM is the possible presence of χ_c^2's in the data. χ_c^2's are strongly suppressed in the CSM, but this is not true for the other models, where production would proceed through color octet diagrams at first order. Because the magnitude of the branching ratio $\mathrm{Br}(\chi_c^2 \to J\gamma)$ is just half that of $\mathrm{Br}(\chi_c^1 \to J\gamma)$, though, any χ_c^2 peak in the mass difference distribution is still expected to be smaller than the χ_c^1 peak. Despite the fact that this analysis cannot confirm the existence of χ_c^2's, this non-observation should not be interpreted as

evidence against the VSM or CEM. The statistics are simply too low to warrant such a conclusion. The evidence against the CSM in the form of the $R_{\chi_c^1}$ measurement, on the other hand, is nontrivial.

The last and most important aspect of charmonium production studied in this thesis was prompt J production in Z decays. A description of this analysis was given in Chapter 6, and evidence was presented there for the observation of prompt J mesons. Working under the positive observation hypothesis, the following results were derived:

$$f_p = (8.3 \pm 2.3 \pm 1.7^{+1.4}_{-0.7}) \times 10^{-2}$$
$$\mathrm{Br}(Z \to J_{\mathrm{prompt}} + X) = (2.7 \pm 0.8 \pm 0.5^{+0.4}_{-0.2}) \times 10^{-4}$$

Like the other measurements, these too disagree with the CSM predictions. Because the experimental and theoretical errors are still quite large, however, the disagreement is only at the 2σ level. Within the context of the CSM, one expects the branching ratio of the Z to prompt J's to be closer to $\mathrm{Br}(Z \to J_{\mathrm{prompt}} + X) = 9.1 \times 10^{-5}$ [11] [12] [48] [29] [50] [53]. However, the VSM and CEM, both of which include color octet contributions, predict substantially higher rates for prompt J mesons. VSM calculations yield an expected branching ratio of $\mathrm{Br}(Z \to J_{\mathrm{prompt}} + X) = 2.8 \times 10^{-4}$, while the CEM predicts $\mathrm{Br}(Z \to J_{\mathrm{prompt}} + X) \geq 1.8 \times 10^{-4}$ [11] [12] [48] [29] [50] [53] [54]. Thus, the VSM shows the best agreement with the data, although the CEM is also consistent with the observed $\mathrm{Br}(Z \to J_{\mathrm{prompt}} + X)$. From this single measurement, even the CSM cannot be entirely discounted, but the aforementioned 2σ discrepancy for prompt J production makes it a less attractive alternative.

To summarize, the experimental work for this thesis comprises several different measurements of charmonium production at the Z pole, and these results have been compared to the predictions of the Color Singlet Model, the Velocity Scaling Model, and the Color Evaporation Model. While no single measurement has been overwhelmingly conclusive, the J, χ_c, and prompt J production measurements taken together indicate possible inconsistency with the CSM. In each instance the measured value is at odds with the CSM calculations at the 1σ to 2σ level. Furthermore, these same measurements are in surprisingly good agreement with the expectations of the VSM, aside from the previously noted non-observation of χ_c^2 states. Regarding the CEM, little can be said with certainty, since out of the measurements performed here, this model is only applicable to the prompt J measurement, and for this the theoretical results are perfectly consistent with the experimental ones. In order to truly test the CEM, it is necessary to examine the constancy of the ratios of prompt charmonium and bottomonium production cross sections in different collision environments and as functions of kinematic variables. Such studies have been carried out with electroproduction, photoproduction, and hadroproduction data, but unfortunately, the limited size of the LEP prompt charmonium data sample prevents it from being of much use in this type of analysis. It follows that the question of whether the VSM or CEM is the more accurate description of heavy quarkonium production will not be resolved at LEP. Therefore, it is incumbent upon future theorists and future experimenters working with larger data sets at a variety of facilities to

explore and settle this matter definitively. Only through such scientific inquiry can we further our understanding of heavy quarkonium production, a task important in its own right but perhaps even critical to future measurements which might depend on knowledge of this most basic of physical processes.

Bibliography

[1] J.J. Aubert *et al.*, Phys. Rev. Lett. **33** (1974) 1404–1406.

[2] J.E. Augustin *et al.*, Phys. Rev. Lett. **33** (1974) 1406–1408.

[3] Gerhard A. Schuler, Production of Heavy Quarks and Heavy Quarkonia, CERN preprint CERN-TH/95-75 (hep-ph/9504242).

[4] R. Baier and R. Rückl, Z. Phys. **C 19** (1983) 251–266.

[5] Geoffrey T. Bodwin, Eric Braaten, and G. Peter Lepage, Phys. Rev. **D 51** (1995) 1125–1171.

[6] R. Gavai, D. Kharzeev, H. Satz, G.A. Schuler, K. Sridhar, and R. Vogt, Int. J. Mod. Phys. **A 10** (1995) 3043–3070.

[7] Gerhard A. Schuler and Ramona Vogt, Systematics of Quarkonium Production, CERN preprint CERN-TH/96-157.

[8] Harald Fritzsch, Phys. Lett. **B 67** (1977) 217–221.

[9] Eric Braaten, Sean Fleming, and Tzu Chiang Yuan, Production of Heavy Quarkonium in High Energy Colliders, University of Wisconsin - Madison preprint MADPH-96-927 (hep-ph/9602374).

[10] Matteo Cacciari, Mario Greco, Michelangelo L. Mangano and Andrea Petrelli, Phys. Lett. **B 356** (1995) 553.

[11] V. Barger, Kingman Cheung and W.-Y. Keung, Phys. Rev. **D 41** (1990) 1541–1546.

[12] Eric Braaten, Kingman Cheung and Tzu Chiang Yuan, Phys. Rev. **D 48** (1993) 4230–4235.

[13] J.H. Kühn, S. Nussinov, and R. Rückl, Z. Phys. **C 5** (1980) 117–120.

[14] Thomas A. DeGrand and Doug Touusaint, Phys. Lett. **B 89** (1980) 256–258.

[15] Mark W. Bailey, Charmonium and Bottomonium Production in $p\bar{p}$ Collisions at CDF (1996).

[16] R. Barbieri, R. Gatto, and E. Remiddi, Phys. Lett. **B 61** (1976) 465–468.

[17] R. Barbieri, M. Caffo, and E. Remiddi, Nucl. Phys. **B 162** (1980) 220–236.

[18] R. Barbieri, M. Caffo, R. Gatto, and E. Remiddi, Phys. Lett. **B 95** (1980) 93–95.

[19] R. Barbieri, M. Caffo, R. Gatto, and E. Remiddi, Nucl. Phys. **B 192** (1981) 61–65.

[20] Eric Braaten, Radiative Corrections to Quarkonium Decays: From a Model to a Rigorous Theory, Northwestern University preprint NUHEP-TH-94-22 (hep-ph/9409286).

[21] Geoffrey T. Bodwin, Eric Braaten, and G. Peter Lepage, Phys. Rev. **D 46** (1992) R1914–R1918.

[22] Geoffrey T. Bodwin, Eric Braaten, Tzu Chiang Yuan, and G. Peter Lepage, Phys. Rev. **D 46** (1992) R3703–R3707.

[23] Gerhard A. Schuler, Quarkonium Production: Velocity-scaling Rules and Long-distance Matrix Elements, CERN preprint CERN-TH/97-12 (hep-ph/9702230).

[24] Pyungwon Ko, Jungil Lee, and H.S. Song, Phys. Rev. **D 53** (1996) 1409–1415.

[25] Feng Yuan, Cong-Feng Qiao, and Kuang-Ta Chao, Phys. Rev. **D 56** (1997) 329–334.

[26] Pyungwon Ko, Jungil Lee, and H.S. Song, Phys. Lett. **B 395** (1997) 107–112.

[27] Eric Braaten and Tzu Chiang Yuan, Phys. Rev. **D 52** (1995) 6627–6629.

[28] Eric Braaten and Tzu Chiang Yuan, Phys. Rev. **D 50** (1994) 3176–3180.

[29] Peter Cho, Phys. Lett. **B 368** (1996) 171–178.

[30] Kingman Cheung, Wai-Yee Keung, and Tzu Chiang Yuan, Phys. Rev. Lett. **76** (1996) 877–880.

[31] Seungwon Baek, P. Ko, Jungil Lee and H.S. Song, Color-octet Heavy Quarkonium Productions in Z^0 Decays at LEP, Seoul National University preprint SNUTP 96-061 (1996).

[32] Feng Yuan, Cong-Feng Qiao, and Kuang-Ta Chao, Phys. Rev. **D 56** (1997) 321–328.

[33] Peter Cho and Adam K. Leibovich, Phys. Rev. **D 53** (1996) 150–162.

[34] Peter Cho and Adam K. Leibovich, Phys. Rev. **D 53** (1996) 6203–6217.

[35] Pyungwon Ko, Jungil Lee, and H.S. Song, Color-octet Mechanism in $\gamma + p \to \mathrm{J}/\psi + X$, Seoul National University preprint.

[36] James Amundson, Sean Fleming, and Ivan Maksymyk, Photoproduction of J/ψ in the Forward Region, University of Wisconsin - Madison preprint MADPH-95-914 (hep-ph/9601298).

[37] Sean Fleming, Int. J. Mod. Phys. **A** (1996) 1–10.

[38] Francis Halzen and Satoshi Matsuda, Phys. Rev. **D 17** (1978) 1344–1355.

[39] M. Glück, J.F. Owens, and E. Reya, Phys. Rev. **D 17** (1978) 2324–2331.

[40] F. Halzen, Phys. Lett. **B 69** (1977) 105–108.

[41] J.F. Amundson, O.J.P. Eboli, E.M. Gregores, and F. Halzen, Phys. Lett. **B 390** (1997) 323–328.

[42] J.F. Amundson, O.J.P. Eboli, E.M. Gregores, and F. Halzen, Phys. Lett. **B 372** (1996) 127–132.

[43] NA14 Collaboration, Z. Phys. **C 33** (1987) 505.

[44] OPAL Collaboration, Phys. Lett. **B 384** (1996) 343.

[45] DELPHI Collaboration, Search for Promptly Produced Heavy Quarkonium States in Hadronic Z Decays, Delphi note 95-77 PHYS 512 (1995).

[46] L3 Collab., O. Adriani *et al.*, Phys. Lett. **B 288** (1992) 412.

[47] Eric Braaten and Sean Fleming, Phys. Rev. Lett. **74** (1995) 3327–3330.

[48] Estia J. Eichten and Chris Quigg, Phys. Rev. **D 52** (1995) 1726–1728.

[49] Particle Data Group, Phys. Rev. **D 54** (1996) I.54.

[50] K. Hagiwara, A.D. Martin, and W.J. Stirling, Phys. Lett. **B 267** (1991) 527–531.

[51] K. Hagiwara, A.D. Martin, and W.J. Stirling, Phys. Lett. **B 316** (1993) 631.

[52] Eric Braaten and Tzu Chiang Yuan, Phys. Rev. Lett. **71** (1993) 1673–1676.

[53] Wai-Yee Keung, Phys. Rev. **D 23** (1981) 2072–2074.

[54] E.M. Gregores, F. Halzen, and O.J.P. Eboli, Prompt Charmonium Production in Z Decays, University of Wisconsin - Madison preprint MADPH-96-950 (hep-ph/9607324).

[55] Eric Braaten, Quarkonium Polarization in the NRQCD Factorization Framework, Ohio State University preprint OHSTPY-96-925 (hep-ph/9609338).

[56] Peter Cho and Mark B. Wise, Phys. Lett. **B 346** (1995) 129–136.

[57] J.H. Kühn and R. Rückl, Phys. Lett. **B 135** (1984) 477–480.

[58] P.H. Cox, S. Hovater, and S.T. Jones, Phys. Rev. **D 32** (1985) 1157–1163.

[59] L. Bergström and P. Ernström, Phys. Lett. **B 328** (1994) 153–161.

[60] P. Ko, Phys. Rev. **D 52** (1995) 3108–3110.

[61] CLEO II Collaboration, Phys. Rev. **D 52** (1995) 2661.

[62] Robert N. Cahn and Gerson Goldhaber, The Experimental Foundations of Particle Physics, (Cambridge University Press, 1989).

[63] Large Electron-Positron Storage Ring Technical Notebook.

[64] O. Adriani *et al.*, Nucl. Inst. Meth. **A 348** (1994) 431–435.

[65] A. Adam *et al.*, Nucl. Inst. Meth. **A 348** (1994) 436–439.

[66] L3 Collab., B. Adeva *et al.*, Nucl. Inst. Meth. **A 289** (1990) 35.

[67] D. Bourilkov *et al.*, TEC Offline Practical Guide (1996).

[68] L3 Collaboration, Phys. Lett. **B 377** (1996) 313–324.

[69] Lucas Taylor, On the Use of Cosmic Ray Muon Events for the Calibration of the L3 Time-Expansion Chamber (1997).

[70] L3 Muon Group, Nucl. Inst. Meth. **A 383** (1996) 342–366.

[71] Y. Karyotakis and M. Wadhwa, Results of the Energy Calibration on the Low Energy Electromagnetic Bumps (1995).

[72] L3 Collaboration, Phys. Lett. **B 407** (1997) 341–350.

[73] L3 Collab., M. Acciarri *et al.*, Z. Phys. **C 62** (1994) 551.